UNIVERSIDAD DE CHILE
FACULTAD DE CIENCIAS FÍSICAS Y MATEMÁTICAS
DEPARTAMENTO DE INGENIERÍA MATEMÁTICA

NUMERICAL STUDIES OF A HOMOGENIZED BONE MODEL AND APPLICATIONS TO POROSITY IDENTIFICATION BY ULTRASOUND

TESIS PARA OPTAR AL GRADO DE MAGÍSTER EN
CIENCIAS DE LA INGENIERÍA, MENCIÓN MATEMÁTICAS APLICADAS

MEMORÍA PARA OPTAR AL TÍTULO DE
INGENIERO CIVIL MATEMÁTICO

REIDMEN ALEXANDER ARÓSTICA BARRERA

PROFESOR GUÍA :
AXEL OSSES ALVARADO
PROFESOR COGUÍA :
JEAN-GABRIEL MINONZIO

COMISION
CARLOS CONCA ROSENDE

Este trabajo ha sido parcialmente financiado por Proyecto Fondecyt 1151512 y CMM Conicyt PIA AFB170001
Powered@NLHPC: Esta tesis fue parcialmente apoyada por la infraestructura de supercómputo del NLHPC (ECM-02)

SANTIAGO DE CHILE
2019

RESUMEN DE LA MEMORIA PARA OPTAR
AL TÍTULO DE
INGENIERIO CIVIL MATEMÁTICO Y GRADO DE
MAGÍSTER EN CIENCIAS DE LA INGENIERÍA, MENCIÓN MATEMÁTICAS APLICADAS
POR: REIDMEN ALEXANDER ARÓSTICA BARRERA
FECHA: 10/04/2019
PROF. GUÍA: AXEL OSSES ALVARADO
PROF. COGUÍA: JEAN-GABRIEL MINONZIO

NUMERICAL STUDIES OF A HOMOGENIZED BONE MODEL AND APPLICATIONS TO POROSITY IDENTIFICATION BY ULTRASOUND

En el contexto de estudios biomecánicos en medicina, existen diversas preguntas por responder, fluctuando desde el modelamiento mismo de tejidos u órganos a la simulación, predicción y validación de los diversos procedimientos experimentales que determinan factores clínicos de interés tal como son los parámetros de espesor, porosidad, rigidez, etc. Este trabajo está orientado en esta última dirección, mediante el cual se propone una formalización, justificación teórica y validación del problema directo de modelar el comportamiento mecánico de un hueso cortical de un nuevo procedimiento de ultrasonido. Así, mediante la teoría de homogenización, se modela la propagación de una guía de ondas en un hueso poroso idealizado e implementa numéricamente un modelo elastodinámico usando librerías al estado del arte. Los resultados obtenidos se comparan con la literatura reciente que propone el modelo experimental usado, validando el modelo numérico. Similarmente se estudia la presencia de viscosidad sobre el hueso mediante un modelo tipo *Kelvin-Voigt*, con predicciones en los factores de calidad que investigan efectos de amortiguamiento, comparable con limitados resultados experimentales recientes.

In the context of biomechanical assessment of bone in medicine, there are abundant questions to be answered, fluctuating from the modelling itself of tissues and organs to the simulation, prediction and validation of the different kind of experimental procedures that determine clinical factors of interest such as the thickness, porosity, stiffness constants, etc. This work is oriented in the later direction in which it is proposed a formalization, theoretical justification and validation of the direct problem related to modelling the mechanical behavior of cortical bone from a new ultrasound experimental procedure. By means of homogenization theory, it is described the propagation of a guided-wave in porous bone and implemented numerically an elastodynamic model by applying state-of-art libraries using FEM method. The results obtained are then compared with recent literature that propose the experimental procedure, validating the numerical model. Similarly, it is studied the presence of viscoelastic type behavior in bone by applying a *Kelvin-Voigt* model, predicting quality factors that assess damping effects which in particular are comparable with recent and limited experimental results.

A mi madre y padre, por todo.

Acknowledgement

During this work, many people have contributed not only from theoretical perspective but also by providing great commentaries, insights and life experiences. The least I can do is to mention my advisers Axel Osses and Jean-Gabriel Minonzio for allowing and support my curiosities, to try new techniques, technologies and moreover patiently explain interesting experiences from their travels and general wisdom.

This project couldn't have been done without the great time shared with many people at the Department of Mathematics (DIM) and to the department itself, providing a nice environment to be intellectually challenged and motivated. In particular, my great appreciation to Pablo Arratia for the interesting discussions and funny times, Rodrigo Zelada for the curiosities I've learn from him, Vicente Ocqueteau for the most amusing times, Daniel Pereda for the life planifications and amusement, Manuel Suil for the great shared experiences, Diego Marchant for the funny times, Felipe Matus for its weird topics and experiences, Felipe Atenas for the culturally-related curiosities and experiences, Juan d'Etigny for his physically oriented passions and Martin Rapaport for the great conversations and perspectives you've given to me. There are quite a numerous important people not mentioned from whom I'm also greatly gratified having shared some time.

Lastly, even though it is dedicated to them, this work completes a phase of outstanding support from my parents, whom I have one of the greatest admiration.

Contents

Introduction **1**

1 Context: Clinical Measurements **3**
1.1 Time-domain Modelling . . . 4
1.1.1 Experimental Procedure . . . 4
1.1.2 Signal Processing . . . 6
1.2 Main assumptions and Multiscale Modelling . . . 8

2 Homogenization and Justification **11**
2.1 Homogenization Procedure . . . 16
2.1.1 Two-Scale Asymptotic Homogenization . . . 16
2.1.2 Contribution at Second Order . . . 19
2.1.3 Contributions at First Order . . . 19
2.1.4 Contribution at the zero order . . . 20
2.2 Justification of the homogenization . . . 21
2.3 Sketch of the Proof . . . 22
2.4 Energy Estimations . . . 25
2.5 Continuity on the Porosity . . . 27
2.5.1 Definition and Estimates . . . 27
2.5.2 About the Continuity . . . 30
2.5.3 About the Derivative . . . 31

3 Discretization Procedures **34**
3.1 Numerical Schemes . . . 34
3.1.1 Approximation by Finite Spaces . . . 34
3.1.2 Time Discretization . . . 36
3.2 Dynamic Type Models . . . 37
3.2.1 Fully Elastodynamic . . . 37
3.2.2 Elastodynamic Attenuated . . . 38
3.2.3 Kelvin-Voigt Viscoelastic Type . . . 38

4 Simulations **40**
4.1 Numerical Solutions to Cell Problems . . . 40
4.1.1 2-Dimensional Models . . . 42
4.1.2 3-Dimensional Model . . . 45
4.2 2-Dimensional Simulations of Wave Propagation . . . 47
4.2.1 Case of Multiple Sources . . . 49

4.2.2 Case of a Single Source 51
4.3 Case on Frequency Domain 54
4.3.1 Solutions without Attenuation 55
4.3.2 Solution using Attenuation. 57
4.4 3-Dimensional Simulation of Wave Propagation 58
4.4.1 Half-Cylinder Case 59
4.4.2 Irregular Domain Case 62

5 Viscoelastic Predictions **67**
5.1 Formalization of Q-factors 67
5.1.1 Workflow Description 68
5.1.2 Nonlinear Decomposition 70
5.2 Predictions 70

Conclusion **71**

Bibliography **74**

List of Tables

4.1 Percentage errors of the homogenized coefficient with respect to the PG reference case. The tensors are written in *Voigt* notation and microstructure is defined by a 2-dimensional unitary square with periodic perforation as porosity as shown schematically in (1.4). 44
4.2 Percentage errors between the homogenized coefficients and the PG reference case. The tensors are expressed in *Voigt* notation with microstructure defined as a hexagonal polygon with circular perforation acting as porosity. 45
4.3 Percentage errors between the homogenized coefficients and the PG reference case. The tensors are expressed in *Voigt* notation with 3-dimensional cubic microstructure and cylindrical subdomain describing the porosity. 47
4.4 RMSE results from time-domain simulations using a set of 8 (porosity, thickness) pairs homogeneously distributed on the space of biomedical interest. Explicitly, the **Axial Meas.** defines vertical measurements of displacement, **Anti-Axial Meas.** defines horizontal measurement of displacement, whereas **Composed** defines measurement of maximum values between each of the two above, thus being of mixed type. 54
4.5 RMSE results from frequency-domain simulations using a set of 8 (porosity, thickness) pairs homogeneously distributed on the space of biomedical interest. Explicitly, the **Axial Meas.** defines vertical measurements of displacement, **Anti-Axial Meas.** defines horizontal measurement of displacement, whereas **Composed** defines measurement of maximum values between each of the two above, thus being of mixed type. 56

List of Figures

1.1 Real samples of μ-CT transverse cross section images, with thickness $Ct.Th$ and porosity $Ct.Po$ labels, obtained from processing of the μ-CT images itself [15]. They define the standard clinical procedure for parameter measurement. 3

1.2 Schematic Procedure. From the experimental device to the homogenize idealization of the cortical bone. 5

1.3 On the left side, objective functional from figure (1.1) associated to the minimization problem (1.1) is shown with best acquisition of (Po, Th) parameters. The obtained values by μ-CT and ultrasound technique (US) are indicated in the (Th, Po) plane with black circles and gray triangles respectively. On the right side, experimental $L_4(f, k)$ dispersion curves (dots) with the guided modes (continuous and dashed lines) are shown fitting to the reference *Lamb*-curves [15]. 7

1.4 Two-Scale homogenization assumption for the microstructure, defining it as a highly oscillatory composite material of bone with matrix part C^m_{ijkl} and fluid on C^f_{ijkl}, periodically distributed along the the anti-plane symmetric over the long-axis of bone. 9

4.1 Main diagonal elastic homogenized coefficients in *Voigt* notation. They describe an transverse isotropic behavior, spanned in the figure on the biomedical range of $(1, 30)[\%]$ cortical porosity. The characteristic microstructure in this case is of unitary square. The blue, orange lines describe the FEM predictions at different mesh sizes, whereas the green line describes the PG approximation. 43

4.2 Other diagonal elastic homogenized coefficients in *Voigt* notation. They describe an transverse isotropic behavior, spanned in the figure on the biomedical range of $(1, 30)[\%]$ cortical porosity with unitary square characteristic microstructure. 43

4.3 Main diagonal elastic tensor coefficients in *Voigt* notation. The figure shows the prediction values over the range $(1, 30)[\%]$ of porosities with characteristic microstructure defined by an hexagonal 2-dimensional polygon. The blue, orange lines describe the FEM predictions at different mesh sizes, whereas the green line describes the PG approximation. 44

4.4 Shear type elastic homogenized coeffs. in *Voigt* notation. The figure shows the behavior over the range $(1, 30)[\%]$ porosity with characteristic microstructure described by a hexagonal 2-dimensional polygon. 45

4.5 Main diagonal elastic tensor coefficients in *Voigt* notation. It describes prediction values over the range $(1, 30)[\%]$ of porosities with 3-dimensional cubic characteristic microstructure. The blue, orange lines describe the FEM predictions at different mesh sizes, whereas the green line describes the PG approximation. 46
4.6 Main diagonal elastic tensor coefficients in *Voigt* notation. It describes prediction values over the range $(1, 30)[\%]$ of porosities with 3-dimensional cubic characteristic microstructure. The blue, orange lines describe the FEM predictions at different mesh sizes, whereas the green line describes the PG approximation. 46
4.7 On the left side, the input force in time domain while on the right side the input force in frequency domain. The implementation is done using $t_0 = 1[\mu s], \sigma_0 = 0.7[\mu s], f_0 = 1[Mhz]$ 48
4.8 Schematic setting of the numerical model to simulate. It contains the *Dirichlet* and *Neumann* boundary conditions for the elastodynamic problem. The mesh is done using `CGALs` library. 49
4.9 Simulated wave-guide stopped at time $31[\mu s]$. It shows in colors the intensity of the propagation wave along the rectangular domain and the interaction with the mixed boundary conditions imposed. This case is parametrized by $(6\%, 3.3[mm])$ porosity-thickness pair. 50
4.10 Numerically simulated (f, k)-diagram defined by the function $L_M(f, k)$ of a 2D transverse elastodynamic model. Setting of 8 sources with 3% porosity and thickness of $2.8[mm]$ with different number of modes $M > 0$. 50
4.11 Singular values obtained by the SVD decomposition of the recorded signal from the simulated diagram (4.10). It can be seen 8 different curves associated to each force source. 51
4.12 Numerically simulated (f, k)-diagram defined by the $L_M(f, k)$ functional of a 2D transverse elastodynamic model. Setting of 1 source with 6% porosity and thickness of $3.3[mm]$ with different M values. 52
4.13 Singular values obtained by the SVD decomposition of the recorded signal from the simulated diagram (4.12), describing the 8 simulated recording at the receptors. 52
4.14 Numerically simulated (f, k)-diagram of 2D elastodynamic Model. Setting of 1 source with 6% porosity and thickness of $3.3[mm]$ applying Hilbert transform to delete reflections. 53
4.15 Singular values obtained by the SVD decomposition of the recorded signal from the simulation (4.14), describing the 8 different recordings at the receptors. 54
4.16 Numerically simulated (f, k)-diagram of the $L_M(f, k)$ functional using a 2D frequency domain elastic model. Setting of 8 sources with 12% porosity and thickness of $2.8\,[mm]$ 55
4.17 Singular values obtained by the SVD decomposition of the recorded signal from the simulation (4.16), describing the 8 different recordings at the receptors containing resonances. 56
4.18 Comparison between Singular Values and Eigen-frequencies: Experimentally its found a increasing sequence of eigenvalues that intersects the experimentally chosen array frequencies. 57

4.19 Numerically simulated (f,k)-diagram of the $L_M(f,k)$ functional using a 2D transverse elastodynamic model. Setting of 8 sources with 12% porosity and thickness of 2.8$[mm]$ with different M values for signal intensity comparison. 58

4.20 Singular values obtained by the SVD decomposition of the recorded signal from the simulation (4.19), describing the 8 recorded attenuated signals. . . . 59

4.21 Half-Cylinder Mesh defining the geometry for the elastodynamic 1-source simulation with mean diameter of tetrahedral $\sim 40[\mu m]$. Number of vertices: $176,144$ and number of cells: $956,704$. The colors variations shows the different tagged subdomains describing the numerical implementation and recording on the receptors. In this case, from left to right it's shown source subdomain and force-sensors subdomains in array-like form. 60

4.22 Wrapping by vector effect on the simulated domain with input force $\mathbf{F}(\mathbf{x},t)$ at $8[\mu s]$. The color intensity described by the right-hand side bar shows the magnitude of displacement scaled at $[mm]$. 60

4.23 Numerically simulated (f,k)-diagram of the $L_M(f,k)$ functional using as 3-dimensional Half-cylinder elastodynamic model. Setting of 1 source with 11% porosity and $1.8\,[mm]$ thickness applying Hilbert transform to delete reflections. The inverse formulation retrieves $\sim 1.01\%$ of porosity and $\sim 1.801\,[mm]$ thickness. 61

4.24 Singular values obtained by the SVD decomposition of the recorded signal from the simulation (4.23). The different modes obtained from the decomposition are shown in different colors, being the first 3 related to the naturally obtain from real *ex-vivo* results. 61

4.25 Data-Flow. The mesh generation involves a sequence of different software `Fiji, Octave, iso2mesh, CGAL` that used in sequence generates complex adaptive meshes that describe realistic geometries. 62

4.26 Mesh Generated from 1000 Slices from $\mu-CT$ images using the mesh-generation diagram (4.25). It characterizes a cortical bone sample of $56\,[mm]$ length in the long direction associated to a thickness $\sim 1.8[mm]$ and experimentally tested porosity of $\sim 11\%$. Explicitly, the mesh is described by $432,280$ vertices with $1,393,709$ tetrahedrons. 63

4.27 The colors markers define the different subdomains associated to the mesh (4.26). It is described 48 receivers and a transmitter locations in a array-like form resembling the experimental transducer. Moreover, each subdomain is defined approximately by ~ 200 marked tetrahedral cells. 64

4.28 The elastodynamic simulation over the irregular mesh is shown at instant $32\,[\mu s]$, characterizing the wave-front propagation using a intensity color-scheme. The right-hand side bar contains the scale over the simulation, at $0.056\,[mm]$ associated to the voxel size. 64

4.29 Numerically simulated (f,k)-diagram of the $L_M(f,k)$ functional using a 3-dimensional realistic-geometry. Setting of one-source with 11% porosity and $\sim 1.8[mm]$ thickness. The green lines defines *Lamb* curves created from recording of the wave-guide being the others associated to a reference model. 65

4.30 Singular values obtained by the SVD decomposition of the recorded signal from the simulated diagram (4.23), describing the 8 recordings at the receptors. 65

5.1 Predicted behavior for the viscoelastic model. It is shown on the left figure the predicted quality factors for a *Kelvin-Voigt* model; the center figure a prediction of homogenized coefficient ratios, and on the right figure some homogenized shear ratios with behavior as in [6]. 71
5.2 The effects from cell-problem solutions is shown for some representative quality factors accounting the linear and non-linear contributions over the range of biomedical interest. 72
5.3 Predicted behavior for the viscoelastic model. It is shown in the left figure the predicted quality factors for a *Kelvin-Voigt* model; the center figure a prediction of homogenized coefficient ratios, and in the right figure some homogenized shear ratios behaves as in [6] 72

Introduction

In the context of mechanical behavior in medicine, there are abundant question to answer, fluctuating from the mathematical modelling itself of different tissues, physiological structures, simulation of its experimental procedures to the verification and prediction of different factor of clinical interest such as density, stiffness constants, etc. From a computational modelling point-of-view, biological tissues define complex multiscale problems since there are multiple physical phenomena acting at various scales. Moreover, from the bast majority of clinical applications the materials are viewed in its continuous setting, thus the importance to contribute with mathematical models and numerical procedures to characterize non-trivial properties arising from the microscopic structures that affect the overall behavior in terms of elasticity or viscosity. One of particular interest is the human bone, an absorbing complex composite structure that has irregular hollow-like interior filled with marrow, surrounded by soft tissue and muscles. Over it is defined the so-called bone quality, a composite of properties that enables bone to resist fracture. In this sense, when more bone is removed than added in the same time span, the so-called *osteoporosis* condition appear, a established and well-defined disease from the World Health Organization, affecting more than 75 million of people in Europe, United States and Japan combined, being the major cause of fractures.

Nowadays, noninvasive ultrasound techniques corresponds to a unique and important aspect in the biomedical research and applications, as it allows detailed insight of important bone parameters with a lower-cost, non-invasive and non-radiative properties that expects to challenge the gold-standard techniques used in clinical procedures. Under this setting, *Minonzio et. al.* [15] proposed a technique of wave-guide propagation to recover two relevant parameters that describe bone quality, the porosity and thickness of cortical bone using an inverse-like problem formulation. Several questions must be addressed to successfully validate the technique, ranging from the studies of underlying theory used, the effect of domain irregularities and robustness as well as the validation under controlled scenarios.

This work is oriented mainly in the modelling and numerical implementation of such novel ultrasound experimental procedure, in which via homogenization theory techniques it is studied the bone mechanical behavior and description using the *Lamb*-curves theory. Explicitly, by means of a two-scale asymptotic homogenization framework it is described the macroscopic equations governing the composite material that incorporates the intrinsic non-linear microstructural-driven behavior, defined by the so-called mesoscale.

By implementing the ultrasound experimental procedure proposed from *Minonzio, Foiret* [12], [15] with a state-of-art library `FEniCS` [13], it is simulated *Lamb*-mode curves and sin-

gular values resembling real behavior, assessing the parameter dependency and fidelity. In this context, it is studied properties of the elastic operator to account effects of resonance behavior in the frequency domain and instabilities observed in their spectral decomposition. Similarly, numerically obtained homogenized elastic coefficients that model the effective mechanical behavior are compared with the reference literate, providing a standpoint towards further modification regarding symmetry and domain configuration. Finally, from a theoretical stand-point it is studied the justification of the two-scale asymptotic expansion concluding with a convergence result, relating the multiscale solution of the composite material and the homogenized solution. Moreover the extension toward a viscoelasticity formulation is done with damping effects naturally appearing from the complex interaction between several tissues.

This thesis is organized as follows: **Chapter 1** contextualize the clinical measurements of bone within the novel ultrasound technique and defines the multiscale model used. **Chapter 2** introduces the two-scale homogenization heuristic providing convergence results and studies of properties derived from the homogenized elastic coefficients. **Chapter 3** introduces the discretization procedures used for all the numerical implementations. **Chapter 4** provide results and validation of the numerical simulations done for each case studied. Finally, **Chapter 5** describes the extension towards a viscoelastic formulation of bone, with justification and numerical results comparable to state-of-art literature.

Chapter 1

Context: Clinical Measurements

Cortical Bone is a highly organized, hard and lightweight tissue representing approximately 80% of the skeletal mass in an human adult defined by an hierarchy of micro-structures. From a functional description, scaling down to nanometers it is observed important structures for the cortical tissue such as haversian systems, osteons, lamellae, collagen fibres, fibrils and elementary mineral constituents with water [18].

The standard description associated to a mechanical point of view is defining it as a two-phase composite material: a soft phase mainly of pores, containing organic fluid and soft tissues as cells, blood vessels, and a complex hard matrix phase with nerves distributed inside, being the matrix consisting mainly of hydroxyapatite and collagen. Porosity is distributed over various length scales, nevertheless only the two largest pores types: resorption cavities (with size of approx. $50 - 200[\mu m]$) and haversian canal (size of approx. $50[\mu m]$) contribute to the so-called mesoscale structure and the mechanical behavior of the cortical bone itself, hence the mesoscale porosity which is characteristic of the higher level of bone organization shown in figure (1.1).

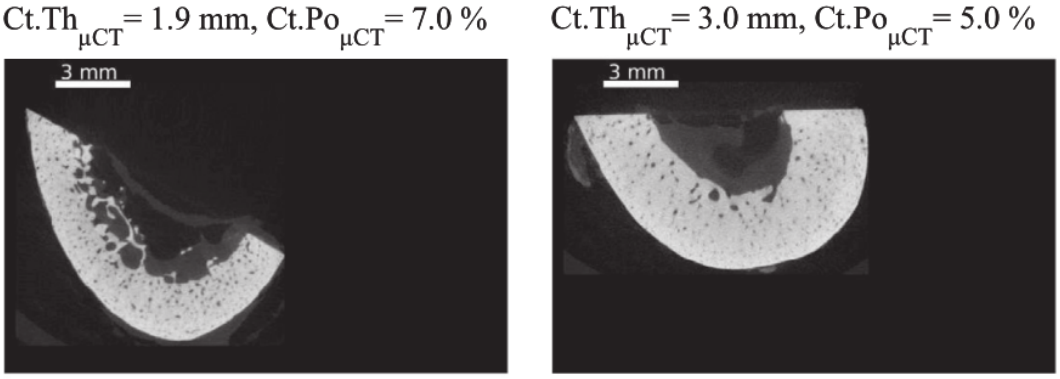

Figure 1.1: Real samples of μ-CT transverse cross section images, with thickness $Ct.Th$ and porosity $Ct.Po$ labels, obtained from processing of the μ-CT images itself [15]. They define the standard clinical procedure for parameter measurement.

The study of such tissue gives us insights of various clinical parameters such as its microstructure, accumulated stress damage, collagen quality, bone turnover and others necessary to diagnosis the status and quality of the bone itself, therefore the early diagnose of osteoporosis, a condition where less bone is added than taken away leading to skeletal fragility and increasing risk of fractures.

The early detection and prevention are important aspect of investigation. Dual X-ray Absorptiometry (DXA) provides the Bone Mineral Density (BMD) used to diagnose osteoporosis, defining the actual gold-standard. As DXA provides non-volumetric measures of bone quality, for fidelity X-ray Quantitative Computed Tomography (QCT) is used to assess volumetric bone density, but is rather expensive with radiation costs involved. To overcome such aspects, new ultrasound techniques have been developed to assess relevant parameters of bone quality. It describes a lower cost, non-invasive and non-radiative novel methodology that expects to reach gold-standard predictions. But validations must be obtained and robustness research must be taken in consideration.

Under such setting, modelling and computational simulations of cortical tissues enables us to go further and test such new procedures, validate under specific environments the possible outcomes and therefore assure the fidelity of results to clinical usage.

1.1 Time-domain Modelling

Sophisticated quantitative ultrasound (QUS) approaches under study [12] [15], are based on the axial transmission measurements which consist of guided waves recordings that propagate into and through the cortex in response to an ultrasonic excitation produced at the surface, then studying their response in the form of dispersion curves [1], i.e., by means of the *Lamb*-waves nonlinear equations [20]. Wave-guide characteristics such as thickness and porosity can then be deduced from the dispersion curves by finding the best fitting of theoretical wave-guide model to experimental data after a signal processing step. Such procedure in particular defines the inverse problem under consideration.

In this section, it is described the experimental procedure used to study two bone mechanical properties by means of a ultrasound transducer. It is also given a brief explanation of the setting involved in the clinical procedure and the assumptions being done to model the recorded signal then processed by a spectrum technique.

1.1.1 Experimental Procedure

Bone samples are subjected to the transmission of the wave-guide, i.e., a wave propagation from the external surface generated by a transducer device. Explicitly such force can be

[1] From a physical perspective, its represented as the variation of wave number $k = 2\pi f/c(f)$ as function of the frequency $f \in [0, 2]$ being $c(f)$ the phase velocity of the mode.

considered in the form:

$$\mathbf{F}(t,\mathbf{x}) = A\mathrm{e}^{-\frac{(t-t_0)^2}{2\sigma_0^2}} cos(2\pi f_0(t-t_0)) \text{ on } \Gamma_N$$

where $A > 0$ denotes an amplitude, $t_0 > 0$ a central time, $f_0 > 0$ frequency, $\sigma_0 > 0$ a fixed variance and Γ_N surface boundaries where the force is applied.

Even though the shape of long segments of cortical bone is not uniform with respect to thickness nor in its surface, by the device shape and size it is assumed that such local spatial variations in the geometry are minimum and moreover can be neglected [12]. Moreover, as the transducer device captures wave-front measurements over the long axis of bone, the propagation effects given on the non-axial (or anti-plane) are assumed to not add more relevant features, thus the natural 3-dimensional cylindrical-like shape of bone can be simplified without affecting the overall behavior of interest to a 2-dimensional plate shape domain modelling the coronal cut plane of propagation.

For such 2-dimensional wave-guide model, the propagation is studied by means of the homogenization technique in elastic and viscoelastic behaviors. Such a homogenization procedure results necessary since the size of microstructure generates restrictive computational costs, and moreover the ability of such theory to model the microstructure observed for example in (1.1), i.e., containing the porosity level implicitly in the elastic coefficients. Schematically, figure (1.2) describes the experimental procedure and the assumptions on the cortical tissue.

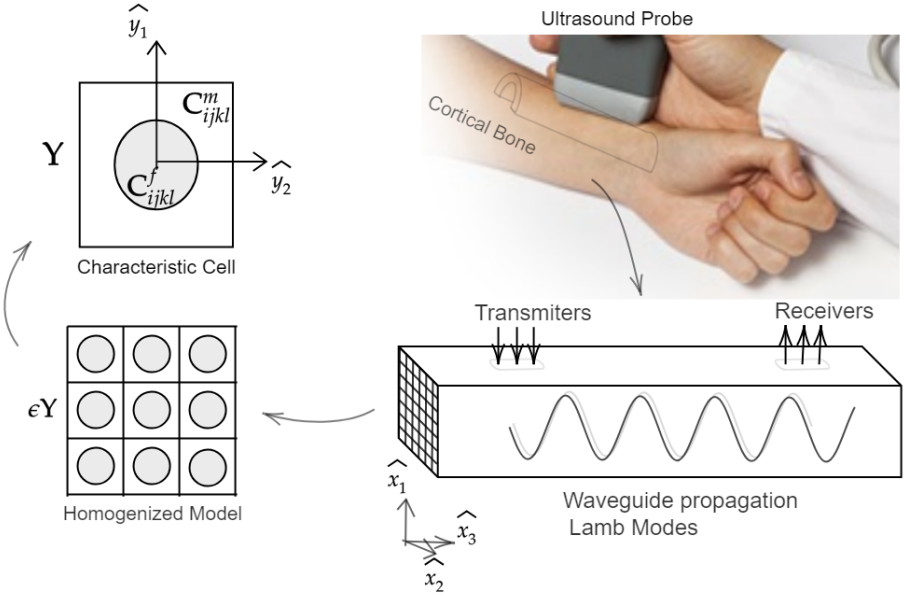

Figure 1.2: Schematic Procedure. From the experimental device to the homogenize idealization of the cortical bone.

The important aspect of the transducer is the linear element array which contains several emitters and receiver which defines the signal recovery. Finally, it is modeled the experi-

mental setting of the transducer applied on patients as an elastodynamic model defined on the cortical bone, moreover it is neglected the effects at the interface with the skin. The excitation generated at the surface by the transducer is produced by different force-sources acting independently, more explicitly by an array of 5 to 8 source-forces generating each one a wave propagation, enabling the posterior recordings at the receiver locations. Nevertheless, by assuming symmetric and regular domains, each wave propagation has similar mechanical effects by the translation invariance properties of the elastic wave which enables us to reduce time-costs for numerical implementations.

1.1.2 Signal Processing

Each cycle of measurements consists of a sequential excitation of $N^E > 0$ number of emitters located at boundaries $\Gamma_{\mathrm{e_i}}$ for each $\mathrm{i} \in \{1, \dots, N^E\}$ where the device recordings take place. By denoting $N^R > 0, N^T > 0$ the number of receivers and number of discretization steps respectively, the device yields $N^T \times N^R$ arrays from each emitter. In the following, $\mathcal{M}_{A,B}$ will denote the space of matrices of dimensions $A, B \in \mathbb{N}$ with values in $\mathbb{R}$.

Such signal generated by the excitation of each emitter $m \in \{1, \dots, N^E\}$ denoted by $s_m(t, \mathbf{x})$ at fixed time t and receptor position $\mathbf{x}$, is *Fourier* transformed to the frequency domain $\mathcal{F}_t[s_m(\cdot, \mathbf{x})](f) := S_m(f, \mathbf{x})$ at fixed $f \in \mathbb{R}_+$, associated to a frequency discretization bandwidth of $N^F > 0$ steps.

The spectral description of the propagated wave-front which allows comparison regarding the *Lamb*-waves [2] is obtained from a Singular Vector Decomposition (SVD) over the signal $\{S_n(t, \mathbf{x})\}_{n \in [N^E]}$. Explicitly, the signal array is decomposed in the form:

$$S_n = U_n \sigma_n D_n, \quad n \in \{1, \dots, N^E\}$$

being each array $U_n \in \mathcal{M}_{N^F \times N^F}, \sigma_n \in \mathcal{M}_{N^F \times N^R}, D_n \in \mathcal{M}_{N^R \times N^R}$ associated to the number of frequency N^F and receptor N^R discretizations. The singular value bases $(U_n)_n$ are then used to define a function for frequency-wavenumber pairs $(f, k) \in \mathbb{R}_+ \times \mathbb{R}$ in the form:

$$L_N(f, k) = \sum_{n=1}^{N} \left| \langle U_n(f, \mathbf{x}) \,|\, \mathrm{e}^{\mathrm{i}k\mathbf{x}} \rangle \right|^2$$

being $0 < N \leq N^E$ the mode number intensity, allowing the description of wave-modes recording on the (f, k) space by applying the plane wave projector operator over the bases U_n. In particular, since the wave-number k is dependent on the material properties (Th, Po) pair then it arises the experimentally obtained dispersion curves described by $L_N(f, k(Po, Th))$ enabling comparison to the *Lamb*-wave material curves.

Experimentally, right column on figure (1.3) shows two particular cases of dispersion-curves recordings, each describing the symmetric and anti-symmetric modes characteristic of each material and the fitting with its corresponding *Lamb*-curves.

[2] Several studies consider the usage of this kind of curves, as ones mainly used to describe the material destruction and mechanical behavior, and moreover in a non-invasive form [20].

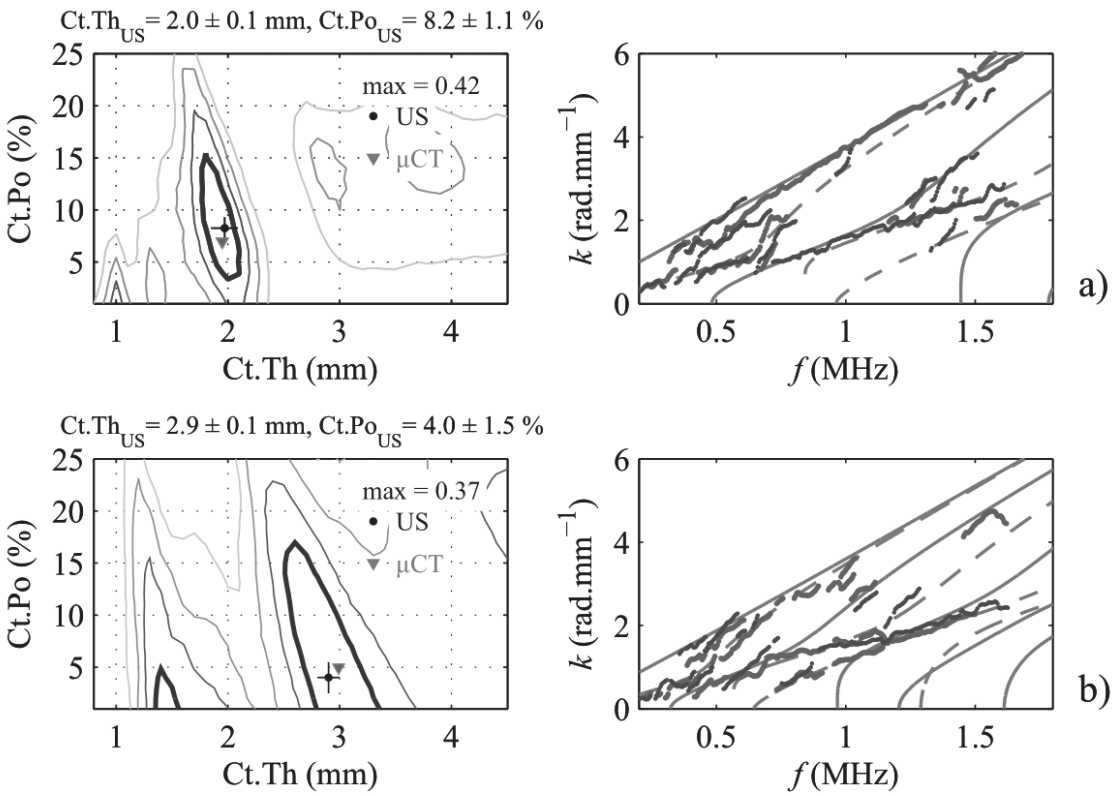

Figure 1.3: On the left side, objective functional from figure (1.1) associated to the minimization problem (1.1) is shown with best acquisition of (Po, Th) parameters. The obtained values by μ-CT and ultrasound technique (US) are indicated in the (Th, Po) plane with black circles and gray triangles respectively. On the right side, experimental $L_4(f, k)$ dispersion curves (dots) with the guided modes (continuous and dashed lines) are shown fitting to the reference *Lamb*-curves [15].

Thus, the parameter recuperation (or inverse problem) from recorded signals is defined by the optimization problem:

$$(Po^*, Th^*) = \underset{(Po,Th)\in\mathcal{A}}{\operatorname{argmax}} \int_{f_{min}}^{f_{max}} \frac{1}{N} \sum_{m=1}^{M} L_N(f, k_m(Po, Th))\, \mathrm{d}f \tag{1.1}$$

being $M > 0$ the number of modes and $\mathcal{A}$ the space of porosity $\times$ thickness pairs. Therefore, the formulation is re-expressed as the recuperation of $(Th.^*, Po.^*)$ two relevant biomedical parameters describing the quality of cortical bone. Experimentally, left column of figure (1.3) describes the objective functional and optimal values obtained in two different experimental measurements (US) with close to gold-standard predictions (μCT).

An important aspect of such *Lamb* curves is the fact that implicitly contains the overall mechanical behavior of the elastodynamic model, allowing to define a useful tool for validation and comparison of numerical simulation with respect to real data [20]. Over such a domain it is considered their behaviour of linear elastic type, defined by a displacement $u(\mathbf{x}, t)$ with constitutive equation following *Hookes* law and forces $\mathbf{F}(t)$ applied at a section of the surface.

1.2 Main assumptions and Multiscale Modelling

Computational modelling of biological tissues (in particular of bone) is a complex multiscale problem, since there are multiple physical phenomena interacting at various scales. Moreover, in a bast majority of clinical applications the material is viewed as continuum, thus it is important to contribute with a mathematical model and numerical procedures to characterize non-trivial properties arising from the microscopic geometrical structures affecting the overall behavior in terms of effective elasticity or viscosity.

Formally, it is considered the following: Let a bounded domain $\Omega \subset \mathbb{R}^{\mathrm{d}}$ ($\mathrm{d} = 2, 3$) represent the composed material under study, modeled by an elastic matrix with several inclusion defining the so-called mesoscale, being described mechanically as a elastic material with cylindrical shape structures periodically distributed. For the sake of the experimental setting under consideration, the exterior boundary $\partial\Omega$ is decomposed as

$$\partial\Omega = \Gamma_D \dot{\cup} \Gamma_N$$

denoting Γ_D, Γ_N the Dirichlet and Neumann part of the exterior boundary respectively.

Furthermore, let the small parameter $0 < \varepsilon \ll 1$ denote the aspect ratio between the macroscopic variable $\mathbf{x} \in \Omega$ and the microscopic one $\mathbf{y}$ in the form: $\mathbf{y} = \frac{\mathbf{x}}{\varepsilon}$ being $\mathbf{y} \in \mathbf{Y}$ and $\mathbf{Y} = (0,1)^{\mathrm{d}}$ the cell structure. In this configuration, the unitary cell $\mathbf{Y}$ can be decomposed as

$$\mathbf{Y} = \mathbf{Y}_m \cup \Gamma \cup \mathbf{Y}_f$$

where $\mathbf{Y}_m$ and $\mathbf{Y}_p$ are defined as the domains occupied by the matrix and porous part respectively, and Γ denotes the interface between them[3].

Such a cell is assumed to be periodically distributed along the material, defining its highly oscillatory structure, suitable to the usage of homogenization framework. It is considered the composite material under study with elastic properties having oscillation rate ε, represented in the domain decomposition:

$$\overline{\Omega} = (\overline{\Omega} \setminus \Omega_1^\varepsilon) \cup \overline{\Omega}_1^\varepsilon$$

defined by:

$$\overline{\Omega}_1^\varepsilon = \bigcup_{\mathbf{x} \in \mathbf{T}_\varepsilon} \varepsilon(\mathbf{x} + \mathbf{Y})$$

being the tessellation $\mathbf{T}_\varepsilon$ the subset in $\mathbb{Z}^{\mathrm{d}}$ of all points satisfying the conditions

$$\varepsilon(\mathbf{x} + \mathbf{Y}) \subset \Omega, \quad \rho(\varepsilon(\mathbf{x} + \mathbf{Y}), \partial\Omega) \geq \varepsilon$$

Let us note in particular that for fixed $\varepsilon > 0$ and all $\mathbf{x} \in \Omega$ there is a unique decomposition $\mathbf{x}/\varepsilon = \mathbf{x}_{\mathbf{T}_\varepsilon(\mathbf{x})} + \mathbf{y}$ where $\mathbf{x}_{\mathbf{T}_\varepsilon(\mathbf{x})}$ denotes the element in Ω of the tessellation.

[3]This model is inspired in the development of the Homogenization of the elastic operator in a porous media proposed on [9]. Nevertheless, this kind of configurations are typical in the two-scale homogenization literature [17], [7] to mention updated references.

The above considerations allow us to define finally the material coefficients as second order rank tensors for component $\mathrm{i}, j, k, l \in \{1, \ldots, \mathrm{d}\}$ in the form:

$$C_{\mathrm{i}jkl}(\frac{\mathbf{x}}{\varepsilon}) = C_{\mathrm{i}jkl}(\mathbf{y}) \quad \text{for } \frac{\mathbf{x}}{\varepsilon} = \mathbf{x}_{\mathbf{T}_\varepsilon(\mathbf{x})} + \mathbf{y},\ \mathbf{x} \in \Omega_1^\varepsilon$$

and being $C_{\mathrm{i}jkl}(\frac{\mathbf{x}}{\varepsilon}) = C^m_{\mathrm{i}jkl}$ if $\mathbf{x} \in \overline{\Omega} \setminus \Omega_1^\varepsilon$.

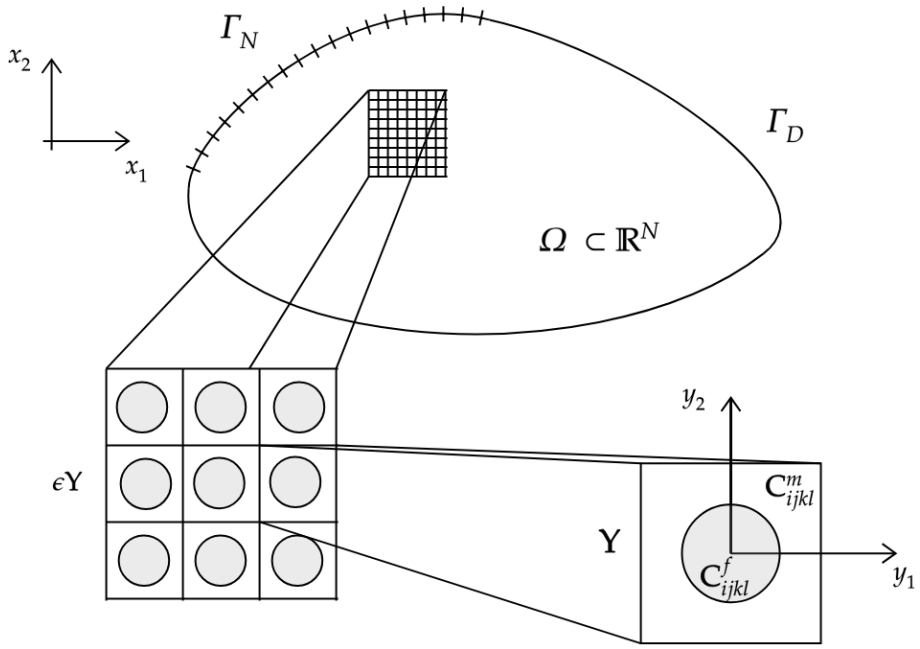

Figure 1.4: Two-Scale homogenization assumption for the microstructure, defining it as a highly oscillatory composite material of bone with matrix part $C^m_{\mathrm{i}jkl}$ and fluid on C^f_{ijkl}, periodically distributed along the the anti-plane symmetric over the long-axis of bone.

Remark The material is assumed to be confined within the inclusion as a elastic (emulating a mechanical behavior of blood mixture mainly made of saturated static fluid) with volume $\varepsilon^{\mathrm{d}}|\mathbf{Y}_f|$ embedded in a elastic material (modeled mainly of hydroxipatite and collagen) filling a unit cell of volume $\varepsilon^{\mathrm{d}}|\mathbf{Y}|$. It is defined, after scaling, the porosity associated to the material as the fraction of volume occupied by the gas in the unitary cell, i.e.,

$$\phi = \frac{|\mathbf{Y}_f|}{|\mathbf{Y}|} = |\mathbf{Y}_f|$$

which will define the material coefficients dependent of such parameters.

Thus, denoting the observed displacement $u(\mathbf{x}, t) \in \mathbf{H}^1(\Omega)$ with behaviour of linear elastic type subjected to surface forces $\mathbf{F}(t) \in L^2(0, T)$, the material is assumed to behave following

the system of partial differential equations (PDE's) in the form:

$$\begin{cases} \rho(\dfrac{\mathbf{x}}{\varepsilon})\partial_{tt}u^{\varepsilon}(\mathbf{x},t) - \nabla \cdot \sigma(u^{\varepsilon}(\mathbf{x},t)) = \mathbf{0}, \text{ in } (0,T)\times\Omega \\ \sigma(u^{\varepsilon}(\mathbf{x},t))_{\mathrm{i}j} = \mathbf{C}_{\mathrm{i}jkl}(\dfrac{\mathbf{x}}{\varepsilon})\mathbf{e}_{kl}(u^{\varepsilon}(\mathbf{x},t)) \text{ in } (0,T)\times\Omega \\ u^{\varepsilon}(\mathbf{x},t) = \mathbf{0} \text{ on } (0,T)\times\Gamma_D \\ \sigma(u^{\varepsilon}(\mathbf{x},t))\cdot n = \mathbf{F}(t) \text{ on } (0,T)\times\Gamma_N \end{cases}$$

where $\mathbf{C}(\mathbf{x})$ denotes the elasticity tensor, $\rho(\mathbf{x})$ the material density and $\mathbf{e}(u(\mathbf{x},t)) = \frac{1}{2}\big(\nabla u(\mathbf{x},t) + \nabla u(\mathbf{x},t)^T\big)$ the symmetric gradient, each at position $\mathbf{x}$ and time $t \in (0,T)$. As shown, the clear dependency on the ε scale requires a more complex framework to successfully implement a feasible numerical model, which will be the two-scale asymptotic theory, developed in the next chapter. In all the following chapters it is assumed sum convention over repeated indices at each expression, except if the opposite is stated.

Chapter 2

Homogenization and Justification

Mechanical models of highly periodic structures within the asymptotic homogenization theory, which defines a multi-scale method for determining the effective moduli of periodic media, have been studied profoundly for example by *Bakhvalov, Panasenko* [5]. The approach exploits a separation of scales within the composite material, deriving a leading order homogenized equations governing the effective macroscopic behavior.

Given the assumptions for the multiscale elastodynamic model of cortical bone, the objective in this section will be to rigorously give a justification of the existence of such multiscale PDE system motivated from [4], [18] then show the schematic procedure to obtain the so-called macroscopic mechanical behavior of bone which will be used for the numerical simulations and finally give a convergence result of the solution between the multiscale model and the homogenized one.

First, let us define the adequate spaces for our problem. Given the domain $\Omega \subset \mathbb{R}^{\mathrm{d}}$, it will be denoted by $\mathbf{L}^2(\Omega)$ the d-dimensional vector functions, being each component on $L^2(\Omega)$. Similarly, it is defined the space $\mathbf{H}^1(\Omega)$ of d-dimensional vector functions, where as before, each component belongs to $H^1(\Omega)$ defined as usual in the literature [11]. In particular, denoting the vector trace operator by $\gamma : \mathbf{H}^1(\Omega) \to \mathbf{L}^2(\partial\Omega)$, we can define the space:

$$\mathbf{H}^1(\Omega, \Gamma_D) = \left\{ v \in \mathbf{H}^1(\Omega) \,|\, \gamma(v)|_{\Gamma_D} = \mathbf{0} \right\}$$

Moreover, by applying the *Rellich-Kondrachov* theorem, the embedding from $\mathbf{H}^1(\Omega, \Gamma_D)$ into $\mathbf{L}^2(\Omega)$ is compact [1].

Given $\varepsilon > 0$, let us fix a porosity $p \in (0, 1)$ and consider $(C_{ijkl})_{ijkl} := \mathbf{C}(p) \in \ \mathrm{lin}\big(\mathbf{Sym}^{\mathrm{d}\times\mathrm{d}}\big)$, the space of linear, continuous operators on the d $\times$ d symmetric matrices space, being

[1] From a more abstract point of view, it is possible to define $\kappa : \mathbf{L}^2(\Omega) \longrightarrow \mathbf{H}^{-1/2}(\Gamma_D)$ being the trace operator, i.e., $\kappa(u) = u|_{\Gamma_D}$. Then define an adequate space of square integrable vector functions with homogeneous Dirichlet condition on Γ_D by $\mathbf{L}^2(\Omega, \Gamma_D) := \kappa^{-1}\big(\{\mathbf{0}\}\big)$. Note that the operator κ defined is linear and continuous in the corresponding spaces, moreover, since $\{\mathbf{0}\}$ is a close subset, then $\mathbf{L}^2(\Omega, \Gamma_D)$ is a close subspace of $\mathbf{L}^2(\Omega)$. In particular, $\mathbf{L}^2(\Omega, \Gamma_D)$ is separable, so that there exist a Hilbertian base associated.

uniformly elliptic and bounded elasticity tensors. Also, denote by $\rho^\varepsilon(\mathbf{x}) = \rho\left(\frac{\mathbf{x}}{\varepsilon}\right)$ an uniformly bounded density, $C^\varepsilon_{ijkl}(\mathbf{x}) = C_{ijkl}(\frac{\mathbf{x}}{\varepsilon})$, $\mathbf{F}(t,\mathbf{x})$ a force independent of ε and consider for fixed parameter $T>0$ the following evolution PDE problem modelling the displacements:

$$\left\{\begin{array}{cc} \rho^\varepsilon \partial_{tt} u^\varepsilon - \nabla\cdot\sigma^\varepsilon(u^\varepsilon) = \mathbf{0} & \text{in } (0,T)\times\Omega \\ \sigma^\varepsilon_{ij}(u^\varepsilon) = C^\varepsilon_{ijkl}\mathbf{e}_{kl}(u^\varepsilon) & \text{in } (0,T)\times\Omega \\ u^\varepsilon = \mathbf{0} & \text{on } (0,T)\times\Gamma_D \\ \sigma^\varepsilon_{ij} n_j = \mathbf{F} & \text{on } (0,T)\times\Gamma_N \\ \partial_t u^\varepsilon = u^\varepsilon = \mathbf{0} & \text{on } \{t=0\}\times\Omega \end{array}\right. \tag{2.1}$$

Proposition 2.1 *Assuming $0<\rho_0\leq\rho\left(\frac{\mathbf{x}}{\varepsilon}\right)<+\infty$ and $\mathbf{F}\in L^\infty(0,T;\mathbf{L}^2(\Omega,\Gamma_N))$, there exist a unique solution u^ε to (2.1) for each $\varepsilon>0$, such that*

$$u^\varepsilon \in \mathcal{C}^0(0,T;\mathbf{H}^1(\Omega,\Gamma_D))\cap\mathcal{C}^1(0,T;\mathbf{L}^2(\Omega))$$

Remark Inspired from [19], a constructive proof is given based in the spectral decomposition of the elastic operator on $\mathbf{H}^1(\Omega,\Gamma_D)$ and solutions of the reduced ODE's associated to each eigenvalue[2].

In the following, it is denoted the dot product $(u,v)_\Omega := \int_\Omega \rho^\varepsilon u\cdot v\,\mathrm{d}\mathbf{x}$ for $u,v\in\mathbf{L}^2(\Omega)$, which is equivalent to the usual one of $\mathbf{L}^2(\Omega)$ for each ε by the assumptions of boundness on the density. On the other hand, $(\cdot,\cdot)_{\Gamma_N}$ denotes the usual dot product of $\mathbf{L}^2(\Gamma_N)$ vector functions.

Under such notation, problem (2.1) can be rewritten in variational form satisfied in distributions over $(0,T)$ by:

$$\begin{array}{cc} \text{Find } u^\varepsilon\in\mathcal{C}^0(0,T;\mathbf{H}^1(\Omega,\Gamma_D))\cap\mathcal{C}^1(0,T;\mathbf{L}^2(\Omega)) & \text{s.t.} \\ \partial_{tt}(u^\varepsilon(t),v)_\Omega + \mathcal{I}_C(u^\varepsilon(t),v) = (\mathbf{F}(t),v)_{\Gamma_N} & \forall v\in\mathbf{H}^1(\Omega,\Gamma_D) \\ \partial_t u^\varepsilon(0) = u^\varepsilon(0) = \mathbf{0} & \end{array} \tag{2.2}$$

being $\mathcal{I}_C(u,v) := \int_\Omega C^\varepsilon_{ijkl}\mathbf{e}_{kl}(u^\varepsilon(t))\partial_{x_j}v_i$. Let us prove the existence and uniqueness of solution for (2.2).

Proof. 1. To this end, it will be considered approximate solutions to (2.2). It is defined the subspace V_m generated by the first $m\in\mathbb{N}$ eigenvectors $\{w_1,\ldots,w_m\}$ being $(w_i)_{i\in\mathbb{N}}\subset\mathcal{C}^\infty(\Omega)$ a Hilbertian base of $\mathbf{H}^1(\Omega,\Gamma_D)$ were the regularity follows from bootstrap and by the Sobolev embedding. Then, let us consider the problem in time, defined by:

$$\begin{array}{cc} \text{Find } u^\varepsilon_m : t\in(0,T)\longrightarrow u_m(t)\in V_m & \text{s.t.} \\ \partial_{tt}(u^\varepsilon_m(t),v)_\Omega + \mathcal{I}_C(u^\varepsilon_m(t),v) = (\mathbf{F}(t),v)_{\Gamma_N} & \forall v\in\mathbf{H}^1(\Omega,\Gamma_D) \\ \partial_t u^\varepsilon_m(0) = u^\varepsilon_m(0) = \mathbf{0} & \end{array} \tag{2.3}$$

Remark Note that the linear operator $b(t)(v) := (\mathbf{F}(t),v)_{\Gamma_N}$ is well-defined and moreover continuous on $\mathbf{H}^1(\Omega,\Gamma_D)$ for each $t\in(0,T)$. This follows from the trace theorem

[2]The formulation of the elastodynamic problem with Dirichlet boundary conditions had been studied in literature, in particular on the multiscale works from [17], [5]. On the other hand, the formal study of Neumann boundary conditions has been done mainly on [16].

applied on $\mathbf{H}^1(\Omega,\Gamma_D)$ since $\forall t\geq 0$, we have the bounds:

$$\begin{aligned}|b(t)(v)| &\leq \|\mathbf{F}(t)\mathbb{I}_{\Gamma_N}\|_{\mathbf{L}^2(\partial\Omega)}\|\gamma(v)\|_{\mathbf{L}^2(\Gamma_N)}\\ &\leq \|\mathbf{F}\|_{\mathbf{L}^\infty(0,T;\mathbf{L}^2(\Gamma_N))}\|\gamma(v)\|_{\mathbf{L}^2(\partial\Omega)}\\ &\leq \|\mathbf{F}\|_{\mathbf{L}^\infty(0,T;\mathbf{L}^2(\Gamma_N))}\|v\|_{\mathbf{H}^1(\Omega)}\\ &= \|\mathbf{F}\|_{\mathbf{L}^\infty(0,T;\mathbf{L}^2(\Gamma_N))}\|v\|_{\mathbf{H}^1(\Omega,\Gamma_D)}\end{aligned}$$

Defining $u_m^\varepsilon(t)=\sum_{\mathrm{i}=1}^m \alpha_\mathrm{i}^\varepsilon(t)w_\mathrm{i}$ with $\alpha_\mathrm{i}^\varepsilon(t)=(u_m^\varepsilon(t),w_\mathrm{i})_\Omega$ it follows that the functions $\alpha_\mathrm{i}^\varepsilon$ are solutions to the ODE system:

$$\begin{aligned}\partial_{tt}\alpha_\mathrm{i}^\varepsilon(t)+\lambda_\mathrm{i}\alpha_\mathrm{i}^\varepsilon(t)=(\mathbf{F}(t),w_\mathrm{i})_{\Gamma_N}\quad \forall t\in(0,T)\\ \partial_t\alpha_\mathrm{i}^\varepsilon(0)=\alpha_\mathrm{i}^\varepsilon(0)=0\end{aligned}\tag{2.4}$$

being $(\lambda_\mathrm{i})_{\mathrm{i}\geq 1}$ a positive, increasing sequence of eigenvalues associated to the decomposition of the operator $\mathcal{I}_C(\cdot,\cdot)$.
Let us note by applying the variation of parameters technique, that the solution to (2.4) is given in the form:

$$\alpha_\mathrm{i}^\varepsilon(t)=\frac{1}{\sqrt{\lambda_\mathrm{i}}}\int_0^t sin(\sqrt{\lambda_\mathrm{i}}(t-s))(\mathbf{F}(t),w_\mathrm{i})_{\Gamma_N}\,\mathrm{d}s\tag{2.5}$$

so that, defining the matrix for $\omega\in\mathbb{R}$ by:

$$Q(\omega)=\begin{bmatrix}cos(\omega) & sin(\omega)\\ -sin(\omega) & cos(\omega)\end{bmatrix}$$

it is obtained the following relation for the solution and their derivative in the form:

$$\begin{bmatrix}\sqrt{\lambda_\mathrm{i}}\alpha_\mathrm{i}^\varepsilon(t)\\ \partial_t\alpha_\mathrm{i}^\varepsilon(t)\end{bmatrix}=\int_0^t Q\big(\sqrt{\lambda_\mathrm{i}}(t-s)\big)\begin{bmatrix}0\\ (\mathbf{F}(t),w_\mathrm{i})_{\Gamma_N}\end{bmatrix}\tag{2.6}$$

2. Next, the sequence $(u_m^\varepsilon)_{m\in\mathbb{N}}$ is of Cauchy type on the spaces $\mathcal{C}^0(0,T;\mathbf{H}^1(\Omega,\Gamma_D))$ and $\mathcal{C}^1(0,T;\mathbf{L}^2(\Omega))$.
Let m,p be two integers such that $p>m\geq 1$ then from (2.5) it follows that

$$\mathcal{I}_C(u_p^\varepsilon(t)-u_m^\varepsilon(t),u_p^\varepsilon(t)-u_m^\varepsilon(t))+|\partial_t(u_p^\varepsilon(t)-u_m^\varepsilon(t))_\Omega|^2=\sum_{\mathrm{i}=m+1}^p\big(\lambda_\mathrm{i}|\alpha_\mathrm{i}^\varepsilon(t)|^2+|\partial_t\alpha_\mathrm{i}^\varepsilon(t)|^2\big)$$

and since $Q(\omega)$ is an orthogonal matrix, from (2.6) it follows that

$$\big(\lambda_\mathrm{i}|\alpha_\mathrm{i}^\varepsilon(t)|^2+|\partial_t\alpha_\mathrm{i}^\varepsilon(t)|^2\big)^{1/2}\leq\int_0^t|(\mathbf{F}(t),w_\mathrm{i})_{\Gamma_N}|\,\mathrm{d}s\tag{2.7}$$

so that, by using the Cauchy-Schwatz inequality, it can be obtained

$$\begin{aligned}\lambda_\mathrm{i}|\alpha_\mathrm{i}^\varepsilon(t)|^2+|\partial_t\alpha_\mathrm{i}^\varepsilon(t)|^2&\leq 2\big(\int_0^t|(\mathbf{F}(t),w_\mathrm{i})_{\Gamma_N}|\,\mathrm{d}s\big)^2\\ &\leq 2t\int_0^t|(\mathbf{F}(t),w_\mathrm{i})_{\Gamma_N}|^2\,\mathrm{d}s\end{aligned}$$

from which it can be deduced the bound

$$\mathcal{I}_C\big(u_p^\varepsilon(t)-u_m^\varepsilon(t),u_p^\varepsilon(t)-u_m^\varepsilon(t)\big)+|\partial_t(u_p^\varepsilon(t)-u_m^\varepsilon(t))|^2\leq 2\sum_{\mathrm{i}=m+1}^{p}t\int_0^t|(\mathbf{F}(s),w_{\mathrm{i}})_{\Gamma_N}|^2\,\mathrm{d}s$$

Now, since $\mathbf{F}\in L^\infty(0,T;\mathbf{L}^2(\Gamma_N))$ it follows

$$\lim_{p,m\longrightarrow+\infty}\sum_{\mathrm{i}=m+1}^{p}\big\{T\int_0^T|(\mathbf{F}(s),w_{\mathrm{i}})_{\Gamma_N}|^2\,\mathrm{d}s\big\}=0$$

and by using the uniform ellipticity of the tensor $\mathbf{C}$, it can be concluded that $(u_m^\varepsilon(t))_{m\in\mathbb{N}}$ is a Cauchy sequence on the spaces $\mathcal{C}^0(0,T;\mathbf{H}^1(\Omega,\Gamma_D))$ and $\mathcal{C}^1(0,T;\mathbf{L}^2(\Omega,\Gamma_D))$.

3. Since the above spaces are complete, there exist $u^\varepsilon(t)$ limit as $m\longrightarrow+\infty$ of $u_m^\varepsilon(t)$ belonging to the spaces $\mathcal{C}^0(0,T;\mathbf{H}^1(\Omega,\Gamma_D))$ and $\mathcal{C}^1(0,T;\mathbf{L}^2(\Omega))$.
Let us see that u^ε effectively solves the problem (2.1). To do this, let $m\geq 1$ and consider $\psi\in\mathcal{D}(0,T)$, since $u_m(t)$ solves (2.4) it follows:

$$\int_0^T(u_m^\varepsilon(t),v)_\Omega\partial_{tt}\psi(t)+\int_0^T\mathcal{I}_C(u_m^\varepsilon(t),v)\psi(t)=\int_0^T(\mathbf{F}(t),v)_{\Gamma_N}\psi(t)$$

so that, in the limit as $m\longrightarrow 0$, the solution $u^\varepsilon(t)$ solves the problem

$$\int_0^T(u^\varepsilon(t),v)_\Omega\partial_{tt}\psi(t)+\int_0^T\mathcal{I}_C(u^\varepsilon(t),v)\psi(t)=\int_0^T(\mathbf{F}(t),v)_{\Gamma_N}\psi(t)$$

with $\partial_t u^\varepsilon(0)=u^\varepsilon(0)=0$ and the desired results follows. Moreover, continuity with respect to boundary data is obtained, since from (2.7) the solution $u^\varepsilon(t)$ in the limit satisfies the inequality

$$\big(\mathcal{I}_C(u^\varepsilon(t),u^\varepsilon(t))+|\partial_t u^\varepsilon(t)|^2\big)^{1/2}\leq\int_0^T\|\mathbf{F}(t)\|_{\mathbf{L}^2(\Gamma_N)}\,\mathrm{d}t\leq T\,\|\mathbf{F}\|_{L^\infty(0,T;\mathbf{L}^2(\Gamma_N)}$$

and by the uniform boundness of the tensor C, the following bound is obtained

$$\|u^\varepsilon\|_{L^\infty(0,T;\mathbf{H}^1(\Omega,\Gamma_D))}+\|\partial_t u^\varepsilon\|_{L^\infty(0,T;\mathbf{L}^2(\Omega))}\lesssim T\,\|\mathbf{F}\|_{L^\infty(0,T;\mathbf{L}^2(\Gamma_N))}$$

Note in particular that the above bound is independent of $\varepsilon>0$ since there is no dependency on the right-hand side of the inequality, from which follows well-possedness for each multiscale elastic problem with parameters $\varepsilon>0$.

□

Now, the idea is to obtain a result of time regularity for the solution of the multiscale elastodynamic model. The motivation comes from *Panasenko* works [17], who obtained such type of results in a general viscoelastic case with full *Dirichlet* boundary conditions.

In this case, a bootstrap type method is used to obtain the time-regularity for the mixed boundary problem, with the bounds derived from spectral theory.

Proposition 2.2 *Let $u^\varepsilon \in \mathcal{C}^0(0,T;\mathbf{H}^1(\Omega,\Gamma_D))$ denote the unique solution of the mixed boundary multiscale problem and suppose also the regularity for the parameters and surface force given by $C_{ijkl} \in L^\infty(\mathbf{Y})$ and $\mathbf{F} \in \mathcal{C}^p(0,T;\mathbf{L}^2(\Gamma_N))$, then for each $p \geq 1$ we have that:*

$$u^\varepsilon, \partial_t u^\varepsilon \in \mathcal{C}^p(0,T;\mathbf{L}^2(\Omega)).$$

Remark In particular, from the proof it's also possible to obtain that

$$u^\varepsilon, \partial_t u^\varepsilon \in \mathcal{C}^p(0,T;\mathbf{H}^1(\Omega,\Gamma_D)).$$

Proof. Let us develop the main idea of the proof:

1. Using the spectral theory for the existence of multiscale problem, it is obtained a solution u^ε having regularity:

   $$u^\varepsilon \in \mathcal{C}^0(0,T;\mathbf{H}^1(\Omega,\Gamma_D)) \cap \mathcal{C}^1(0,T;\mathbf{L}^2(\Omega))$$

   thus the results being valid for initial cases $p = 0, 1$.
2. Let us take $|h| \ll 1$ such that $t + h \in (0,T)$ and define the difference with parameter $\varepsilon > 0$ fixed as:

   $$u_h^\varepsilon(t,\mathbf{x},\frac{\mathbf{x}}{\varepsilon}) := u^\varepsilon(t+h,\mathbf{x},\frac{\mathbf{x}}{\varepsilon}) - u^\varepsilon(t,\mathbf{x},\frac{\mathbf{x}}{\varepsilon})$$

   Now, defining the difference of surface forces as

   $$\mathbf{F}_h(t) := \mathbf{F}(t+h) - \mathbf{F}(t)$$

   it follows that the problem satisfied for functions u_h^ε is given by:

   $$(P_\varepsilon) \begin{cases} \rho^\varepsilon \partial_{tt} u_h^\varepsilon - \nabla \cdot \sigma^\varepsilon(u_h^\varepsilon) = \mathbf{0} & \text{in } (0,T)\times\Omega \\ \sigma_{ij}^\varepsilon(u_h^\varepsilon) = C_{ijkl}^\varepsilon \mathbf{e}_{kl}(u_h^\varepsilon) & \text{in } (0,T)\times\Omega \\ C_{ijkl}^\varepsilon \mathbf{e}_{kl}(u_h^\varepsilon) n_j = \mathbf{F}_h & \text{on } (0,T)\times\Gamma_N \\ u_h^\varepsilon = \mathbf{0} & \text{on } (0,T)\times\Gamma_D \end{cases}$$

   with initial condition at rest (i.e. $\partial_t u_h^\varepsilon = u_h^\varepsilon = \mathbf{0}$ on $\{t=0\}\times\Omega$).
3. Using the assumption of regularity for the surface force $\mathbf{F}$, it can be obtained from spectral theory the bound:

   $$\|u_h^\varepsilon\|_{\mathbf{H}^1(\Omega,\Gamma_D)} + \|\partial_t u_h^\varepsilon\|_{\mathbf{L}^2(\Omega)} \lesssim \int_t^{t+h} \|\mathbf{F}(s)\|_{\mathbf{L}^2(\Gamma_N)}\,\mathrm{d}s$$

   so, from the continuity it is obtained that as $h \to 0$, the terms

   $$\|u_h^\varepsilon\|_{\mathbf{H}^1(\Omega,\Gamma_D)}, \|\partial_t u_h^\varepsilon\|_{\mathbf{L}^2(\Omega)} \to 0$$

   then $u^\varepsilon \in \mathcal{C}^2(0,T;\mathbf{L}^2(\Omega))$.

4. Now, let us observe that we can take a time derivative to the full problem (P_ε), and obtain a similar multiscale problem. Applying again the spectral theory, it is possible to obtain a solution $v_h^\varepsilon = \partial_t u_h^\varepsilon$, satisfying same bounds as before. In such a way, it follows that:

$$\|\partial_{tt} u_h^\varepsilon\|_{\mathbf{H}^1(\Omega,\Gamma_D)} + \|\partial_t u_h^\varepsilon\|_{\mathbf{L}^2(\Omega)} \lesssim \int_t^{t+h} \|\partial_t \mathbf{F}(t)\|_{\mathbf{L}^2(\Gamma_N)}$$

so that, as $h \to 0$ we conclude the regularity

$$\partial_t u_h^\varepsilon \in \mathcal{C}^0(0,T;\mathbf{H}^1(\Omega,\Gamma_D)) \cap \mathcal{C}^1(0,T;\mathbf{L}^2(\Omega))$$

then

$$u_h^\varepsilon \in \mathcal{C}^3(0,T;\mathbf{L}^2(\Omega))$$

and by a bootstrap type argument, the results follows for each $p \geq 1$.

□

2.1 Homogenization Procedure

In this section, it is described the procedure to obtain effective (or macroscopic) equations derived from the multiscale model (2.1), by means of asymptotic approximation of the displacement $u^\varepsilon(\mathbf{x},t)$ proposed by the two-scale homogenization theory inspired from [4]. This framework enables us to obtain an effective PDE model governing the overall macroscopic mechanical behavior that incorporates the highly oscillatory microstructure variation by using the cell problems. It provides moreover an algorithmic procedure suitable for numerical implementation[3].

To give jargon regarding homogenization literature, the variable $\mathbf{x}$ is defined as slow or global coordinate, while $\mathbf{y}$ denote the fast or local variable, related by $\mathbf{y} = \varepsilon^{-1}\mathbf{x}$ as used before. In particular, the ε parameter represent the highly-oscillatory periodicity assumed on the material components described by the cell structure.

2.1.1 Two-Scale Asymptotic Homogenization

It is assumed that displacement solutions to problem (2.1) can be expressed as expansion at different ε scales. Thus, the solution is found by an asymptotic expression at each time $t \in \mathbb{R}_+$ in the form:

$$u^\varepsilon(t,\mathbf{x}) = \sum_{a=0}^{\infty} \varepsilon^a u^{(a)}(t,\mathbf{x},\mathbf{y}) \tag{2.8}$$

where the vector functions $u^{(a)}(\mathbf{x},\cdot)$ are assumed Y-periodic, spanning the full domain Ω for each $a > 0$. Moreover, throughout the developments it is assumed regularity for each

[3]It keeps the mechanical behavior explicitly stated in all the derivation of the homogenized model, thus keeping its physical interpretation in the context of solid mechanics.

$t \in (0, T)$ in the form:

$$u^{(a)}(t, \mathbf{x}, \mathbf{y}) \in \mathbf{H}^1\big(\Omega; \mathbf{H}^1(\mathbf{Y})\big) \quad \forall a \in \mathbb{N}$$

where $\mathbf{H}^1(\mathbf{Y})$ denotes the space of d-dimensional vector function on $H^1(\mathbf{Y})$. In what follows, it will be imposed several restrictions for the proposed solution (2.8) to effectively satisfy the problem (2.1). In particular, the regularity assumption will naturally arise from restriction imposed for each $u^{(a)}$. In all that follows, it is dropped the time dependency in the functions for easiness of exposition.

Since there is an explicit relation between slow and fast variables, it is considered expressions of strain rate dependent on each one. Let us define for $\Phi \in \mathcal{C}^\infty(\Omega \times \mathbf{Y})$ the strain on each variable by:

$$\mathbf{e}_{kl,\alpha}(\Phi(\alpha)) = \frac{1}{2}(\partial_{\alpha_l}\Phi_k(\alpha) + \partial_{x_k}\Phi_l(\alpha)) \quad \forall \alpha \in \{\mathbf{x}, \mathbf{y}\}$$

thus, after applying it over the strain tensor $\mathbf{e}(\cdot)$ it follows the relation at components k, l given in the form:

$$\mathbf{e}_{kl}(u^{(a)}(\mathbf{x}, \frac{\mathbf{x}}{\varepsilon})) = \mathbf{e}_{kl,x}(u^{(a)}(\mathbf{x}, \mathbf{y})) + \varepsilon^{-1}\mathbf{e}_{kl,y}(u^{(a)}(\mathbf{x}, \mathbf{y})). \tag{2.9}$$

In the following, it is used a separation of scales to obtain the so-called homogenized coefficients, approximating the overall macroscopic (effective) behavior by applying the asymptotic solution, i.e., seeking

$$\rho^\varepsilon(\mathbf{x})u(\mathbf{x})^\varepsilon + P^{(\varepsilon)}(u^\varepsilon(\mathbf{x})) = \mathcal{O}(\varepsilon^\gamma) \quad \gamma \geq 0$$

where the elasticity operator $P^{(\varepsilon)}$ is expected to satisfy under some corrections

$$P^{(\varepsilon)}(u^\varepsilon(\mathbf{x}) = -\mathrm{div}\left[\mathbf{C}^{hom}(\mathbf{x}) : \mathbf{e}(u^{(0)}(\mathbf{x}))\right] + \mathcal{O}(\varepsilon) \tag{2.10}$$

where $\mathbf{C}^{hom}(\mathbf{x})$ is some four-order tensor to be found and the right-hand side $\mathcal{O}(\varepsilon^\gamma)$ denotes the error expected from such an approximation.

To handle derivatives from (2.10), let us define the operator

$$L_{\alpha\beta}(\cdot) = -\partial_{\alpha_j}\big(C_{ijkl}(\mathbf{y})\mathbf{e}_{kl,\beta}(\cdot)\big), \quad \alpha, \beta \in \{\mathbf{x}, \mathbf{y}\}$$

And recall that by the chain rule $\forall\, \Phi(\mathbf{x}, \mathbf{y})$ enough regular vector functions, it follows:

$$\partial_{x_j}(\Phi(\mathbf{x}, \frac{\mathbf{x}}{\varepsilon})) = \big\{\partial_{x_j}\Phi(\mathbf{x}, \mathbf{y}) + \frac{1}{\varepsilon}\partial_{y_j}\Phi(\mathbf{x}, \mathbf{y})\big\}_{\mathbf{y}=\varepsilon^{-1}\mathbf{x}}.$$

Now, using (2.8), the idea is to regroup in powers of ε thus impose constrains over each term $\varepsilon^{(a)}$ to satisfy the main formulation (2.1). To this end, note that from (2.10) it follows:

$$P^{(\varepsilon)}(u(\mathbf{x}, \varepsilon)) = A + B + C + \mathcal{O}(\varepsilon)$$

where

$$\begin{aligned} A &= P^{(\varepsilon)}(u^{(0)}(\mathbf{x}, \mathbf{y})) \\ B &= \varepsilon P^{(\varepsilon)}(u^{(1)}(\mathbf{x}, \mathbf{y})) \\ C &= \varepsilon^2 P^{(\varepsilon)}(u^{(2)}(\mathbf{x}, \mathbf{y})) \end{aligned}$$

Expanding every term and using (2.9), it follows:

$$\begin{aligned} A &= -\partial_{x_j}\big(C_{ijkl}\mathbf{e}(u^{(0)})\big) \\ &= -\partial_{x_j}\big(C_{ijkl}\mathbf{e}_{kl,x}(u^{(0)}) + \frac{1}{\varepsilon}C_{ijkl}\mathbf{e}_{kl,y}(u^{(0)})\big) \\ &= -L_{xx}u^{(0)} - \frac{1}{\varepsilon}L_{yx}u^{(0)} - \frac{1}{\varepsilon}L_{xy}u^{(0)} - \frac{1}{\varepsilon^2}L_{yy}u^{(0)} \end{aligned}$$

Similarly, for the other terms it can be obtained:

$$\begin{aligned} B &= -\varepsilon L_{xx}u^{(1)} - L_{yx}u^{(1)} - L_{xy}u^{(1)} - \frac{1}{\varepsilon}L_{yy}u^{(1)} \\ C &= -\varepsilon^2 L_{xx}u^{(2)} - \varepsilon L_{yx}u^{(2)} - \varepsilon L_{xy}u^{(2)} - L_{yy}u^{(2)} \end{aligned}$$

So, the following necessary conditions for powers of ε are derived:

$$\begin{array}{rcll} \varepsilon^{-2} \longrightarrow & L_{yy}u^{(0)} & = \mathbf{0} & \\ \varepsilon^{-1} \longrightarrow & L_{xy}u^{(0)} + L_{yx}u^{(0)} + L_{yy}u^{(1)} & = \mathbf{0} & (2.11) \\ \varepsilon^{0} \longrightarrow & L_{xx}u^{(0)} + L_{xy}u^{(1)} + L_{yx}u^{(1)} + L_{yy}u^{(2)} + \rho^{\varepsilon}u^{(0)} & = \mathbf{0} & \end{array}$$

Let us consider the asymptotic expansion (2.8) as an approximation for the exact solution of the original problem (2.1) where their boundary conditions had been replaced to the behavior at $\mathcal{O}(1)$.

$$\begin{array}{cc} u^{(0)}(\mathbf{x},\mathbf{y}) = \mathbf{0} & \forall(\mathbf{x},\mathbf{y}) \in \Gamma_D \times \mathbf{Y} \\ \big(\mathbf{C}(\mathbf{y}) : \mathbf{e}(u^{(0)}(\mathbf{x},\mathbf{y})\big) \cdot n = \hat{\mathbf{F}}(\mathbf{x}) & \forall(\mathbf{x},\mathbf{y}) \in \Gamma_N \times \mathbf{Y} \end{array}$$

and the remaining terms for each $a \in \mathbb{N}$ in the expansion are assigned by

$$\begin{array}{cc} u^{(a)}(\mathbf{x},\mathbf{y}) = \mathbf{0} & \forall(\mathbf{x},\mathbf{y}) \in \Gamma_D \times \mathbf{Y} \\ \big(\mathbf{C}(\mathbf{y}) : \mathbf{e}(u^{(a)}(\mathbf{x},\mathbf{y})\big) \cdot n = \mathbf{0} & \forall(\mathbf{x},\mathbf{y}) \in \Gamma_N \times \mathbf{Y} \end{array}$$

Let us recall a classical results for elliptic problems. It relates the existence for problems in (2.11) by some compatibility conditions.

Lemma 2.3 *Let $f(\cdot)$ be a square integrable function over $\mathbf{Y}$. Consider the problem:*

$$L_{yy}\Phi(\mathbf{y}) = f(\mathbf{y}) \text{ in } \mathbf{Y}$$

where Φ is $\mathbf{Y}$-periodic function. Then it holds:

1. *There exist a $\mathbf{Y}$-periodic solution Φ iff $\langle f \rangle = \mathbf{0}$*
2. *If a Y-periodic solution Φ exists, then it's unique up to a constant vector $\mathbf{c} \in \mathbb{R}^{\mathrm{d}}$.*

Remark It is being used as notation

$$\langle f \rangle := \frac{1}{|Y|}\int_{\mathbf{Y}} f(\mathbf{y})\,\mathrm{d}\mathbf{y}$$

where $|Y|$ denotes the measure of the set $\mathbf{Y}$.

2.1.2 Contribution at Second Order

For the contribution at order $\mathcal{O}(\varepsilon^{-2})$ recall that problem (2.1) with their boundary conditions states:

$$\begin{cases} L_{yy}u^{(0)}(\mathbf{x},\mathbf{y}) = \mathbf{0} & \text{in } \Omega\times\mathbf{Y} \\ u^{(0)}(\mathbf{x},\mathbf{y}) = \mathbf{0} & \text{in } \Gamma_D\times\mathbf{Y} \\ \big(\mathbf{C}(\mathbf{y}) : \mathbf{e}(u^{(0)}(\mathbf{x},\mathbf{y})\big)\cdot n = \mathbf{F}(t,\mathbf{x}) & \text{in } \Gamma_N\times\mathbf{Y} \end{cases} \tag{2.12}$$

By the Lemma (2.3) it can be deduced that $u(\mathbf{x},\mathbf{y})$ is solution of (2.12) iff it is constant with respect to the $\mathbf{y}$-variable. It implies then:

$$u^{(0)}(t,\mathbf{x},\mathbf{y}) = v(t,\mathbf{x}) \tag{2.13}$$

i.e. being independent with respect to the microstructure (or fast variable) $\mathbf{Y}$. In particular, the contribution of the boundary conditions is associated to such vector function $v(t,\mathbf{x})$, at each time $t\in(0,T)$ in the form:

$$\begin{aligned} v(\mathbf{x}) &= \mathbf{0} && \text{on } \Gamma_D \\ \big(\mathbf{C}(\mathbf{y}) : \mathbf{e}(v(\mathbf{x}))\big)\cdot n &= \mathbf{F}(\mathbf{x}) && \text{on } \Gamma_N\times\mathbf{Y} \end{aligned}$$

2.1.3 Contributions at First Order

For the contribution at order $\mathcal{O}(\varepsilon^{-1})$ recall by (2.13) it follows $u^{(0)}(\mathbf{x},\mathbf{y}) = v(\mathbf{x})$ then it can deduced by definition:

$$L_{xy}v(\mathbf{x}) = \mathbf{0}$$

So, the problem formulation in (2.11) is reduced to

$$L_{yy}u^{(1)}(\mathbf{x},\mathbf{y}) = -L_{yx}v(\mathbf{x}) \quad \text{in } \Omega\times\mathbf{Y} \tag{2.14}$$

Now, using the Lemma (2.3) on (2.14) taking into account (2.13), the Y-periodicity of $\mathbf{C}(\mathbf{y})$ and the diverge theorem, it follows:

$$\big\langle -L_{yx}u^{(0)}(\mathbf{x},\cdot)\big\rangle = \mathbf{0}$$

thus, the existence of solution for problem 2.14 is satisfied.

Now, by separation of variables and the second condition of lemma (2.3), a general solution to the system of equations (2.14) can be given by:

$$u^{(1)}(\mathbf{x},\mathbf{y}) = \mathbf{N}^{rs}(\mathbf{y})\mathbf{e}_{rs,x}(v(\mathbf{x})) \tag{2.15}$$

where $N^{rs}\in\mathbf{H}^1(\mathbf{Y})$ the so-called cell solution.

Then replacing (2.13), (2.15) into (2.14) results on the so-called cell problems. Explicitly, note that replacing the terms described before, it follows:

$$\begin{aligned} & L_{yy}\big(\mathbf{N}^{rs}(\mathbf{y})\mathbf{e}_{rs,x}(v(\mathbf{x}))\big) + L_{yx}(v(\mathbf{x})) = \mathbf{0} \\ \Longrightarrow\ & -\partial_{y_j}\big(C_{ijkl}\mathbf{e}_{kl,y}(\mathbf{N}^{rs}(\mathbf{y}))\mathbf{e}_{rs,x}(v(\mathbf{x})) = \partial_{y_j}\big(C_{ijrs}\mathbf{e}_{rs,x}(v(\mathbf{x}))\big) \\ \Longrightarrow\ & -\partial_{y_j}\big(C_{ijkl}\mathbf{e}_{kl,y}(\mathbf{N}^{rs}(\mathbf{y}))\big) = \partial_{y_j}(C_{ijrs}) \end{aligned}$$

and applying lemma (2.3), it follows that $\mathbf{N}^{rs}$ is Y-periodic where it has been added the boundary conditions taken from (2.14), obtaining:

$$\begin{cases} -\partial_{y_j}\big(C_{\mathrm{i}jkl}\mathbf{e}_{kl,y}(\mathbf{N}^{rs}(t,\mathbf{y}))\big) = \partial_{y_j}(C_{\mathrm{i}jrs}) & \text{in } (0,T)\times\mathbf{Y} \\ \big(\mathbf{C}(\mathbf{y}) : \mathbf{e}(\mathbf{N}^{rs}(t,\mathbf{y}))\big)\cdot n = \mathbf{0} & \text{on } (0,T)\times\partial\mathbf{Y} \\ \mathbf{N}^{rs}(0,\mathbf{y}) = \mathbf{0} & \text{in } \mathbf{Y} \end{cases}$$

the above deduced by construction using the ansatz (2.15) define a solution to the PDE system (2.14).

2.1.4 Contribution at the zero order

For the contribution at order $\mathcal{O}(\varepsilon^0)$ problem (2.1) after regrouping the terms it follows:

$$L_{yy}u^{(2)} = \rho^{\varepsilon}(\mathbf{x})\partial_{tt}v(\mathbf{x}) - \tilde{P}(u^{(1)},u^{(2)})(\mathbf{x},\mathbf{y}) \quad \text{in } \Omega\times\mathbf{Y} \tag{2.16}$$

where it has been denoted

$$\tilde{P}(u^{(0)},u^{(1)})(\mathbf{x},\mathbf{y}) := L_{xx}u^{(0)} + L_{xy}u^{(1)} + L_{yx}u^{(1)}$$

then by Lemma 2.3, it follows existence of a Y-periodic solution of (2.16) iff

$$\big\langle \rho(\mathbf{y})\partial_{tt}v(\mathbf{x}) - L_{xx}u^{(1)}(\mathbf{x},\mathbf{y}) - L_{xy}u^{(1)}(\mathbf{x},\mathbf{y}) - L_{yx}u^{(1)}(\mathbf{x},\mathbf{y})\big\rangle = \mathbf{0} \tag{2.17}$$

From 2.17 the homogenized equation is obtained, which can be deduced explicitly in the form:

$$\begin{aligned} & \langle\rho(\mathbf{y})\rangle\partial_{tt}v(\mathbf{x}) + \langle L_{xx}u^{(0)}(\mathbf{x},\mathbf{y}) + L_{xy}u^{(1)}(\mathbf{x},\mathbf{y})\rangle = \mathbf{0} \\ \Leftrightarrow\quad & \langle\rho(\mathbf{y})\rangle\partial_{tt}v(\mathbf{x}) + \langle L_{xx}u^{(0)}(\mathbf{x},\mathbf{y}) + L_{xy}\big(\mathbf{N}^{rs}(\mathbf{y})\mathbf{e}_{rs,x}(v(\mathbf{x}))\big) = \mathbf{0} \\ \Leftrightarrow\quad & \langle\rho\rangle\partial_{tt}v_{\mathrm{i}}(\mathbf{x}) - \partial_{x_j}\big\langle\big(C^{hom}_{\mathrm{i}jrs}(\mathbf{N}^{rs})\big)\mathbf{e}_{rs,x}(\hat{v}(\mathbf{x}))\big\rangle = \mathbf{0} \quad \forall\mathrm{i}\in\{1,\dots,\mathrm{d}\} \\ \Leftrightarrow\quad & \rho^0\partial_{tt}v_{\mathrm{i}}(\mathbf{x}) - C^{hom}_{ijkl}\partial_{x_j}\mathbf{e}_{rs,x}(v(\mathbf{x})) = \mathbf{0} \quad \forall\mathrm{i}\in\{1,\dots,\mathrm{d}\} \end{aligned}$$

where it is denoted $\rho^0 = \langle\rho\rangle$ and $C^{hom}_{\mathrm{i}jrs}$ the so-called homogenized elastic coefficients defined by

$$C^{hom}_{\mathrm{i}jrs} = \big\langle C_{\mathrm{i}jrs}(\mathbf{y}) + C_{\mathrm{i}jkl}\mathbf{e}_{kl,y}\big(\mathbf{N}^{rs}(\mathbf{y})\big)\big\rangle$$

With the above definition and the homogenized equation obtained from (2.16) it can be obtained the effective behavior of the system defined by:

$$\begin{cases} \rho^0\partial_{tt}v - \nabla\cdot\sigma^0(v) = \mathbf{0} & \text{in } (0,T)\times\Omega \\ \sigma^0_{\mathrm{i}j}(v) = C^{hom}_{\mathrm{i}jkl}\mathbf{e}_{kl,x}(v) & \text{in } (0,T)\times\Omega \\ v = \mathbf{0} & \text{on } (0,T)\times\Gamma_D \\ \sigma^0(v)\cdot n = \mathbf{F} & \text{on } (0,T)\times\Gamma_N \end{cases} \tag{2.18}$$

In particular, the PDE problem (2.18) is well-posed and the mechanical behavior maintains the linear elasticity property from the material.

Finally, it will be useful in the next chapters to recall that the homogenized elastic operator defines a bilinear form on $\mathbf{H}^1(\Omega, \Gamma_D)$ by:

$$a(u,v) := \int_\Omega \sigma_{ij}^{hom}(u(\mathbf{x})\partial_{x_j} v_i \, \mathrm{d}x \quad u, v \in \mathbf{H}^1(\Omega, \Gamma_D)$$

moreover, since the homogenized coefficients are bounded and uniformly elliptic it can be applied the classical theorem of spectral decomposition [19].

Proposition 2.4 *Let $V \subset H$ Hilbert spaces, such that V is dense and continuously embedded in H. Suppose the canonical injection from V on H is compact, and the bilineal form $a(\cdot,\cdot)$ is symmetric, V-elliptic. Then there exist an increasing sequence which tend to $+\infty$ of eigenvalues*

$$0 < \lambda_1 < \lambda_2 \leq \cdots \leq \lambda_m \leq \cdots$$

and a hilbertian orthonormal base of H given by eigenvector w_m such that:

$$\forall v \in V, \quad a(w_,, v) = \lambda_m (w_m, v), \quad \forall m = 1, 2, \ldots$$

2.2 Justification of the homogenization

Having obtained the homogenized model, in this section it is developed the justification procedure of convergence for the solution in the space $\mathbf{H}^1(\Omega, \Gamma_D)$. It corresponds to an extension of the work done by [16] in the static case. To handle easily the derivatives, it will be reformulated the problem (2.1) to a canonical form described below[4].

Over the bounded smooth domain $\Omega \subset \mathbb{R}^{\mathrm{d}}$ it is considered the multiscale problem of second order in time:

$$\begin{cases} \mathcal{L}_\varepsilon(u^\varepsilon) := \rho\left(\frac{\mathbf{x}}{\varepsilon}\right)\partial_{tt} u^\varepsilon - \partial_{x_h}\left(A^{hk}\left(\frac{\mathbf{x}}{\varepsilon}\right)\partial_{x_k} u^\varepsilon\right) = \mathbf{0} & \text{in } (0,T)\times\Omega \\ \sigma^\varepsilon(u^\varepsilon)\cdot n := A^{hk}\left(\frac{\mathbf{x}}{\varepsilon}\right)\partial_{x_k} u^\varepsilon n_k = \mathbf{F}(t,\mathbf{x}) & \text{on } (0,T)\times\Gamma_N \\ u^\varepsilon = \mathbf{0} & \text{on } (0,T)\times\Gamma_D \\ \partial_t u^\varepsilon = u^\varepsilon = \mathbf{0} & \text{on } \{t=0\}\times\Omega \end{cases} \tag{2.19}$$

being n the unit outward normal to $\partial\Omega$, the disjoint decomposition $\partial\Omega = \Gamma_D \dot{\cup} \Gamma_N$ and assumed enough regularity for the boundaries (at least *Lipschitz*). It is also assumed that the coefficients matrices $A^{hk}(\mathbf{y})$ are smooth functions, 1-periodic that satisfy conditions of uniformly ellipticity and boundness in $\mathbf{y}$.
Recall also from (2.18) the homogenized mixed boundary problem, rewritten in canonical form is given by:

$$\begin{cases} \mathcal{L}_0(u^0) := \rho^0\partial_{tt} u^0 - \partial_{x_h}\left(A^{hk}_{hom}\partial_{x_k} u^0\right) = \mathbf{0} & \text{in } (0,T)\times\Omega \\ \sigma^0(u^0)\cdot n := A^{hk}_{hom}\partial_{x_k} u^0 n_h = \mathbf{F}(t,\mathbf{x}) & \text{on } (0,T)\times\Gamma_N \\ u^0 = \mathbf{0} & \text{on } (0,T)\times\Gamma_D \\ \partial_t u^0 = u^0 = \mathbf{0} & \text{on } \{t=0\}\times\Omega \end{cases} \tag{2.20}$$

[4]The choice of a canonical formulation for the mixed boundary elastodynamic model is based on straightforward usage of space derivatives and estimations to assure the justification of the asymptotic solution, in the sense that the two-scale approximate solution $u^\varepsilon(t,\mathbf{x})$ converge to the real (experimental solution) $u(t,\mathbf{x})$ in some space with enough regularity.

where the matrices A^{hk}_{hom} (denoting the homogenized material coefficients) are defined by the formulas:

$$A^{pq}_{hom} = \int_{\mathbf{Y}} A^{pq}(\mathbf{y}) + A^{pj}(\mathbf{y})\partial_{y_j}\mathbf{N}^q(\mathbf{y})\,\mathrm{d}\mathbf{y} \tag{2.21}$$

being the matrices $\mathbf{N}^q(\mathbf{y})$ the so-called cell solutions of the following boundary value problem:

$$\begin{cases} \partial_{y_k}\big(A^{kj}(\mathbf{y})\partial_{y_j}\mathbf{N}^q\big) = -\partial_{y_k}\big(A^{kq}(\mathbf{y})\big) & \text{in } \mathbf{Y} \\ \mathbf{N}^q(\mathbf{y}) \quad \text{1-periodic in } \mathbf{y}, & \int_{\mathbf{Y}} \mathbf{N}^q(\mathbf{y})\,\mathrm{d}\mathbf{y} = \mathbf{0} \end{cases} \tag{2.22}$$

where $\mathbf{Y} = (0,1)^{\mathrm{d}}$ is the characteristic microstructure and $\mathrm{d} \in \mathbb{N}^*$ denotes the dimension, usually 2 or 3.

Remark Let us note from (2.22) that by applying coercivity and boundness conditions over the coefficients $A^{kj}(\mathbf{y})$, it follows continuity and boundness conditions on (2.21). Thus the homogenized problem (2.20) is of elastic type, and moreover it can be applied the same proof as in the case of prop. 2.2 obtaining by bootstrapping method:

$$u^0,\, \partial_t u^0 \in \mathcal{C}^p(0,T;\mathbf{H}^1(\Omega,\Gamma_D))$$

It is assumed an approximate solution to the problem (2.19) in the form:

$$\tilde{u}(t,\mathbf{x}) = u^0(t,\mathbf{x}) + \varepsilon\mathbf{N}^s\big(\frac{\mathbf{x}}{\varepsilon}\big)\partial_{x_s}u^0(t,x) \tag{2.23}$$

where u^0 is the solution to problem (2.20) and $\mathbf{N}^s(\mathbf{y})$ solutions to the so-called cell problems (2.22).

Now, let us enunciate the main result, where the sketch of proof will be presented in the next section.

Theorem 2.5 *Assuming that* $\mathbf{F} \in L^\infty(0,T;\mathbf{L}^2(\Gamma_N))$ *and also* $\mathbf{N}^q \in L^\infty(0,T;\mathbf{H}^1(\Omega))$ *for each* $q \in \{1,\ldots,N\}$. *Then the solutions* u^ε *and* u^0 *of problems (2.19) and (2.20) respectively, satisfy the following inequality*

$$\|u^\varepsilon - u^0 - \varepsilon\mathbf{N}^s\big(\frac{\mathbf{x}}{\varepsilon}\big)\partial_{x_s}u^0\|_{L^\infty(0,T;\mathbf{H}^1(\Omega,\Gamma_D))} \lesssim \varepsilon^{1/2}\|u^0\|_{L^\infty(0,T;\mathbf{H}^3(\Omega))}$$

2.3 Sketch of the Proof

The result is constructed using the work done on [16], extending it from the elastostatic case to the elastodynamic model with mixed boundary conditions by controlling the behavior of each time-dependent that appears in the deduction. In this sense, the proof corresponds to an extension of the work done by *Oleinik*.

The idea will be to study at fixed time $t \in (0,T)$ the elastodynamic operator $\mathcal{L}_\varepsilon$. Let us apply the operator $\mathcal{L}_\varepsilon$ to a vector valued function $u^\varepsilon - \tilde{u}$, where $\tilde{u}$ is defined by (2.23), then:

$$\begin{aligned}\mathcal{L}_\varepsilon(u^\varepsilon - \tilde{u}) =& \rho^\varepsilon \partial_{tt}(u^\varepsilon - \tilde{u}) - \partial_{x_h}\big(A^{hk}\partial_{x_k}u^\varepsilon\big) + \partial_{x_h}\big(A^{hk}\partial_{x_k}(u^0 + \varepsilon \mathbf{N}^s \partial_{x_s}u^0)\big)\\ \overset{(*)}{=}& -(\rho^\varepsilon - \rho^0)\partial_{tt}u^0 - \varepsilon\rho^\varepsilon\partial_{tt}\big(\mathbf{N}^s\partial_{x_s}u^0\big)\\ & - \partial_{x_h}\big[\big(A^{hk}_{hom} - A^{hk} - \varepsilon A^{hj}\partial_{x_j}\mathbf{N}^k\big)\partial_{x_k}u^0\big] + \varepsilon\partial_{x_h}\big(A^{hk}\mathbf{N}^s\partial_{x_kx_s}u^0\big)\end{aligned}$$

where in $(*)$ it was rewritten, relabeled and separated term with ε order. Taking into account the equation in (2.22) for the $\mathbf{N}^s$ it follows:

$$\begin{aligned}\mathcal{L}_\varepsilon(u^\varepsilon - \tilde{u}) :=& -(\rho^\varepsilon - \rho^0)\partial_{tt}u^0 - \varepsilon\rho^\varepsilon\partial_{tt}\big(\mathbf{N}^s\partial_{x_s}u^0\big) + \varepsilon A^{hk}\mathbf{N}^s\partial_{x_hx_kx_s}u^0\\ & - \big[A^{pq}_{hom} - A^{pq} - A^{pj}\partial_{y_j}\mathbf{N}^q - \partial_{y_h}(A^{hp}\mathbf{N}^q)\big]\partial_{x_px_q}u^0\end{aligned}$$

From the above expression, let us define the matrices $\mathbf{N}^{hk}(\mathbf{y})$ as weak solutions of the following boundary value problem

$$\begin{cases} \partial_{y_k}\big(A^{kj}\partial_{y_j}\mathbf{N}^{pq}\big) = -\partial_{y_k}\big(A^{kp}\mathbf{N}^q\big) - A^{pj}\partial_{y_j}\mathbf{N}^q - A^{pq} + A^{pq}_{hom} & \text{in } \mathbf{Y}\\ \sigma(N^{pq})\cdot n := A^{kl}\partial_{x_k}\mathbf{N}^{pq}n_l = -n_kA^{pk}\mathbf{N}^q & \text{on } \partial\mathbf{Y}\\ \mathbf{N}^{hk}(\mathbf{y})\ \mathbf{Y}\text{-periodic}, \quad \int_{\mathbf{Y}} N^{pq}\mathrm{d}\mathbf{y} = \mathbf{0} \end{cases} \tag{2.24}$$

So, using (2.24) it can be obtained:

$$\begin{aligned}\mathcal{L}_\varepsilon(u^\varepsilon - \tilde{u}) =& -(\rho^\varepsilon - \rho^0)\partial_{tt}u^0 - \varepsilon\rho^\varepsilon\partial_{tt}\big(\mathbf{N}^s\partial_{x_s}u^0\big)\\ & + \varepsilon A^{hk}\mathbf{N}^s\partial_{x_hx_kx_s}u^0 + \varepsilon A^{kj}\partial_{y_j}\mathbf{N}^{pq}\partial_{x_px_qx_k}u^0\\ & - \varepsilon\partial_{x_k}\big[A^{kj}\partial_{y_j}\mathbf{N}^{pq}\partial_{x_px_q}u^0\big]\end{aligned}$$

Thus, it follows:

$$\mathcal{L}_\varepsilon(u^\varepsilon - \tilde{u}) = G^0_{tt} + \varepsilon G^1_{tt} + \varepsilon F_0 + \varepsilon\partial_{x_k}F_k \tag{2.25}$$

where each term is defined by:

$$\begin{aligned} G^0_{tt} =& -(\rho^\varepsilon - \rho^0)\partial_{tt}u^0\\ G^1_{tt} =& -\rho^\varepsilon\partial_{tt}(\mathbf{N}^s\partial_{x_s}u^0)\\ F_0 =& A^{hk}N^s\partial_{x_hx_kx_s}u^0 + A^{kj}\partial_{y_j}\mathbf{N}^{pq}\partial_{x_px_qx_k}u^0\\ F_k =& -A^{kj}\partial_{y_j}\mathbf{N}^{pq}\partial_{x_px_q}u^0\end{aligned} \tag{2.26}$$

Remark Let us recall the two-scale asymptotic solution proof, by the hypothesis of continuity for the $\mathcal{O}(1)$ term in the form:

$$v \in \mathcal{C}^2(0,T;\mathbf{H}^1(\Omega,\Gamma_D))$$

It follows that terms G^0_{tt}, G^1_{tt} are bounded.

Let us now obtain a expression for the *Neumann* condition at Γ_N. To this end, applying σ_ε to the difference $u^\varepsilon - \tilde{u}$ it follows that:

$$\begin{aligned}\sigma_\varepsilon(u^\varepsilon - \tilde{u}) &= \sigma_\varepsilon(u^\varepsilon) - \sigma_\varepsilon(\tilde{u}) \\ &= F_h(t)n_h - A^{hk}\partial_{x_k}\big(u^0 + \varepsilon N^s \partial_{x_s} u^0\big)n_h \\ &= \big(A^{hk}_{hom} - A^{hk}\big)\partial_{x_k}u^0 n_h - A^{hl}\partial_{y_l}N^s\partial_{x_s}u^0 n_h - \varepsilon A^{hk}N^s\partial_{x_k x_s}u^0 n_h\end{aligned}$$

Taking into account the obtained expression, let us define:

$$\alpha^{\mathrm{i}s}(\mathbf{y}) := A^{\mathrm{i}s}_{hom} - A^{\mathrm{i}s}(\mathbf{y}) - A^{\mathrm{i}j}(\mathbf{y})\partial_{y_j}\mathbf{N}^s(\mathbf{y}), \quad \mathrm{i}, s \in \{1, \dots, \mathrm{d}\}$$

That allows us to obtain the expression at the *Neumann* boundary in the form:

$$\begin{aligned}\sigma_\varepsilon(u^\varepsilon - \tilde{u}) &= \alpha^{hs}\partial_{x_s}u^0 n_h - \varepsilon A^{hk}N^s\partial_{x_k x_s}u^0 n_h \\ &= I_0 + \varepsilon I_1\end{aligned} \tag{2.27}$$

where $I_0 = \alpha^{hs}\partial_{x_s}u^0 n_h$ and $I_1 = -A^{hk}N^s\partial_{x_k x_s}u^0 n_h$. The function α^{hs} has already been studied in the similar context by *Oleinik* [16], who shown a continuity property: For each $v \in \mathbf{H}^1(\Omega)$

$$\left|\int_{\partial\Omega}\alpha^{\mathrm{i}k}(\frac{\mathbf{x}}{\varepsilon})v_k n_{\mathrm{i}}\,\mathrm{d}s\right| \lesssim \varepsilon^{1/2}\|\nabla v\|_{\mathbf{L}^2(\Omega)} \tag{2.28}$$

which applies to our case of functions $v \in \mathbf{H}^1(\Omega, \Gamma_D)$, whereas the I_2 term can be shown to satisfy similarly the bound:

$$\left|\int_{\partial\Omega} I_2\right| \lesssim \varepsilon^{1/2}\|\nabla u_0\|_{\mathbf{L}^2(\Omega)} \tag{2.29}$$

The intuition behind (2.29) relies in using that $\partial\Omega \subset \partial B_\varepsilon(\Omega)$ where $B_\varepsilon(\Omega) = \{\mathbf{x} \in \Omega \,|\, \rho(\mathbf{x}, \Omega) \leq \varepsilon\}$ from which the $\varepsilon^{1/2}$ bound follows by applying *Lemma 2.2* from [16] with the uniform bound on $\mathbf{Y}$ of A^{hk} and N^s.

On the other hand, at the boundary Γ_D for the difference $u^\varepsilon - \tilde{u}$ it follows:

$$u^\varepsilon - \tilde{u} = -\varepsilon N^s \partial_{x_s}u^0 \equiv \psi_\varepsilon$$

Such kind of function satisfies moreover

$$\|\psi_\varepsilon\|_{\mathbf{H}^{1/2}(\Gamma_D)} \lesssim \varepsilon^{1/2}\|u^0\|_{\mathbf{H}^2(\Omega)} \tag{2.30}$$

To prove (2.30), it suffices to find a function $\Psi_\varepsilon \in H^1(\Omega)$ such that $\Psi_\varepsilon|_{\Gamma_D} = \psi_\varepsilon \in \mathbf{H}^{1/2}(\Gamma_D)$ with $\|\Psi_\varepsilon\|_{\mathbf{H}^1(\Omega)} \lesssim \varepsilon^{1/2}\|u^0\|_{\mathbf{H}^2(\Omega)}$.

Let us define such $\Psi_\varepsilon(\mathbf{x})$ using a cutoff function. To this end, let $\varphi_\varepsilon \in \mathcal{C}^\infty(\Omega)$ be such that:

$$\begin{cases}\varphi_\varepsilon(\mathbf{x}) = 1 \text{ if } \rho(\mathbf{x}, \Gamma_D) \leq \varepsilon \\ \varphi_\varepsilon(\mathbf{x}) = 0 \text{ if } \rho(\mathbf{x}, \Gamma_D) \geq 2\varepsilon\end{cases}$$

with $0 \leq \varphi_\varepsilon(\mathbf{x}) \leq 1$ and $|\nabla\varphi_\varepsilon| \lesssim \varepsilon^{-1}$. Then, by construction it follows that $\Psi_\varepsilon := \varepsilon\varphi_\varepsilon N^s\partial_{x_s}u^0 \in \mathbf{H}^1(\Omega)$. Thus, from φ_ε and the uniformly boundness in ε of $N^s, \partial_{y_j}N^s$ for each $s, j \in \{1, \dots, \mathrm{d}\}$ it follows:

$$\|\Psi_\varepsilon\|_{H^1(\Omega)} \leq \|u^0\|_{H^1(B_\varepsilon(\Gamma_D))} + \varepsilon\|u^0\|_{\mathbf{H}^2(\Omega)}$$

being $B_\varepsilon(\Gamma_D) = \{\mathbf{x} \in \Omega : \rho(\mathbf{x}, \Gamma_D) \leq 2\varepsilon\}$. From which it can be deduced the desired result after applying the result (Lemma 1.5 at [16]).

From the developments done, a mixed boundary evolution problem for the variable $u^\varepsilon - \tilde{u}$ is obtained given by:

$$\begin{cases} \mathcal{L}_\varepsilon(u^\varepsilon - \tilde{u}) = G^0_{tt} + \varepsilon G_t t^1 + \varepsilon \partial_{x_k} F_k + \varepsilon F_0 \text{ in } (0,T)\times\Omega \\ \qquad\qquad u^\varepsilon - \tilde{u} = \psi_\varepsilon \text{ on } (0,T)\times\Gamma_D \\ \qquad\qquad \sigma_\varepsilon(u^\varepsilon - \tilde{u}) = I_0 + \varepsilon I_1 \text{ on } (0,T)\times\Gamma_N \end{cases} \tag{2.31}$$

where each term $G^0_{tt}, G^1_{tt}, F^0_k$ are uniformly bounded in ε and time, I_0, I_1 bounded in (2.28), (2.29) respectively and ψ_ε bounded in (2.30). Moreover, the operator $\mathcal{L}_\varepsilon(\cdot)$ is of linear elastic type. It follows that (2.31) defines a well-posed evolution problem, which can be solved as in the case of the previous multiscale problems by using the spectral decomposition method [19]. Thus, the existence of solution is guaranteed and the continuity condition with respect to the initial data implies in particular the bound

$$\|u^\varepsilon - u^0 - \varepsilon N^s \partial_{x_s} u^0\|_{L^\infty(0,T;\mathbf{H}^1(\Omega))} \lesssim \varepsilon^{1/2} \|u^0\|_{L^\infty(0,T;\mathbf{H}^3(\Omega)}$$

Remark Let us note from the above bound that for each $t \in (0,T)$ it can be deduced:

$$\|u^\varepsilon - u^0 - \varepsilon \varphi \mathbf{N}^s\big(\frac{\mathbf{x}}{\varepsilon}\big)\partial_{x_s} u^0\|_{\mathbf{H}^1(\Omega,\Gamma_N)} \lesssim \varepsilon^{1/2} \|\mathbf{F}\|_{L^\infty(0,T;\mathbf{L}^2(\Gamma_N))} \tag{2.32}$$

2.4 Energy Estimations

The convergence results shown before contains information of the elastic operator behavior as ε varies, thus the convergence of its energy operator. The results is inspired from the energy result of *Oleinik* [16], extending it to a time-dependent model.

Let us define the energy operators E_ε and E_0 associated to the multiscale and homogenized problems defined in the form:

$$E_\varepsilon(u^\varepsilon) := \int_0^T \int_\Omega \frac{1}{2} u^\varepsilon_{\mathrm{i}} u^\varepsilon_{\mathrm{i}} + \int_0^T \int_\Omega \big(\partial_{x_j} u^\varepsilon, A^{jk}\big(\frac{\mathbf{x}}{\varepsilon}\big)\partial_{x_k} u^\varepsilon\big)$$

and analogously:

$$E_0(u^0) := \int_0^T \int_\Omega \frac{1}{2} u^0_{\mathrm{i}} u^0_{\mathrm{i}} + \int_0^T \int_\Omega \big(\partial_{x_j} u^0, A^{jk}_{hom} \partial_{x_k} u^0\big)$$

Thus, the following can be obtained

Lemma 2.6 *Assuming the hypothesis of the above theorem, we have the convergence of the energy operators, i.e.,*

$$|E_\varepsilon(u^\varepsilon) - E_0(u^0)| \lesssim \varepsilon^{1/2} \|\mathbf{F}\|_{L^\infty(0,T;\mathbf{L}^2(\Gamma_N))}$$

PROOF. Let us fix $t \in (0,T)$, it follows from the result (2.32) the bounds for u^ε and $\partial_{x_\mathrm{i}} u^\varepsilon$ in the form:

$$u^\varepsilon = u^0 + \varepsilon \mathbf{N}^s\big(\frac{\mathbf{x}}{\varepsilon}\big)\partial_{x_s} u^0 + r^\varepsilon(\mathbf{x},t)$$

where the remaining term is bounded for

$$\|r^\varepsilon(\cdot,t)\|_{\mathbf{H}^1(\Omega;\Gamma_D)} \lesssim \varepsilon^{1/2}\|\mathbf{F}\|_{L^\infty(0,T;\mathbf{L}^2(\Gamma_N))}$$

and for each $\mathrm{i} \in \{1,2,3\}$:

$$\partial_{x_\mathrm{i}} u^\varepsilon = \partial_{x_\mathrm{i}} u^0 + \varepsilon \partial_{y_\mathrm{i}} \mathbf{N}^s\big(\frac{\mathbf{x}}{\varepsilon}\big)\partial_{x_s} u^0 + q^\varepsilon_\mathrm{i}(\mathbf{x},t)$$

where now, the remaining term satisfies

$$\|q^\varepsilon_\mathrm{i}(\cdot,t)\|_{\mathbf{H}^1(\Omega,\Gamma_D)} \lesssim \varepsilon^{1/2}\|\mathbf{F}\|_{L^\infty(0,T;\mathbf{L}^2(\Gamma_N))}$$

So, using the definition of the energy operator it follows that:

$$\begin{aligned} E_\varepsilon(u^\varepsilon) = &\int_0^T\int_\Omega \frac{1}{2}(u^0 + \varepsilon \mathbf{N}^s\big(\frac{\mathbf{x}}{\varepsilon}\big)\partial_{x_s} u^0, u^0 + \varepsilon \mathbf{N}^s\big(\frac{\mathbf{x}}{\varepsilon}\big)\partial_{x_s}(u^0)\big) + R(r^\varepsilon) \\ &+ \int_0^T\int_\Omega \big(\partial_{x_j} u^0 + \varepsilon \partial_{x_j}\mathbf{N}^s\big(\frac{\mathbf{x}}{\varepsilon}\big)\partial_{x_s} u^0, A^{jk}\big(\frac{\mathbf{x}}{\varepsilon}\big)\big[\partial_{x_k} u^0 + \varepsilon\partial_{x_k}\mathbf{N}^s\big(\frac{\mathbf{x}}{\varepsilon}\big)\partial_{x_s} u^0\big]\big) + Q(q^\varepsilon) \end{aligned}$$

where the remaining integral terms can be bounded by

$$|R(r^\varepsilon)| \lesssim \varepsilon^{1/2}\|\mathbf{F}\|_{L^\infty(0,T;\mathbf{L}^2(\Gamma_N))}$$

and moreover

$$|Q(q^\varepsilon| \lesssim \varepsilon^{1/2}\|\mathbf{F}\|_{L^\infty(0,T;\mathbf{L}^2(\Gamma_N))}$$

since the functions $u^0, \partial_{x_k} u^0, \mathbf{N}^s, \partial_{x_k}\mathbf{N}^s$ are bounded.

Let us consider a base for the $\mathrm{d}\times\mathrm{d}$ matrices $(m_{\mathrm{i}j})_{\mathrm{i}j}$, using the notation $m_s = (m_{s1},\dots,m_{s\mathrm{d}})$. Thus, consider for each $s,t \in \{1,2,3\}$ the matrices

$$H^{st}(\mathbf{y}) = \partial_{y_\mathrm{i}}\big(\mathbf{N}^s + y_s m_s\big)A^{\mathrm{i}j}(\mathbf{y})\partial_{y_j}\big(\mathbf{N}^t + y_t m_t\big) - A^{st}_{hom}$$

It follows then by the homogenized coefficient definition that $\langle H^{st}\rangle_{\mathbf{Y}} = \mathbf{0}$. Using the definition of H^{st} over the multiscale energy expression, it can be deduced that

$$E_\varepsilon(u^\varepsilon) - E_0(u^0) = \int_0^T\int_\Omega \frac{1}{2}(u^0,u^0) + \partial_{x_s} u^0 H^{st}(\frac{\mathbf{x}}{\varepsilon})\partial_t u^0 + \tilde{R}(r^\varepsilon) + Q(q^\varepsilon)$$

being $|\tilde{R}(r^\varepsilon)| \lesssim \varepsilon^{1/2}\|\mathbf{F}\|_{L^\infty(0,T;\mathbf{L}^2(\Gamma_N))}$, obtained using the same technique as in *Theorem 1.3* [16]. □

2.5 Continuity on the Porosity

The definition of homogenized coefficients contains an explicit dependency on the porosity level since it defines the characteristic microstructure. In this section, it will be studied the continuity of the homogenized coefficients with respect to the porosity level addressing the well-posedness of the inverse problem formulation. Moreover, differentiability is also assessed[5] by means of the cell problem definition.

More explicitly, it is given estimations for such effective coefficients with a continuity property under reasonable hypothesis on the porosity[6]. To this end, let us recall that our formulation for the elasticity coefficients at a cell point $\mathbf{y} \in \mathbf{Y}$ is given by:

$$C_{ijkl}(\mathbf{y}, p) = C^m_{ijkl}\mathbb{I}_{\mathbf{y}\in\mathbf{Y}_m(p)} + C^f_{ijkl}\mathbb{I}_{\mathbf{y}\in\mathbf{Y}_f(p)}$$

being $\mathbf{Y}_m(p)$ and $\mathbf{Y}_f(p)$ the matrix and fluid-like parts of the cell, where the explicit dependency on the porosity fraction $p \in (0,1)$ implies *a posteriori* also the dependence of p on the homogenized coefficient.

2.5.1 Definition and Estimates

In this section is defined the space in which the highly oscillatory coefficients $C_{ijkl}(\cdot)$ belongs dependent on the porosity parameter.

Definition 2.7 *Let us define the set of operators on the feasible porosity interval* $(0,1)$*, associated to a cell-domain* $\mathbf{Y}$ *by:*

$$\mathbf{T}((0,1)\times\mathbf{Y}) := \left\{\mathbf{C}(\cdot,\cdot) \in L^\infty((0,1);\, lin(\boldsymbol{Sym}^{\mathrm{d}})) \,:\, \mathbf{C}(p,\mathbf{y})^* = \mathbf{C}(p,\mathbf{y})\,\forall \mathbf{y}\in\mathbf{Y}\right\} \tag{2.33}$$

where it is used the notation of $lin(\mathbf{Sym}^{\mathrm{d}})$ *as the space of linear, continuous operators from the* $\mathrm{d}\times\mathrm{d}$ *symmetric matrices space with* $\mathbf{L}^2(\mathbf{Y})$ *entries into itself, being* $\mathrm{d} = 2,3$ *and* $*$ *denoting the adjoint.*

Remark Note that, the linear elastic second-order tensors $\mathbf{C} = (C_{ijkl})_{ijkl}$ belong to $\mathbf{T}((0,1)\times\mathbf{Y})$. In particular, the symmetry of the tensors expressed in *Voigt* engineering notation described as $C_{IJ} = C_{JI}$ is given by the self-adjoint property, by identifying the set $lin(\mathbf{Sym}^{\mathrm{d}})$ with the space of arrays indexed in the form $\mathbf{C}(p,\cdot) = (C_{ijkl}(p,\cdot))_{ijkl}$. Over such considerations, the set (2.33) becomes:

$$\mathbf{T}((0,1)\times\mathbf{Y}) = \left\{C_{ijkl}(\cdot,\mathbf{y}) \in L^\infty((0,1);\mathbb{R}) \,:\, C_{ijkl}(\mathbf{y}) = C_{ijlk}(\mathbf{y}) = C_{klij}(\mathbf{y}) \in L^2(\mathbf{Y})\right\}$$

where it is assumed implicitly the dependency on p of each coefficient.

[5] A similar study has been done for the multiscale *Calderón* problem by with high-oscillation conductivity coefficients, oriented to the inverse problem identification of homogenized coefficients *A. Abudlle and A. di Blasio* [3]

[6] Such reasonable hypothesis are oriented in a continuity condition on the definition of the multiscale coefficients $C_{ijkl}(\mathbf{y}, p)$, for example of *Lipschitz* type on p.

With the above it can be defined the space of bounded and coercive tensors associated to parameters $(\alpha, \beta) \in \mathbb{R}^2_+$ given as a subset of $\mathbf{T}((0,1) \times \mathbf{Y})$ with conditions specified below. Let $(C_{ijkl})_{ijkl} \in \mathbf{T}((0,1) \times \mathbf{Y})$, consider α, β two positive parameters and define the following properties:

(H1) If $\xi \in \mathbf{R}^{d\times d} \setminus \{\mathbf{0}_{d\times d}\}$ then $\alpha\xi_{ij}\,\xi_{ij} \leq C_{ijkl}(p,\mathbf{y})\xi_{kl}\,\xi_{ij}$ a.e.$\mathbf{y} \in \mathbf{Y}$ for each $p \in (0,1)$.

(H2) If $\xi \in \mathbf{R}^{d\times d} \setminus \{\mathbf{0}_{d\times d}\}$ then $C_{ijkl}(p,\mathbf{y})\xi_{kl}\xi_{ij} \leq \beta\xi_{ij}\xi_{ij}$ a.e. $\mathbf{y} \in \mathbf{Y}$ for each $p \in (0,1)$.

The above enables to consider the suitable space of linear elastic tensors, related to the generalized *Hookes* law.

Definition 2.8 *A tensor* $\mathbf{C} = (C_{ijkl})_{ijkl} \in \mathcal{T}(\alpha, \beta, (0,1) \times \mathbf{Y})$ *if* $\mathbf{C}$ *is a feasible tensor, i.e., belongs to* $\mathbf{T}((0,1) \times \mathbf{Y})$ *and satisfies the properties* $(H1) - (H2)$.

Remark In the two-scale elastodynamic model formulation, the linear elastic tensor is expressed on the macroscopic (or slow) variable by

$$\mathbf{C}^{\varepsilon}(p,\mathbf{x}) = \mathbf{C}(p, \frac{\mathbf{x}}{\varepsilon})$$

being $\mathbf{x} \in \Omega$, in such a way that $\mathbf{C} \in \mathcal{T}(\alpha, \beta, (0,1) \times \mathbf{Y})$. Recall also that, the ε parameter indicates the relation of micro-to-macro scale (3.3).

Following the two-scale homogenization procedure studied in the sections before, the homogenized problem governing the macroscopic mechanical behavior is of elastic type with effective coefficients defined at porosity $p \in (0,1)$ by:

$$C^{hom}_{ijrs}(p) = \frac{1}{|\mathbf{Y}|}\int_{\mathbf{Y}} C_{ijrs}(p,\mathbf{y})\,\mathrm{d}y + \frac{1}{|\mathbf{Y}|}\int_{\mathbf{Y}} C_{ijkl}(p,\mathbf{y})\mathbf{e}_{kl,y}(N^{rs}(p))\,\mathrm{d}y \tag{2.34}$$

for each $i, j, r, s \in \{1,2,3\}$, where the vector functions $(N^{rs})_{rs}$ are defined as the unique $\mathbf{Y}$-periodic solution to the cell problems, satisfying for each $i \in \{1,2,3\}$, the equality:

$$-\partial_{y_j}\left[C_{ijkl}(p,\mathbf{y})\mathbf{e}_{kl}(N^{rs}(p,\mathbf{y})\right] = \partial_{y_j}\left[C_{ijrs}(p,\mathbf{y})\right] \tag{2.35}$$

with the normalization condition $\langle N^{rs}\rangle_{\mathbf{Y}} = \mathbf{0}$. Such a condition is necessary to obtain a well-posed elliptic problem on the space $\mathbf{H}^1(\mathbf{Y})$. Explicitly, vector solutions $N^{rs}(\cdot,p)$ to the cell problem are found on

$$\mathbf{H}^1_0(\mathbf{Y}) := \left\{ N(p) \in \mathbf{H}^1(\mathbf{Y}) \,:\, \langle N(p)\rangle_{\mathbf{Y}} = \mathbf{0} \right\}$$

Variational Formulations

Solutions to problem (2.35) are found via variational formulation of such problem for each $r, s \in \{1,2,3\}$. In all that follows, it is assumed a condition of radial symmetry on the

coefficients[7] $C_{\mathrm{i}jkl}(\mathbf{y})$ which applied to (2.35) gives us the desired equivalent problem:

$$\left\{\begin{array}{c}\text{Find a function } N^{rs}\in\mathbf{H}^1_0(\mathbf{Y}) \text{ such that}\\ \int\limits_{\mathbf{Y}} C_{\mathrm{i}jkl}(p,\mathbf{y})\mathbf{e}_{kl,y}(N^{rs})\,\partial_{y_j}(v_{\mathrm{i}})\,\mathrm{d}\mathbf{y}=-\int\limits_{\mathbf{Y}} C_{\mathrm{i}jrs}(p,\mathbf{y})\partial_{y_j}(v_{\mathrm{i}})\,\mathrm{d}\mathbf{y}\quad\forall v\in\mathbf{H}^1_0(\mathbf{Y}).\end{array}\right. \tag{2.36}$$

Note the variational formulation (2.36) can be rewritten by the symmetry of the operator $\mathbf{C}(\cdot,p)$ in the form:

$$\left\{\begin{array}{c}\text{Find a function } N^{rs}(p)\in\mathbf{H}^1_0(\mathbf{Y}) \text{ such that}\\ \int\limits_{\mathbf{Y}} C_{\mathrm{i}jkl}(p,\mathbf{y})\mathbf{e}_{kl,y}(N^{rs})\,\mathbf{e}_{kl,y}(v)\,\mathrm{d}\mathbf{y}=-\int\limits_{\mathbf{Y}} C_{\mathrm{i}jrs}(p,\mathbf{y})\mathbf{e}_{\mathrm{i}j,y}(v)\,\mathrm{d}\mathbf{y}\quad\forall v\in\mathbf{H}^1_0(\mathbf{Y}).\end{array}\right. \tag{2.37}$$

Let us now define the following useful notation for the contraction of the last two indexes:

Definition 2.9 *Let us consider* $\mathbf{a}=(a_{\mathrm{i}j})_{\mathrm{i}j}$ *and* $\mathbf{b}=(b_{\mathrm{i}j})_{\mathrm{i}j}$ *elements in* $\mathcal{M}_{\mathrm{d}\times\mathrm{d}}(\mathbb{R})$*, and consider* $\mathbf{A}=(A_{\mathrm{i}jkl})_{ijkl}$ *a element of* $\mathbf{T}([0,1]\times\mathbf{Y})$ *identified with their multidimensional array. It is defined the contraction of the (last) two indices by*

$$\mathbf{a}:\mathbf{b}:=a_{\mathrm{i}j}b_{\mathrm{i}j}$$

and naturally extending the definition to three elements in the form:

$$\mathbf{A}:\mathbf{a}:\mathbf{b}:=A_{\mathrm{i}jkl}a_{kl}b_{\mathrm{i}j}$$

Remark In particular, since $\mathbf{A}\in\mathbf{T}((0,1)\times\mathbf{Y})$ then it can be deduced the symmetry conditions $A_{\mathrm{i}jkl}=A_{kl\mathrm{i}j}=A_{\mathrm{i}jlk}$, which allows to obtain a conmutative property between $\mathbf{a},\mathbf{b}$ two matrices:

$$\mathbf{A}:\mathbf{a}:\mathbf{b}=\mathbf{A}:\mathbf{b}:\mathbf{a} \tag{2.38}$$

Symmetries

As before, let us denote the base of $\mathbf{Sym}^{\mathrm{d}}$ by the set $(m_{\mathrm{i}j})_{\mathrm{i}j}$ for each $\mathrm{i},j\in\{1,\dots\mathrm{d}\}$, i.e., the set of $\mathrm{d}\times\mathrm{d}$ matrices with 1 at the entry (i,j) and 0 otherwise. Observe that the homogenized coefficient (2.34) (where it is assumed w.l.o.g $|\mathbf{Y}|=1$) can be rewritten with the previously defined notation in the form:

$$\begin{array}{rcl} C^{hom}_{\mathrm{i}jrs}(p) & = & \displaystyle\int\limits_{\mathbf{Y}}\mathbf{C}(\mathbf{y},p):m_{rs}:m_{\mathrm{i}j}+\int\limits_{\mathbf{Y}}\mathbf{C}(\mathbf{y},p):\mathbf{e}(N^{rs}):m_{\mathrm{i}j}\,\mathrm{d}\mathbf{y}\\ & = & \displaystyle\int\limits_{\mathbf{Y}}\mathbf{C}(\mathbf{y},p):\big(m_{rs}+\mathbf{e}(N^{rs})\big):m_{\mathrm{i}j}\,\mathrm{d}\mathbf{y}\end{array} \tag{2.39}$$

Moreover, expression (2.37) can be rewritten in the form:

$$\int\limits_{\mathbf{y}}\mathbf{C}(\mathbf{y},p):\mathbf{e}(v):\mathbf{e}(N^{rs})\,\mathrm{d}\mathbf{y}=-\int\limits_{\mathbf{y}}\mathbf{C}(\mathbf{y},p):\mathbf{e}(v):m_{rs}\,\mathrm{d}\mathbf{y}\quad\forall v\in\mathbf{H}^1_0(\mathbf{Y})\,\mathrm{d}\mathbf{y} \tag{2.40}$$

[7]Such kind of condition, which is naturally presented in periodic and compound media is assumed throughout this study, moreover the numerical results developed are obtained over a formulation of bone satisfying that property since the model is defined as compounds material with the inclusion being of different kind where the surrounding is a known fixed material. It is important to observe that under such assumptions the term associated to $\partial\mathbf{Y}$ vanishes obtaining the expression observed on (2.36).

So, by using the above equality (2.40) with $v = N^{ij}$ in the expression (2.39), it is obtained the homogenized coefficient in the form:

$$C^{hom}_{\mathrm{i}jkl}(p) = \int_{\mathbf{Y}} \mathbf{C}(\mathbf{y}, p) : (m_{rs} + \mathbf{e}(N^{rs})) : (m_{\mathrm{i}j} + \mathbf{e}(N^{\mathrm{i}j}))\, \mathrm{d}\mathbf{y} \tag{2.41}$$

It follows then from (2.41) the full symmetric properties of the elements C^{hom}_{ijkl}, since by (2.37) follows the that $N^{rs}(p, \mathbf{y}) = N^{sr}(p, \mathbf{y})$ thus taking into account the symmetry of $\mathbf{C}(p)$ it can be deduced:

$$C^{hom}_{\mathrm{i}jkl} = C^{hom}_{klij} = C^{hom}_{\mathrm{i}jlk} \quad \forall \mathrm{i}, j, k, l \in \{1, 2, 3\}$$

which implies in particular the usage of engineering *Voigt* notation for the homogenized equations, obtaining a standard elasticity tensor.

In all that follows, it will be denoted by $M(\mathbf{Y})$ the space of $\mathrm{d} \times \mathrm{d}$ matrices $L^2(\mathbf{Y})$ entries with norm $\|\cdot\|_{M(\mathbf{Y})}$ defined for $A = (A_{kl})_{kl} \in M(\mathbf{Y})$ by

$$\|A\|_{M(\mathbf{Y})} = \Big(\sum_{k,l=1}^{\mathrm{d}} \|A_{kl}\|^2_{L^2(\mathbf{Y})} \Big)^{1/2} \tag{2.42}$$

Let us recall the coercivity condition over $\mathbf{C}(p, \cdot)$, applying a duality argument over the space $M(\mathbf{Y})$ it follows that:

$$\|\mathbf{e}(N^{rs}(p))\|_{M(\mathbf{Y})} \leq \frac{\beta}{\alpha} \tag{2.43}$$

which will be useful in the estimation in the following subsections. Observe with the above definition, the elastic tensors belong to $lin(M(\mathbf{Y}))$.

2.5.2 About the Continuity

To study the continuity condition on the effective coefficients $C^{hom}_{\mathrm{i}jkl}(\cdot)$, let $p, q \in (0, 1)$ be two porosity levels. It will be first shown a useful estimation of $N^{rs}(p) - N^{rs}(q)$ for each $r, s \in \{1, 2, 3\}$. Using (2.37) rewritten in tensor notation, the following equality can be obtained that relates the cell solutions to their coefficients associated to the porosity level in the form:

$$\begin{aligned} \int_{\mathbf{Y}} \mathbf{C}(\mathbf{y}, p) : \mathbf{e}\big(N^{rs}(p) - N^{rs}(q)\big) : \mathbf{e}(v) = &- \int_{\mathbf{Y}} \mathbf{C}(p) - \mathbf{C}(q) : m_{rs} : \mathbf{e}(v) \\ &- \int_{\mathbf{Y}} \mathbf{C}(p) - \mathbf{C}(q) : \mathbf{e}(N^{rs}(q)) : \mathbf{e}(v). \end{aligned} \tag{2.44}$$

So that, using (2.44) it follows the representation $\forall v \in \mathbf{H}^1_0(\mathbf{Y})$

$$\int_{\mathbf{Y}} \mathbf{C}(p) : \mathbf{e}\big(N^{rs}(p) - N^{rs}(q)\big) : \mathbf{e}(v) = - \int_{\mathbf{Y}} \mathbf{C}(p) - \mathbf{C}(q) : m_{rs} + \mathbf{e}(N^{rs}(q)) : \mathbf{e}(v). \tag{2.45}$$

Applying then a duality argument on (2.45) since $M(\mathbf{Y})^* = M(\mathbf{Y})$ it is deduced the first estimate for the difference between the cell solutions, expressed by:

$$\|\mathbf{C}(p) : \mathbf{e}\big(N^{rs}(p) - N^{rs}(q)\big)\|_{M(\mathbf{Y})} \leq \|\mathbf{C}(p) - \mathbf{C}(q) : m_{rs} + \mathbf{e}(N^{rs}(q))\|_{M(\mathbf{Y})}$$

from which after taking Hölder inequality and recalling the coercivity of $\mathbf{C}(p)$ it is possible to obtain:

$$\|\mathbf{e}\big(N^{rs}(p) - N^{rs}(q)\big)\|_{M(\mathbf{Y})} \leq \alpha^{-1}\|\mathbf{C}(p) - \mathbf{C}(q)\|_{lin(M(\mathbf{Y}))}\|m_{rs} + \mathbf{e}(N^{rs}(q))\|_{M(\mathbf{Y})}. \tag{2.46}$$

Let us then estimate the difference between the homogenized coefficients associated to the porosities p, q. By applying the definition and rearranging terms it follows:

$$\begin{aligned} C^{hom}_{ijrs}(p) - C^{hom}_{ijrs}(q) &= \int_{\mathbf{Y}} \mathbf{C}(p) : m_{rs} + \mathbf{e}(N^{rs}(p)) : m_{ij} - \int_{\mathbf{Y}} \mathbf{C}(q) : m_{rs} + \mathbf{e}(N^{rs}(q)) : m_{ij} \\ &= \int_{\mathbf{Y}} \mathbf{C}(p) - \mathbf{C}(q) : m_{rs} + \mathbf{e}(N^{rs}(p)) : m_{ij} \\ &\quad + \int_{\mathbf{Y}} \mathbf{C}(q) : \mathbf{e}(N^{rs}(p)) - \mathbf{e}(N^{rs}(q)) : m_{ij} \end{aligned}$$

and by applying the Hölder inequality and using (2.46) it follows:

$$\begin{aligned} |C^{hom}_{ijrs}(p) - C^{hom}_{ijrs}(q)| \leq \|\mathbf{C}(p) - \mathbf{C}(q)\|_{lin(M(\mathbf{Y}))}\|m_{rs} + \mathrm{e}(N^{rs}(p))\|_{M(\mathbf{Y})} \\ + \frac{\beta}{\alpha}\|\mathbf{C}(p) - \mathbf{C}(q)\|_{lin(M(\mathbf{Y}))}\|m_{rs} + \mathbf{e}(N^{rs}(q))\|_{M(\mathbf{Y})} \end{aligned} \tag{2.47}$$

Finally, applying the estimation (2.43) over (2.47) it follows the continuity property for the coefficients:

$$|C^{hom}_{ijrs}(p) - C^{hom}_{ijrs}(q)| \leq \|\mathbf{C}(p) - \mathbf{C}(q)\|_{lin(M(\mathbf{Y}))}(1 + \frac{\beta}{\alpha})\frac{\beta}{\alpha} \tag{2.48}$$

2.5.3 About the Derivative

Our interest now is to obtain some estimates for the derivatives with respect to the porosity p. By using the expression (2.41) for fixed $\mathrm{i}, j, r, s \in \{1, 2, 3\}$ and $\overline{p} \in (0, 1)$ it can be deduced:

$$\partial_p C^{hom}_{ijkl}(\overline{p}) = \int_{\mathbf{Y}} \partial_p\big(\mathbf{C}(\mathbf{y}, \overline{p})\big) \,:\, m_{rs} + \mathbf{e}(N^{rs}(\overline{p})) \,:\, m_{ij} + \mathbf{e}(N^{\mathrm{ij}}(\overline{p}))\,\mathrm{d}\mathbf{y} \tag{2.49}$$

which results by distributing each term, rules of differentiation and (2.40).

It follows then from (2.49) after applying holder inequality that:

$$|\partial_p C^{hom}_{ijrs}(\overline{p})| \leq \|\mathbf{C}(\overline{p})\|_{lin(M(\mathbf{Y}))}\|m_{rs} + \mathbf{e}(N^{rs}(\overline{p}))\|_{M(\mathbf{Y})}\|m_{ij} + \mathbf{e}(N^{\mathrm{ij}}(\overline{p}))\|_{M(\mathbf{Y})}$$

which after applying the estimate (2.43) the following inequality for the derivative can be deduced:

$$|\partial_p C^{hom}_{\mathrm{i}jrs}(p)| \leq (1+\frac{\beta}{\alpha})^2 \|\partial_p \mathbf{C}\|_{L^\infty((0,1);lin(M(\mathbf{Y}))} \tag{2.50}$$

The above estimates enable us to obtain a bound for the difference of the homogenized elastic tensors.

Now, let $\overline{p}, \overline{q}$ be two porosity level on $(0,1)$. Applying the equality (2.49), rearranging terms and using directly Hölder inequality, it follows:

$$\begin{aligned}
|\partial_p C_{\mathrm{i}jrs}(\overline{p}) - \partial_p C_{\mathrm{i}jrs}(\overline{q})| \leq \\
&\|\partial_p \mathbf{C}(\overline{p}) - \partial_p \mathbf{C}(\overline{q})\|_{lin(M(\mathbf{Y}))} \|m_{rs} + \mathbf{e}(N^{rs}(\overline{p}))\|_{M(\mathbf{Y})} \|m_{j\mathrm{i}} + \mathbf{e}(N^{\mathrm{i}j}(\overline{p}))\|_{M(\mathbf{Y})} \\
&+ \|\partial_p \mathbf{C}(\overline{q})\|_{lin(M(\mathbf{Y}))} \|\mathbf{e}(N^{rs}(\overline{p})) - \mathbf{e}(N^{rs}(\overline{q}))\|_{M(\mathbf{Y})} \|m_{ij} + \mathbf{e}(N^{\mathrm{i}j}(\overline{q})\|_{M(\mathbf{Y})} \\
&+ \|\partial_p \mathbf{C}(\overline{q})\|_{lin(M(\mathbf{Y}))} \|m_{rs} + \mathbf{e}(N^{rs}(\overline{p}))\|_{M(\mathbf{Y})} \|\mathbf{e}(N^{\mathrm{i}j}(\overline{p})) - \mathbf{e}(N^{\mathrm{i}j}(\overline{q}))\|_{M(\mathbf{Y})}
\end{aligned}$$

From which can be deduced taking into consideration the bounds for the cell solutions (2.43), (2.46) that:

$$\begin{aligned}
|\partial_p C_{\mathrm{i}jrs}(\overline{p}) - \partial_p C_{\mathrm{i}jrs}(\overline{q})| \leq (1+\frac{\beta}{\alpha})^2 \|\partial_p \mathbf{C}(\overline{p}) - \partial_p \mathbf{C}(\overline{q})\|_{lin(M(\mathbf{Y}))} \\
+ 2\frac{\beta}{\alpha}(1+\frac{\beta}{\alpha})^2 \|\partial_p \mathbf{C}(\overline{q})\|_{lin(M(\mathbf{Y}))} \|\mathbf{C}(\overline{p}) - \mathbf{C}(\overline{q})\|_{lin(M(\mathbf{Y}))}
\end{aligned} \tag{2.51}$$

As conclusion, it is obtained the following properties:

Proposition 2.10 *Under the assumptions of regularity for the multiscale elastic coefficients* $\mathbf{C} = (C_{\mathrm{i}jkl})_{\mathrm{i}jkl} \in \mathcal{T}(\alpha, \beta, (0,1) \times \mathbf{Y})$ *of type:*

HI A Lipschitz continuity assumption for the elastic coefficients in the form:

$$\|\mathbf{C}(\overline{p}) - \mathbf{C}(\overline{q})\|_{lin(M(\mathbf{Y}))} \leq L|\overline{p} - \overline{q}|^l$$

for some $L, l > 0$ *positive constants, and each* $\overline{p}, \overline{q} \in (0,1)$.

Then it follows for each $\mathrm{i}, j, r, s \in \{1,2,3\}$ *and* $\overline{p}, \overline{q}$ *porosity levels:*

PI A continuity property for the homogenized coefficients:

$$|C^{hom}_{\mathrm{i}jrs}(\overline{p}) - C^{hom}_{\mathrm{i}jrs}(\overline{q})| \leq L|\overline{p} - \overline{q}|^l \frac{\beta}{\alpha}(1+\frac{\beta}{\alpha})$$

Moreover, if it is satisfied:

HII Uniformly boundness over the porosity range for the derivative, i.e., $\|\partial_p \mathbf{C}(\overline{q})\|_{lin(M(\mathbf{Y}))} < \infty$ *for each* $\overline{q} \in (0,1)$.

HIII Lipschitz continuity condition for the derivative, in the form:

$$\|\partial_p \mathbf{C}(\overline{p}) - \partial_p \mathbf{C}(\overline{q})\|_{lin(M(\mathbf{Y}))} \leq \overline{L}|\overline{p} - \overline{q}|^{\overline{l}}$$

for $\overline{L}, \overline{l} > 0$ *constants and each* $\overline{p}, \overline{q} \in (0,1)$.

Then it follows that each $\mathrm{i}, j, r, s \in \{1, 2, 3\}$ *and* $\overline{p}, \overline{q}$ *porosity levels:*

PII A continuity property for the derivatives of hom. coeffients:

$$|\partial_p C^{hom}_{\mathrm{i}jrs}(\overline{p}) - \partial_p C_{\mathrm{i}jrs}(\overline{q})| \leq C(\alpha, \beta)|\overline{p} - \overline{q}|^{\bar{l}} + \tilde{C}(\alpha, \beta)|\overline{p} - \overline{q}|^{l}$$

being $C(\alpha, \beta), \tilde{C}(\alpha, \beta) > 0$ *constants.*

Chapter 3

Discretization Procedures

Discretization procedures for elastic formulation have been developed since the early 60's under diverse setting oriented mainly in civil-engineering fields. In this section, it will be presented following literature [10], [19] a finite-element discretization scheme for the space-domain and a standard β-Newmark time-domain discretization, thus a complete numerical formulation for various elastic models implemented in `FEniCS`, a state-of-art library for such purposes joint with `Python` language.

3.1 Numerical Schemes

To discretize the elastodynamic model, it will be assumed that the solution is defined on a Banach space $\mathbf{V}$, in which the elasticity operator defined from the tensor $\mathbf{C}^{hom} = (C^{hom}_{\mathrm{i}jkl})_{\mathrm{i}jkl}$ by:

$$\mathcal{I}_{C^{hom}}(u, v) := \int_{\Omega} C^{hom}_{\mathrm{i}jkl} \mathbf{e}_{kl}(u) \mathbf{e}_{\mathrm{i}j}(v) \, \mathrm{d}x \quad \forall u, v \in \mathbf{V}$$

is well-defined in the sense that conditions of coercivity on the operator are assured from the uniformly ellipticity of $C^{hom}_{\mathrm{i}jkl}$.

3.1.1 Approximation by Finite Spaces

The solution of the elastodynamic problem will be found as projection solutions of finite dimensional subspaces that approximate to solution space[1], in this case $\mathbf{H}^1(\Omega, \Gamma_D)$. Let $\{\mathbf{V}_h\}_{0 \leq h \leq 1}$ be a family of finite-dimensional subspaces of $\mathbf{V}$, assume that there exist a dense subspace $\mathbf{W} \subset \mathbf{V}$, a linear interpolator $\Pi_h \in \mathcal{L}(\mathbf{W}; \mathbf{V}_h)$, integer $k > 0$ such that our finite dimensional solution approximation Π_h with associated to a mesh size $h > 0$ satisfies:

$$\|v - \Pi_h v\|_{\mathcal{L}(\mathbf{W}; \mathbf{V}_h)} \leq h^{k+1} \|v\|_{\mathbf{W}} \quad \forall v \in \mathbf{W}$$

[1]Such workflow is defines the approximation theory of PDE solutions and the so-called finite elements method [10].

Remark In our case under study it is used $\mathbf{V} = \mathbf{L}^2(\Omega)$ and $\mathbf{W} = \mathbf{H}^1(\Omega, \Gamma_D)$ being $\mathbf{V}_h$ the $\mathbf{H}^1$-conformal finite element spaces using as reference element $\{\hat{K}, \hat{P}, \hat{\sigma}\}$ of *Lagrange* type with typical order $k \in \{1, 2\}$, such that $\mathbb{P}_k \subset \hat{P}$ with $\mathbf{W} := \mathbf{H}^{k+1}(\Omega) \cap \mathbf{H}^1(\Omega, \Gamma_D)$

Over such finite dimensional subspaces $\{\mathbf{V}_h\}_{h>0}$ the approximate solution can be found, satisfying the problem for each $h > 0$:

$$\left\{ \begin{array}{cc} \text{Find } u_h \in \mathcal{C}^2(0,T;\mathbf{V}_h) & \text{such that} \\ (\rho^0 \mathrm{d}_{tt} u_h(t), v_h)_\Omega + \mathcal{I}_{C^{hom}}(u_h(t), v_h) = (\mathbf{F}(t), v_h)_{\Gamma_N} & \forall v_h \in \mathbf{V}_h \\ \mathrm{d}_t u_h(0) = u_h(0) = \mathbf{0} & \end{array} \right. \tag{3.1}$$

Problem (3.1) corresponds to a finite linear PDE system in time for the variable $u_h(t)$ where the existence can be obtained by application of the spectral theory decomposing the elastic operator in its spectrum. The treatment is similar to the procedure proposed in the above section [19].

The space discretization then is obtained from (3.1) which corresponds to a system of Ordinary Differential Equations (ODEs). Indeed, let $\{\varphi_1, \ldots, \varphi_{N(h)}\}$ denote a basis for the finite dimensional space $\mathbf{V}_h$ or so-called global shape functions for $\mathbf{V}_h$, then for all $t \in (0, T)$ the approximate solution $u_h(t) \in \mathbf{V}_h$ can be expanded as

$$u_h(\mathbf{x}, t) = \sum_{\mathrm{i}=1}^{N(h)} \mathbf{U}_\mathrm{i}(t) \varphi_\mathrm{i}$$

where it is used the notation $\mathbf{U}(t) = (U_\mathrm{i}(t))_{1 \leq \mathrm{i} \leq N} \in \mathbb{R}^{N(h)}$.

Now, introducing also $\mathbf{F}_h(t) = \big((\mathbf{F}(t), \varphi_\mathrm{i})_\Omega\big)_{1 \leq \mathrm{i} \leq N} \in \mathbb{R}^{N(h)}$ with the so-called stiffness $\mathcal{A}(t) \in \mathbb{R}^{N(h) \times N(h)}$ and stress $\mathcal{M} \in \mathbb{R}^{N(h) \times N(h)}$ matrices respectively by:

$$\mathcal{A}_{\mathrm{i}j}(t) = \mathcal{I}_C(\varphi_j, \varphi_\mathrm{i}),\ \mathcal{M}_{\mathrm{i}j} = (\sqrt{\rho^0}\varphi_\mathrm{i}, \sqrt{\rho^0}\varphi_j)_\Omega \quad 1 \leq \mathrm{i}, j \leq N(h)$$

By the previous hypothesis $\mathcal{A}(t)$ is symmetric and positive-definite whereas $\mathcal{M}_{\mathrm{i}j}$ is positive definite. Under such notation, it follows the time-dependent matrix form formulation :

$$\left\{ \begin{array}{cc} \text{Find } \mathbf{U} \in \mathcal{C}^2(0,T;\mathbb{R}^{N(h) \times N(h)}) & \text{such that} \\ \mathcal{M} \mathrm{d}_{tt} \mathbf{U}(t) + \mathcal{A}\mathbf{U}(t) = \mathbf{F}_h(t) & \text{in } (0,T) \\ \mathrm{d}_t \mathbf{U}(0) = \mathbf{U}(0) = \mathbf{0} & \end{array} \right. \tag{3.2}$$

which describes the full space discretization scheme by means of the FEM method, and enabling the use of time discretization techniques for the resulting ODE problem (3.2). In particular as will be seen in the next section the so-called β-Newmark scheme. [2]

[2] The implementation of such space discretization is done in Python using a state-of-art open-source project called `FEniCS` [13], defined as a set of specific core component such as `DOLFIN`, `UFL`, `UFC`, etc. It enables the automatic solution of differential forms implementing the Theory of Finite Elements with numerically optimized libraries for arithmetic computations. The project is an international collaboration initiated in 2003 between the University of Chicago and Chalmers University of Technology currently under development from a variety of institutions.

3.1.2 Time Discretization

Let us note that (3.2) defines a standard *Cauchy* ODE problem. To solve numerically such system, it will be introduced an uniform time-step discretization of $(0,T)$ in the form $\Delta t = T/N_T$ such that:

$$t_n = n\Delta t, \quad 0 \leq n \leq N_T$$

being $N_T \in \mathbb{N}^*$ some fixed number of time steps.

It will be found for each $n \in \{1,\ldots,N_T\}$ an approximate sequence tuple (u_n, v_n, a_n) of the solutions $(u(t_n), \partial_t u(t_n), \partial_{tt} u(t_n))$ being the method chosen the so-called β-*Newmark*, a well-known scheme to study mechanically driven behavior [19].

Taking into account the time-domain regularity from the solution $u^{(0)}(t,\mathbf{x}) := u(t,\mathbf{x})$ of the homogenized PDE problem (result analogous to 2.2), let us note that by using the *Taylor* expansion on $u \in \mathcal{C}^p(0,T;\mathbf{H}^1(\Omega,\Gamma_D))$ and the mean value theorem that for the displacement at time t_{n+1} it follows:

$$u(t_{n+1}) = u(t_n) + \Delta t\, \partial_t u(t_n) + \Delta t^2 \left(\beta \partial_{tt} u(t_{n+1}) + (\frac{1}{2} - \beta)\partial_{tt} u(t_{n+1})\right) + \mathcal{O}(\Delta t^3)$$

and for the velocity

$$\partial_t u(t_{n+1}) = \partial_t u(t_n) + \Delta t \left(\gamma \partial_{tt} u(t_{n+1}) + (1-\gamma)\partial_{tt} u(t_n)\right) + \mathcal{O}(\Delta t^2)$$

being β, γ two parameters with $0 < 2\beta < 1$, $0 < \gamma < 1$. The β-Newmark scheme consist then in a approximation of the above equations by using a finite difference scheme in the form:

$$u_{n+1} = u_n + \Delta t\, v_n + \Delta t^2 \left(\beta a_{n+1} + (\frac{1}{2} - \beta)a_n\right) \tag{3.3}$$

$$v_{n+1} = v_n + \Delta t \left(\gamma a_{n+1} + (1-\gamma)a_n\right) \tag{3.4}$$

From (3.3) it is defined the numerical procedure by a two-step update given as follows:

$$\text{(Stage 1)} \longrightarrow a_{n+1} = \frac{1}{\beta \Delta t^2}(u_{n+1} - u_n - \Delta t\, v_n) - \frac{(1-2\beta)}{2\beta} a_n, \quad \forall\, 0 \leq n \leq N_T - 1 \tag{3.5}$$

$$\text{(Stage 2)} \longrightarrow v_{n+1} = v_n + \Delta t \left((1-\gamma)a_n + \gamma a_{n+1}\right), \quad \forall\, 0 \leq n \leq N_T - 1 \tag{3.6}$$

Let us now show the precision of the β-*Newmark* scheme. Note that the elastodynamic equation contains two derivatives in time, so that taking into account the above and applying again *Taylor* expansion and the mean value theorem, it follows as Δt tends to zero that:

$$u(t_{n+1}) = u(t_n) + \Delta t\, \partial_t u(t_n) + \Delta t \left(\beta \partial_{tt} u(t_{n+1}) + (\frac{1}{2} - \beta)\partial_{tt} u(t_n)\right) + \Delta t^3 (\frac{1}{6} - \beta)\partial_{ttt} u(t_n) + \mathcal{O}(\Delta t^4) \tag{3.7}$$

$$\partial_t u(t_{n+1}) = \partial_t u(t_n) + \Delta t \left(\gamma \partial_{tt} u(t_{n+1}) + (1-\gamma)\partial_{tt} u(t_n)\right) + \Delta t^2 \left(\frac{1}{2} - \gamma\right)\partial_{ttt} u(t_n) + \mathcal{O}(\Delta t^3) \quad (3.8)$$

so that, the scheme results of precision $\mathcal{O}(\Delta t)$ for $\gamma \neq 1/2$ and $\mathcal{O}(\Delta t^2)$ for $\gamma = 1/2$.

Applying now such two-step scheme (3.5) over (3.2) it follows the matrix system update procedure:

$$\frac{1}{\beta \Delta t}\mathcal{M}(\mathbf{U}_{n+1} - \mathbf{U}_n - \Delta t\, \mathbf{V}_n) - \frac{1}{\beta}\left(\frac{1}{2} - \beta\right)\mathcal{M}\mathbf{A}_n + \mathcal{A}\mathbf{U}_{n+1} = \mathbf{F}_h \quad 0 \leq n \leq N_T - 1 \quad (3.9)$$

$$\frac{1}{\gamma \Delta t}\mathcal{M}(\mathbf{V}_{n+1} - \mathbf{V}_n) - \frac{1}{\gamma}(1-\gamma)\mathcal{M}\mathbf{A}_n + \mathcal{A}\mathbf{U}_{n+1} = \mathbf{F}_h \quad 0 \leq n \leq N_T - 1 \quad (3.10)$$

Note that such a time step iteration (3.9) corresponds to solve the linear system of equations defined for the function $\mathbf{U}_{n+1}$ in the form:

$$(\mathcal{M} + \beta \Delta t^2\, \mathcal{A})\mathbf{U}_{n+1} = \mathbf{F}_{n+1}$$

being $\mathbf{F}_{n+1} \in \mathbb{R}^{I(h)}$ known and then update the solution $\mathbf{U}_n$ field using the (3.5). Now, since the $\beta \geq 0$, if follows that the $\mathbf{R}^{I(h)} \times \mathbf{R}^{I(h)}$ matrix $(\mathcal{M} + \beta \Delta t^2 \mathcal{A})$ is positive definite and moreover its symmetric.

3.2 Dynamic Type Models

The discretization procedures defined before enables the implementation of step-wise procedures of homogenized fully elastodynamic models, its attenuated version to bypass resonance effects shown in the frequency domain formulation and Viscoelastic formulations.

3.2.1 Fully Elastodynamic

Taking into account our homogenized elastodynamic model (2.18) described explicitly:

$$\begin{cases} \text{Find } u \in \mathcal{C}^2(0,T;\mathbf{H}^1(\Omega,\Gamma_D)) & \text{such that} \\ \rho^0 \partial_{tt} u^{(0)}(t,\mathbf{x}) - \nabla \cdot \sigma^0(u^{(0)}(t,\mathbf{x})) = \mathbf{0} & \text{in } (0,T)\times\Omega \\ \sigma^0_{ij}(u^{(0)}(t,\mathbf{x})) = C^{hom}_{ijkl}\mathbf{e}_{kl,x}(u^{(0)}(t,\mathbf{x})) & \text{in } (0,T)\times\Omega \\ u^{(0)}(t,\mathbf{x}) = \mathbf{0} & \text{on } (0,T)\times\Gamma_D \\ \sigma^0(u^{(0)}(t,\mathbf{x}))\cdot n = \mathbf{F}(t,\mathbf{x}) & \text{on } (0,T)\times\Gamma_N \end{cases} \quad (3.11)$$

the discretization procedure over time applied on (3.11) turn into the update scheme for each $n \in \{1,\ldots,N\}$ in the form:

$$\frac{\rho^0}{\beta(\Delta t)^2}u_{n+1} - \nabla\cdot\sigma(u_{n+1}) = \frac{\rho^0}{\beta(\Delta t)^2}(u_n + (\Delta t)v_n) + \rho^0\frac{(1-2\beta)}{2\beta}a_n$$

with fields update (3.5).

3.2.2 Elastodynamic Attenuated

The presence of eigen-frequencies in the elastodynamic operator gives a bad numerical solution after solving the discrete system in the frequency domain. This problem can be bypassed using a regularization factor, or moreover, a kind of viscosity term which changes the eigen-frequencies and stabilizes the discrete system resulting in *good* approximation to the experimental results.
In this case, we add a term which in viscoelastic literature resembles a *Kelvin-Voigt* type behavior. It is added such term scaled with parameter ε, so that the overall behavior is not abruptly disrupted but is well-posed in the set of real frequencies.

Remark One possible way to see this technique is to consider the fact that we are moving the real frequencies ω to $\omega - \mathrm{i}\varepsilon$, it let us be away from the eigen-frequencies of the operator $\mathcal{I}_{C^{hom}}$, but the overall behavior of the real part remains close to the experimental setting.

So, it is modeled the material as function of displacement $u(\mathbf{x}, t) \in H^1(\Omega)$ (after the homogenization procedure) being $\Omega \subset \mathbb{R}^2$ a sufficiently regular domain, with *Lipschitz* boundary $\partial\Omega := \Gamma_D \cup \Gamma_N$. Explicitly, the regularized elastic model in defined by:

$$\begin{cases} \rho^0 \partial_{tt} u^{(0)} - \varepsilon \partial_t u^{(0)} - \nabla \cdot \sigma^0(u^{(0)}) = \mathbf{0} & \text{in } (0,T)\times\Omega \\ \sigma^0(u^{(0)}) = \mathbf{C}^{hom} : \mathbf{e}(u^{(0)}) & \text{in } (0,T)\times\Omega \\ \sigma^0(u^{(0)}) \cdot n = \mathbf{F} & \text{on } (0,T)\times\Gamma_N \\ u^{(0)} = \mathbf{0} & \text{on } (0,T)\times\Gamma_D \\ u^{(0)} = \partial_t u^{(0)} = \mathbf{0} & \text{on } \{t=0\}\times\Omega \end{cases}$$

where ε denotes a small regularization parameter associated to a Kelvin-Voigt type viscosity. As before, it is considered a time-discretization β-Newmark scheme following the two-step update procedure for each $n \in \{1, \ldots, N\}$:

$$\begin{aligned} &(\text{Stage 1}) \longrightarrow a_{n+1} = \frac{1}{\beta(\Delta t)^2}(u_{n+1} - u_n - (\Delta t)v_n) - \frac{1-2\beta}{2\beta}a_n \\ &(\text{Stage 2}) \longrightarrow v_{n+1} = v_n + \Delta t((1-\gamma)a_n + \gamma a_{n+1}) \end{aligned}$$

It is then possible to define a numerically explicit scheme for our model, with update procedure at time $n+1$ given in the form:

$$\begin{aligned} \frac{(\rho^0 - \varepsilon(\Delta t)\gamma)}{\beta(\Delta t)^2}u_{n+1} - \nabla \cdot u_{n+1} = &\frac{\rho^0}{\beta(\Delta t)^2}(u_n + (\Delta t)v_n) + \rho^0\frac{(1-2\beta)}{2\beta}a_n \\ &- \frac{\varepsilon\gamma}{\beta(\Delta t)}(u_n + (\Delta t)v_n) - \varepsilon(\Delta t)\gamma\frac{1-2\beta}{2\beta}a_n \end{aligned}$$

3.2.3 Kelvin-Voigt Viscoelastic Type

Following the developments of the above ideas, a ε-*Kelvin-Voigt* viscoelastic bone model captures the main characteristics observed in biological and biomechanical literature of bone. In this case, the model is considered of linear elastic-viscous behavior with an ε-regularization

of the viscous part. Thus, after applying the homogenization procedure, the following homogenized model is obtained:

$$\begin{cases} \rho^0 \partial_{tt} u^{(0)} - \nabla \cdot \sigma^0(u^{(0)}) = \mathbf{0} & \text{in } (0,T)\times\Omega \\ \sigma^0(u^{(0)}) = \mathbf{C}^{hom} : \mathbf{e}(u^{(0)}) + \varepsilon \mathbf{D}^0 : \mathbf{e}(\partial_t u^{(0)}) & \text{in } (0,T)\times\Omega \\ \sigma^0(u^{(0)})\cdot n = \mathbf{F} & \text{on } (0,T)\times\Gamma_N \\ u^{(0)} = \mathbf{0} & \text{on } (0,T)\times\Gamma_D \\ u^{(0)} = \partial_t u^{(0)} = \mathbf{0} & \text{on } \{t=0\}\times\Omega \end{cases}$$

The standard discretization scheme is defined by a β-*Newmark* implicit finite differences scheme for the time domain and FEM for the space domain. In this case, the time discretization is obtained in the usual two steps:

$$\begin{aligned} &\text{(Stage 1)} \longrightarrow a_{n+1} = \frac{1}{\beta(\Delta t)^2}(u_{n+1} - u_n - (\Delta t)v_n) - \frac{1-2\beta}{2\beta}a_n \\ &\text{(Stage 2)} \longrightarrow v_{n+1} = v_n + \Delta t((1-\gamma)a_n + \gamma a_{n+1}) \end{aligned}$$

So that, the update scheme obtained at times $t_n = n+1$ in the form:

$$\begin{aligned} \frac{\rho^0}{\beta(\Delta t)^2}u_{n+1} - \nabla\cdot\sigma_C^0(u_{n+1}) - \frac{\gamma\Delta t}{\beta(\Delta t)^2}\nabla\cdot\sigma_D^0(u_{n+1}) & \\ = \frac{\rho^0}{\beta(\Delta t)^2}(u_n + (\Delta t)v_n) + \rho^0\frac{(1-2\beta)}{2\beta}a_n & \\ + \nabla\cdot\sigma_D^0(v_n) + (1-\gamma)(\Delta t)\nabla\cdot\sigma_D^0(a_n) & \\ - \frac{(\Delta t)\gamma}{\beta(\Delta t)^2}\nabla\cdot\sigma_D^0(u_n + (\Delta t)v_n) & \\ - (\Delta t)\gamma\frac{1-2\beta}{2\beta}\nabla\cdot\sigma_D^0(a_n) & \end{aligned}$$

where it is used the notation $\sigma_C^0(w) = \mathbf{C} : \mathbf{e}(w)$ and $\sigma_D^0(w) = \mathbf{D} : \mathbf{e}(w)$ for $w \in \mathbf{H}^1(\Omega)$.

Chapter 4

Simulations

The numerical simulations studied in this section define the main tool for evaluation and validation of the ultrasound technique. It includes assessment of the homogenized coefficient predictions by means of the FEM method under the clinical-range of porosities regarding to standard literature, elastodynamic simulations associated to the experimental device on time- and frequency formulations and the processing of *Lamb*-modes characterizing the material behavior recorded at the receivers. In this context, aspects such as computational costs, fidelity derived from the meshes and instabilities are faced at various degrees of success. Moreover, `Python` source code to recreate the results is freely available at the repository github.com/Reidmen.

4.1 Numerical Solutions to Cell Problems

Following the developments done before to obtain effective equations governing the macroscopic mechanical behavior of cortical bone, one of the main difficulties to solve is related to the so-called cell problems which contains the non-linear component associated to the homogenized coefficients. Such a PDE problem is characterized by unique vector-valued solutions $\mathbf{N}^{rs} \in \mathbf{H}^1(\mathbf{Y})$ for each $r, s \in \{1, \dots, \mathrm{d}\}$ satisfying the elliptic PDE system:

$$\begin{cases} -\partial_{y_j}\left[C_{\mathrm{i}jkl}(\mathbf{y})\mathbf{e}_{kl,y}\big(\mathbf{N}^{rs}(\mathbf{y})\big)\right] = \partial_{y_j}\big(C_{\mathrm{i}jrs}(\mathbf{y})\big) & \text{in } \mathbf{Y} \\ \left[C_{\mathrm{i}jkl}(\mathbf{y})\mathbf{e}_{kl,\mathbf{y}}\big(\mathbf{N}^{rs}(\mathbf{y})\big)\right] n_j = \mathbf{0} & \forall \mathbf{y} \in \partial\mathbf{Y} \end{cases} \tag{4.1}$$

where it is added the condition

$$\int_{\partial Y} \mathbf{N}^{rs}(\mathbf{y})\, \mathrm{d}\mathbf{y} = \mathbf{0}$$

to obtain uniqueness, since the right hand side of (4.1) is constructed to satisfy average equal $\mathbf{0}$. The variational formulation is derived using integration by parts, in which for $\phi \in \mathbf{H}^1(\mathbf{Y})$ it follows:

$$\int_Y C_{\mathrm{i}jkl}(\mathbf{y})\mathbf{e}_{kl,\mathbf{y}}(N^{rs}(\mathbf{y}))\partial_{y_j}\phi_{\mathrm{i}} = -\int_Y C_{\mathrm{i}jrs}(\mathbf{y})\partial_{y_j}\phi_{\mathrm{i}} + \int_{\partial Y} C_{\mathrm{i}jrs}(\mathbf{y})n_j\phi_{\mathrm{i}}$$

Considering the standard biomechanical literature [12], the bone matrix is mainly made from hydroxyapatite, a material which can be modeled with a linear elastic behavior and inclusion defining the mesoscale composed mainly of saturated fluid, which in this approximation is assumed of static elastic type. Taking axial symmetry along the long axis of bone, the composed material is modeled with transverse isotropy for each component C^m_{ijkl}, C^f_{ijkl} of matrix and water phases respectively. Thus, it follows the elastic tensor C_{ijkl} defined on the cell $\mathbf{Y}$ by

$$C_{ijkl}(\mathbf{y}) := C^m_{ijkl}\mathbb{I}_{\{\mathbf{y}\in\mathbf{Y}_m\}} + C^f_{ijkl}\mathbb{I}_{\{\mathbf{y}\in\mathbf{Y}_p\}}$$

Such component-wise elastic behavior can be described explicitly using *Voigt* notation as a 6×6 matrix in the 3-dimensional case by:

$$C_{ij}(\mathbf{y}) = \begin{bmatrix} C_{11}(\mathbf{y}) & C_{12}(\mathbf{y}) & C_{13}(\mathbf{y}) & 0 & 0 & 0 \\ C_{12}(\mathbf{y}) & C_{11}(\mathbf{y}) & C_{23}(\mathbf{y}) & 0 & 0 & 0 \\ C_{13}(\mathbf{y}) & C_{23}(\mathbf{y}) & C_{23}(\mathbf{y}) & 0 & 0 & 0 \\ 0 & 0 & 0 & C_{44}(\mathbf{y}) & 0 & 0 \\ 0 & 0 & 0 & 0 & C_{44}(\mathbf{y}) & 0 \\ 0 & 0 & 0 & 0 & 0 & C_{66}(\mathbf{y}) \end{bmatrix}$$

which is given by the transverse isotropy symmetries of the material components. In particular, it is assumed that $C_{55}(\mathbf{y}) = C_{44}(\mathbf{y})$ and $C_{11}(\mathbf{y}) = C_{22}(\mathbf{y})$.

Simulations are done of the homogenized coefficients in function of the porosity level, i.e. setting the circular inclusion with radius $r(p)$ being $p \in (0,1)$ the set of admissible porosity levels, in the form $p := \frac{|\mathbf{Y}_f|}{|\mathbf{Y}|}$. Moreover, 2-dimensional and 3-dimensional cases are assumed over the microstructure to assess different aspects of symmetry.

Explicitly, an increasing array of possible porosity levels is chosen limited to the range of interest, i.e. it is limited to the $[0, 0.3]$ interval of possible porosities. The numerical solution to the model is obtained using the `UFL` language implemented within the library `FEniCS`[1] to solve PDE's in variational formulation.

In particular, it is used the `PETScKrylov` solver to solve the matrix system obtained after discretization of the variational formulation by FEM, and over such solver we used the `GMRES` (Generalized Minimal Residual Method)[2] with preconditioner given by *iLU* (incomplete LU

[1]The `FEniCS` project [13] is an international initiative, started in 2013 with the objective to automate the solution of mathematical models based of Partial Differential Equations of the type elliptic as the heat equation, hyperbolic as the wave equation, quasi-hyperbolic equations, etc., using the Finite Element theory and formalism to find such solution. More in general, its capable to find an approximate solution by means of a well-posed general variational formulation. Different use scenarios can be seen at [1].
Defined as a set of interdependent base `C++` libraries such as `DOLFIN` [14], `FIAT`, `SFC` to just mention some. `FEniCS` implements a close-to-abstract coding and procedure to solve PDE problems on interface languages such as the native `C++` or via wrappers `Python`. Moreover, such base libraries rely on high-performance libraries for the algebra computations necessary in the FEM, such as `PETSc` which implements iterative solver of *Krylov* type and a range of preconditioner to find an approximate solution $x \in \mathbb{R}^m$ of $Ax = b$ for $\mathcal{M}_{m\times m}(\mathbb{R})$, $b \in \mathbb{R}^m$ for $m \gg 1$.

[2]The `GMRES` method is an efficient algorithm to solve large linear systems. It uses an iterative method associated to the Theory of Krylov subspaces to approximate the solution of the system by reducing the high dimensional problem to a sequence of low dimensional, solved each one by least squares. Explicitly, given

factorization). Such consideration where done to tackle numerical instabilities and non-convergence results, assembling a sparse linear system with better properties for numerical inversion.

Predictions are then compared with the approximation of the homogenized coefficients for cortical bone using the same input coefficient tensor of *Parnell* and *Grimal* (PG), whom by means of a multipolar approximation to the solution of problem (4.1), obtained semi-analytic approximate expressions [18], thus enabling in this case a comparison to a FEM method proposed here to solve each of the cell problems involved in the homogenized coefficient description.

It is important to emphasize that PG solutions define the standard reference used in literature and a relevant comparison study must be done to test validity and robustness under different configurations.

4.1.1 2-Dimensional Models

Taking into account the symmetry condition assumed for the microstructure described as repetition along the long axis of bone, motivates the usage of d = 2 with a unit square microstructure domain, i.e. $\mathbf{Y} = (0,1)^2$, being the porosity of circular type.

Figure (4.1) contains the predictions of the diagonal homogenized elastic coefficients by means of the FEM, compared to the results obtained from PG. It is shown a close behavior for the results in the two different mesh sizes. The representative isotropic values, shows differences with a error percentages $< 5\%$ validating the numerical solutions.

Similarly, figure (4.2) shows the non-diagonal homogenized coefficients that describe the shear behavior again compared to the PG reference case. It shows a lower percentage error in all the coefficients describing the mechanical behavior related to the axial plane (in this case $C_{55}^{hom}, C_{23}^{hom}$), whereas the C_{66}^{hom} that describes full shear interaction on the anti-axial plane, shows a clear difference toward bigger porosity values with $> 5\%$ percentage errors.

Such failure in the prediction can be attributed to errors regarding to the boundary conditions *Neumann* conditions being imposed, and moreover to the assumption on the characteristic microstructure. Nevertheless, as the PG predictions for the C_{66}^{hom} are validated with respect to experimental data results under an error percentages of $> 5\%$, the solutions found for such coefficient cannot be rejected since the predictions in are in the same range of error.

$A \in \mathcal{M}_{m\times m}(\mathbb{R})$, $b \in \mathbb{R}^m$ for $m \gg 1$, the `GMRES` algorithm solves the problem $Ax = b$ by solving the problems

$$\min_{x\in\mathcal{K}_n} \|b - Ax\|_2$$

for increasing values of $n \in \mathbb{N}$, knowing $\mathcal{K}_n = \mathcal{K}_n(A, b)$ the Krylov space of order n defined by

$$\mathcal{K}_n(A, b) = \text{span } \{b, Ab, \ldots, A^{n-1}b\} \subset \mathbb{R}^m$$

At each iteration, its computed the residual by least squares, where under reasonable assumptions of symmetry of the matrix, the residual will be sufficiently small for $n \ll m$.

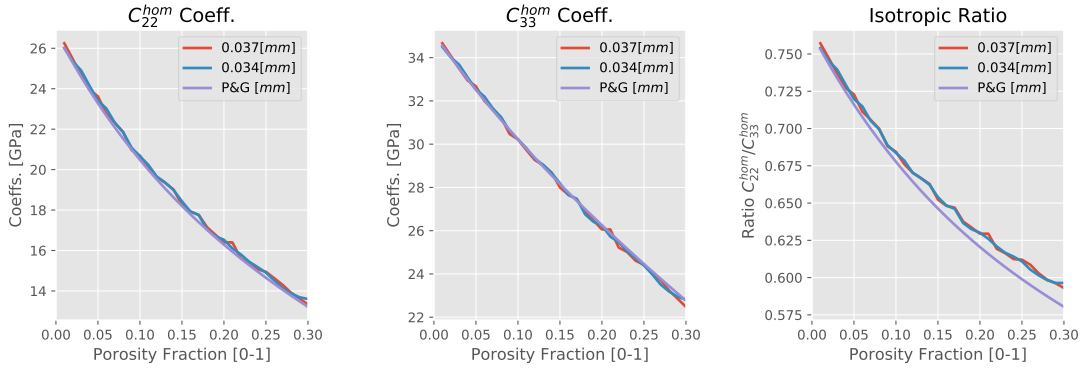

Figure 4.1: Main diagonal elastic homogenized coefficients in *Voigt* notation. They describe an transverse isotropic behavior, spanned in the figure on the biomedical range of $(1, 30)[\%]$ cortical porosity. The characteristic microstructure in this case is of unitary square. The blue, orange lines describe the FEM predictions at different mesh sizes, whereas the green line describes the PG approximation.

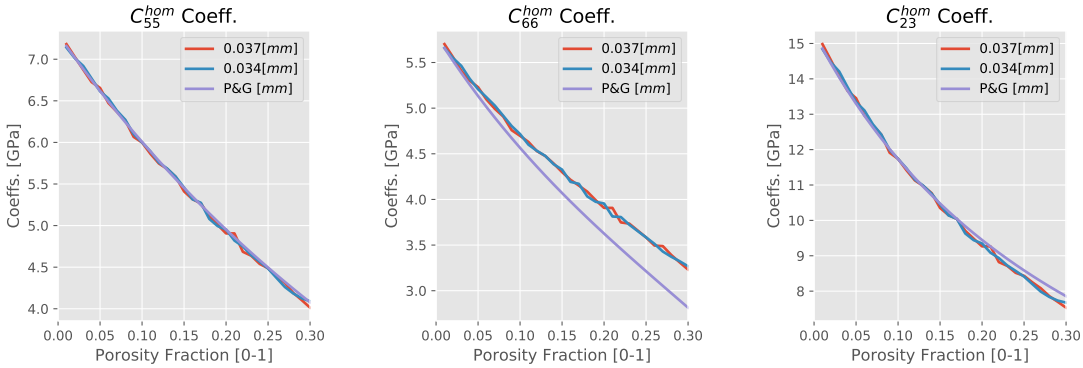

Figure 4.2: Other diagonal elastic homogenized coefficients in *Voigt* notation. They describe an transverse isotropic behavior, spanned in the figure on the biomedical range of $(1, 30)[\%]$ cortical porosity with unitary square characteristic microstructure.

The explicit results of error percentages associated to the predictions for the complete homogenized elastic tensor are shown in table (4.1). It describes the clear correspondence between coefficients associated to the axial plane with errors $< 0.1\%$, whilst differences over all anti-axial coefficients such as $C_{12}^{hom}, C_{66}^{hom}$.

To assess the high error percentage obtained from (4.1) shown on the non-axial related coefficients within the 2-dimensional domain, its proposed to study a hexagonal type domain following the idealization proposed from [18]. In this sense, it's expected corrections over the cell-problems that could contribute to such assumption.

In the following, it will be considered a 2-dimensional hexagonal polygon domain with porosity inclusion of circular type. As before, simulations are done using the same solver proposed for the square case, the linear system derived from the governing system (4.1) is solved preconditioned using an iterative solver.

Figure (4.3) describe the predictions results for the diagonal coefficients in this case by

Homogenized Coefficients				
Error [%]	$\phi = 5\%$	$\phi = 10\%$	$\phi = 15\%$	$\phi = 20\%$
C_{22}^{hom}	0.6 %	1.3 %	1.3 %	1.5 %
C_{33}^{hom}	<0.1 %	<0.1 %	<0.1 %	<0.1 %
C_{55}^{hom}	<0.1 %	<0.1 %	<0.1 %	<0.1 %
C_{66}^{hom}	1.4 %	3.3 %	6.3 %	9.0 %
C_{12}^{hom}	<0.8 %	1.5 %	3.3 %	5.9 %
C_{23}^{hom}	0.4 %	<0.1 %	0.3 %	1.0 %

Table 4.1: Percentage errors of the homogenized coefficient with respect to the PG reference case. The tensors are written in *Voigt* notation and microstructure is defined by a 2-dimensional unitary square with periodic perforation as porosity as shown schematically in (1.4).

the FEM method, compared to the reference results. It shows a clear prediction on the two main diagonal coefficients, being the isotropic values with percentage errors $< 1\%$, thus a best prediction in this cases. Similarly, figure (4.4) shows the non-diagonal elastic coefficients

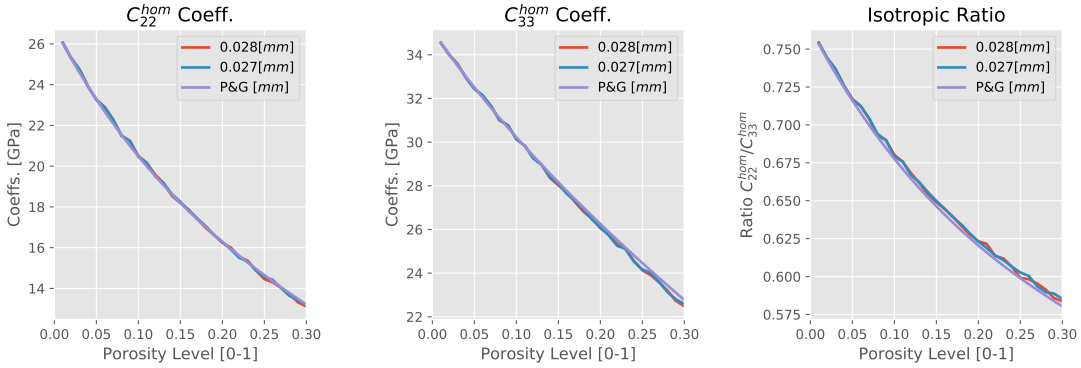

Figure 4.3: Main diagonal elastic tensor coefficients in *Voigt* notation. The figure shows the prediction values over the range $(1, 30)[\%]$ of porosities with characteristic microstructure defined by an hexagonal 2-dimensional polygon. The blue, orange lines describe the FEM predictions at different mesh sizes, whereas the green line describes the PG approximation.

describing shear behavior comparing again to (PG) approximations. The coefficients connected to the axial-plane shows predictions with errors $< 2\%$, therefore validated under the clinical range, whereas the problematic prediction of the C_{66}^{hom} coefficient persist as in the case before and moreover, the errors become $> 15\%$ at bigger porosity values.

As before, the prediction failure is related to the boundary conditions being imposed on the domain, and the continuity conditions over the mesh. The instability effects obtained, shows a clear dependence on the mesh size, thus further studies must be done. Finally, the explicit results of percentage errors are shown in the table (4.2). It describes the clear correspondence between elastic homogenized coefficients with axial connection, and the error prediction on the C_{66}^{hom} which is attributed to a full non-axial behavior, not captured within the 2-dimensional microstructure assumption.

From tables (4.1), (4.2) it can be concluded that the 2-dimensional axial type description

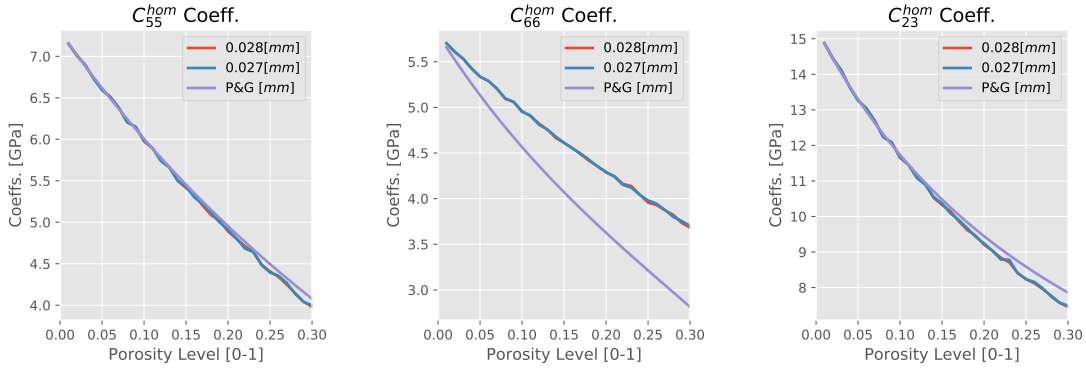

Figure 4.4: Shear type elastic homogenized coeffs. in *Voigt* notation. The figure shows the behavior over the range $(1, 30)[\%]$ porosity with characteristic microstructure described by a hexagonal 2-dimensional polygon.

Homogenized Coefficients				
Error [%]	$\phi = 5\%$	$\phi = 10\%$	$\phi = 15\%$	$\phi = 20\%$
C_{22}^{hom}	<0.1 %	<0.1 %	<0.1 %	0.3 %
C_{33}^{hom}	0.2 %	0.3 %	0.1 %	0.7 %
C_{55}^{hom}	0.3 %	0.5 %	0.1 %	1.2 %
C_{66}^{hom}	4.0 &	8.6 %	13.2 %	18.2 %
C_{12}^{hom}	0.7 %	2.1 %	4.4 %	7.2 %
C_{23}^{hom}	0.2 %	0.7 %	1.4 %	2.5 %

Table 4.2: Percentage errors between the homogenized coefficients and the PG reference case. The tensors are expressed in *Voigt* notation with microstructure defined as a hexagonal polygon with circular perforation acting as porosity.

of the characteristic periodic microstructure relates correctly to realistic mechanical behavior in bone, nevertheless it lacks of non-axial type description regarding to PG predictions. It related then to a possible failure to incorporate non-axial structures that marginally could affect the homogenized coefficients by means of the two-scale framework. Such effects are currently under study in a experimentally oriented setting [8].

4.1.2 3-Dimensional Model

To test the insight observed using 2-dimensional case and assuming the lower percentage error shown from the unit-square type domain, a 3-dimensional cubic domain with cylindrical type inclusion is proposed as periodic microstructure characteristic of cortical bone, i.e. $\mathbf{Y} = (0, 1)^3$. Such new degree of freedom is expected to contribute on the non-axial behavior, thus incorporating missing elements that are vanished from a lower dimensional description. However, it requires computational cost associated to finer meshes for fidelity results.

The figure (4.5) describes diagonal coefficients by means of FEM method, comparing with PG predictions. Nevertheless, the isotropic ratio predicts a different behavior from the 2-

dimensional models, assumed from the new terms describing multiple axial and anti-axial interaction on the cell PDE system. Similarly, (4.6) describes non-diagonal coefficients that

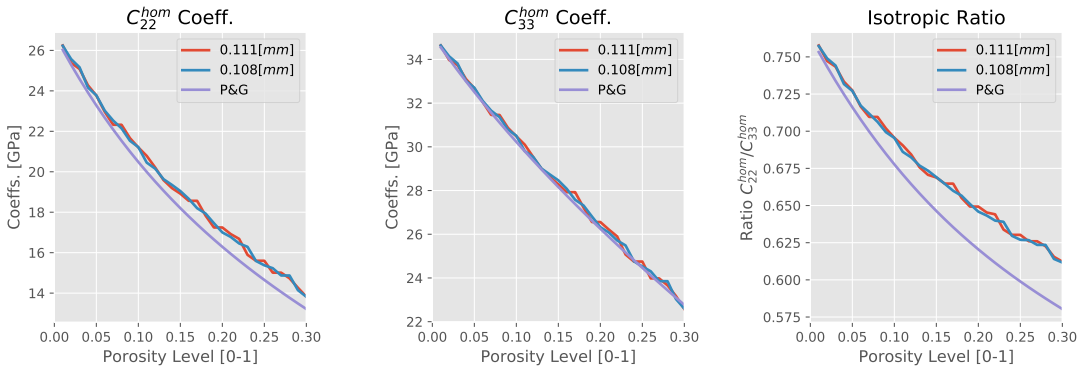

Figure 4.5: Main diagonal elastic tensor coefficients in *Voigt* notation. It describes prediction values over the range $(1, 30)[\%]$ of porosities with 3-dimensional cubic characteristic microstructure. The blue, orange lines describe the FEM predictions at different mesh sizes, whereas the green line describes the PG approximation.

in the 2-dimensional case contains greater error percentages.

As stated before, such behavior assumed as interactions between non-axial and axial behavior as described from $C_{55}^{hom}, C_{23}^{hom}$ coefficients, shows error of $\sim 1\%$ regarding to PG predictions. Thus, such error result close to 2-dimensional models tested before, but it remains with different behavior on the C_{66}^{hom} coefficient.

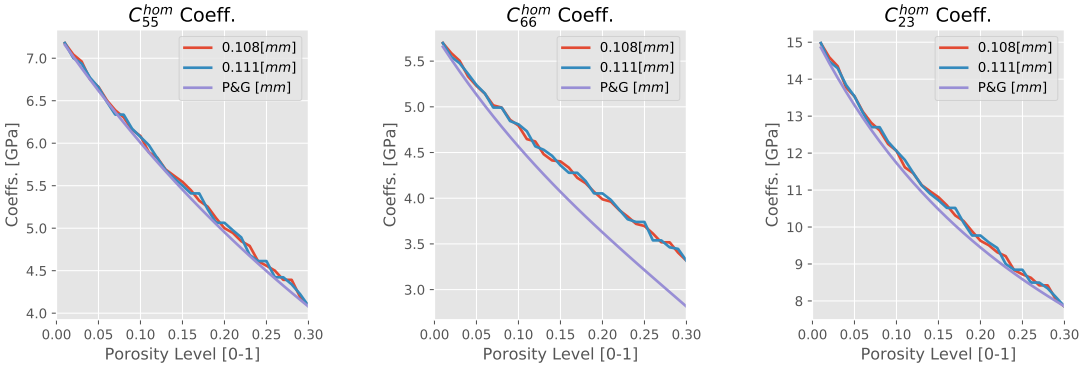

Figure 4.6: Main diagonal elastic tensor coefficients in *Voigt* notation. It describes prediction values over the range $(1, 30)[\%]$ of porosities with 3-dimensional cubic characteristic microstructure. The blue, orange lines describe the FEM predictions at different mesh sizes, whereas the green line describes the PG approximation.

Finally, table (4.3) shows explicitly error percentages obtained at various porosity levels. It can be concluded that diagonal elastic coefficients, describe with lower errors the mechanical behavior following PG asymptotic solutions, as shown by $C_{22}^{hom}, C_{33}^{hom}$.

Similarly, axial interacting coefficients such as $C_{23}^{hom}, C_{55}^{hom}$ follows predicted values regarding the reference which implies correct incorporation of realistic interaction within long

bone axis. Nevertheless, C_{66}^{hom} remains with higher errors of $\sim 10\%$ which enable us to conclude possible underlying effects from produced from the microstructure, having impact on the overall elastic behavior on bone. Such conclusion it backed-up from the validity of PG model, which fits experimental data with C_{66}^{hom} errors of $\sim 9\%$. It can be associated moreover to the presence of *Volksmann* canals that interact on the non-axial plane and that are assumed to have minimal impact on the periodic structure, which might not be fully valid at this scale.

Homogenized Coefficients				
Error [%]	$\phi = 5\%$	$\phi = 10\%$	$\phi = 15\%$	$\phi = 20\%$
C_{22}^{hom}	2.1 %	3.5 %	4.6 %	4.3 %
C_{33}^{hom}	0.5 %	0.9 %	1.0 %	0.2 %
C_{55}^{hom}	0.6 %	1.3 %	1.6 %	0.9 %
C_{66}^{hom}	1.8 %	5.0 %	8.1 %	9.9 %
C_{12}^{hom}	1.4 %	1.7 %	0.9 %	2.1 %
C_{23}^{hom}	1.8 %	2.7 %	3.1 %	1.9 %

Table 4.3: Percentage errors between the homogenized coefficients and the PG reference case. The tensors are expressed in *Voigt* notation with 3-dimensional cubic microstructure and cylindrical subdomain describing the porosity.

4.2 2-Dimensional Simulations of Wave Propagation

The simulation setting associated to the experimental measurements is defined by a 2-dimensional rectangular array imitating the frontal plane associated to the cortical bone. In this case, the wave-propagation can be directly compared to the *Lamb*-wave theory proposed by *Rhee* in [20], thus enabling the numerical validation of the modelling being used.

The transducer excitation source is defined at the upper surface where the omit the interaction between the human skin with bone structure itself, mainly of viscous type. The experimental measurement and recording procedure consist in the following steps:

1. Each emission source within a section of the transducer is placed approximately at a distance of $0.5\,[mm]$ from one another, being together a set of 5-12 different sources experimentally. Each one activated independently thus defining unique wave-guide propagation profiles, i.e., characterized by (porosity, thickness) pair. The numerical implementation uses data recording reconstructing 8 sources, allowing greater singular value fidelity for comparison, thus containing the standard experimental setting.
2. The detection is obtained by placing typically 12-24 sensors depending on the configuration used, where each one is placed at a distance approximately of $0.4\,[mm]$ from one another. In particular, the choice is made regarding the single source or multiple source setting used, with 48 and 66 sensors respectively.

Each force source acting at the surface is modeled on the vertical direction associated to the horizontal plane of the skin pointing to the mid section of the cortical bone with a central

time $t_0 > 0$ and angular frequency $f_0 > 0$, i.e., described in the form:

$$\mathbf{F}(\mathbf{x}, t) = -\mathrm{e}^{\frac{(t-t_0)^2}{2\sigma^2}} cos(2\pi(t - t_0)f_0)\mathbb{I}_{\mathbf{x}\in\Gamma_u}\hat{j} \quad \text{on } \Gamma_N \tag{4.2}$$

where $\Gamma_u \subset \Gamma_N$ denotes a subset of the boundaries where the force is applied, being the subscript denoting the upper one (u). Figure (4.7) shows the explicit form used. In both time and frequency domain simulations, the parameters on the input force are set to $t_0 = 1, \sigma_0 = 0.7, f_0 = 1$. An important aspect shown on the singular value decomposition will be the correspondence between the input force type used and the recorded signal, in particular regarding to the real part of the Fourier transformed input force.

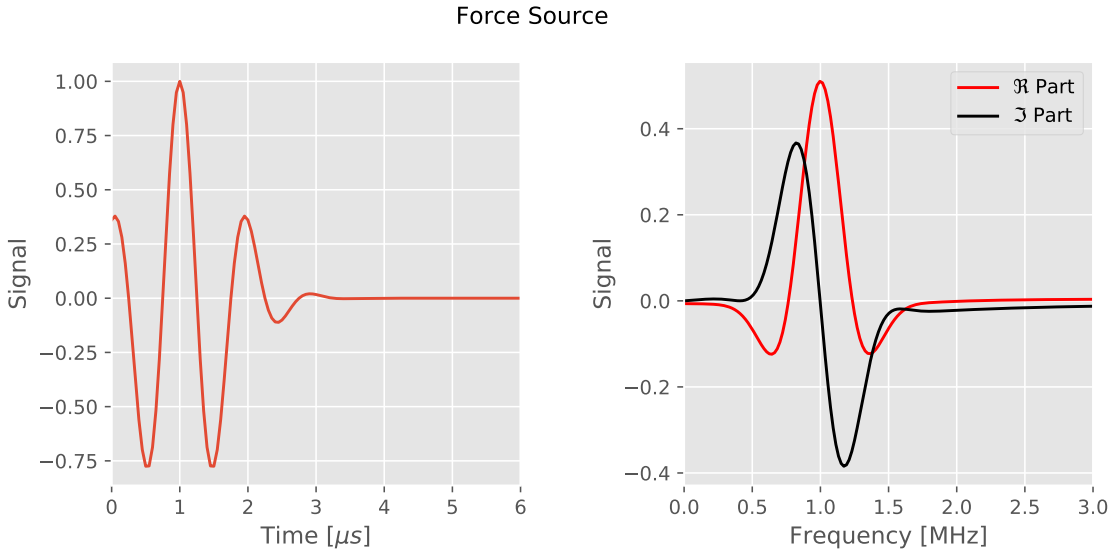

Figure 4.7: On the left side, the input force in time domain while on the right side the input force in frequency domain. The implementation is done using $t_0 = 1[\mu s], \sigma_0 = 0.7[\mu s], f_0 = 1[Mhz]$

Formally the PDE system simulated is defined by finding the solution of (4.3) under the β-Newmark (3.2.1) time scheme with parameters $\beta = 0.36$ and $\gamma = 0.7$.

$$\begin{cases} \rho^0 \partial_{tt} u^{(0)} - \nabla \cdot \sigma^0(u^{(0)}) = \mathbf{0} & \text{in } (0,T) \times \Omega \\ \sigma^0_{ij}(u^{(0)}) = C^{hom}_{ijkl} \mathbf{e}_{kl,x}(u^{(0)}) & \text{in } (0,T) \times \Omega \\ u^{(0)} = \mathbf{0} & \text{on } (0,T) \times \Gamma_l \cup \Gamma_r \\ \sigma^0(u^{(0)}) \cdot n = \mathbf{F}(\mathbf{x}) & \text{on } (0,T) \times \Gamma_u \cup \Gamma_\mathrm{d} \end{cases} \tag{4.3}$$

Over such kind of configuration it can be proved theoretically the existence of the so-called *Lamb*-waves that describe the particular guided-wave propagation associated to the elastic coefficients and density of the model being used. In particular, the presence of a closed domain implies reflection with different directions related to the *Neumann* or *Dirichlet* respectively.

From a computational points of view, its observed the dependence of the mesh discretization with respect to the inverse problem prediction, thus inducing greater computational costs for fidelity prediction. Given such restriction, the 2-dimensional model had the following characteristics:

1. A rectangular tetrahedral meshed domain using `CGALs` library. With tetrahedral cells at optimal mean diameters of $\sim 20[\mu m]$ used for one-source type simulations and $\sim 40[\mu m]$ for multiple-source simulations. For a reference mesh, number of points used where ~ 30.000 being the triangle cells ~ 60.000 at $40[\mu m]$ and ~ 90.000 points with ~ 300.000 cells at $20[\mu m]$.
2. Its simulated the homogenized elastodynamic model for sets of (th, po) pairs, evaluating then the prediction from the inverse problem solution. The elasticity tensor is of transverse isotropy type, with values obtained from PG predictions since as shown before, there is a correspondence between the FEM simulated coefficients and ones from PG predictions.
3. The recording from the wave-front propagation is done by point measurements from which is then applied a signal processing step to recover *Lamb*-modes diagrams in the form of (f, k)-diagrams.

The figure (4.8) contains a schematic description of the simulation setting for this 2-dimensional case.

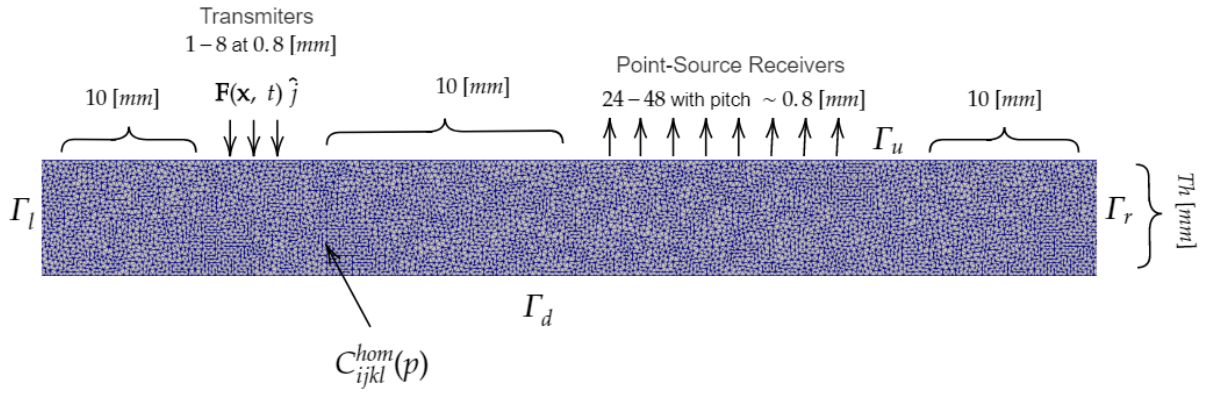

Figure 4.8: Schematic setting of the numerical model to simulate. It contains the *Dirichlet* and *Neumann* boundary conditions for the elastodynamic problem. The mesh is done using `CGALs` library.

Moreover, figure (4.9) describes an explicit time-step of simulation, it shows in particular the propagated wave-front with their symmetric and anti-symmetric profiles.

4.2.1 Case of Multiple Sources

Its simulated under the setting of 8 force sources activated independently, i.e., one at each experimental simulation, thus defining 8 different wave-guided propagation of the model (4.3).

Remark The computation times associated to the multiple-cases setting vary according to the thickness parameter, since it defines the mesh size. Using a test size of $40\,[\mu m]$ for the diameter of the cells within the mesh, the simulation times for different cases varies between $\sim 16 - 28$ hrs in the range of thicknesses $1 - 3\,[mm]$. Moreover, it is found experimentally

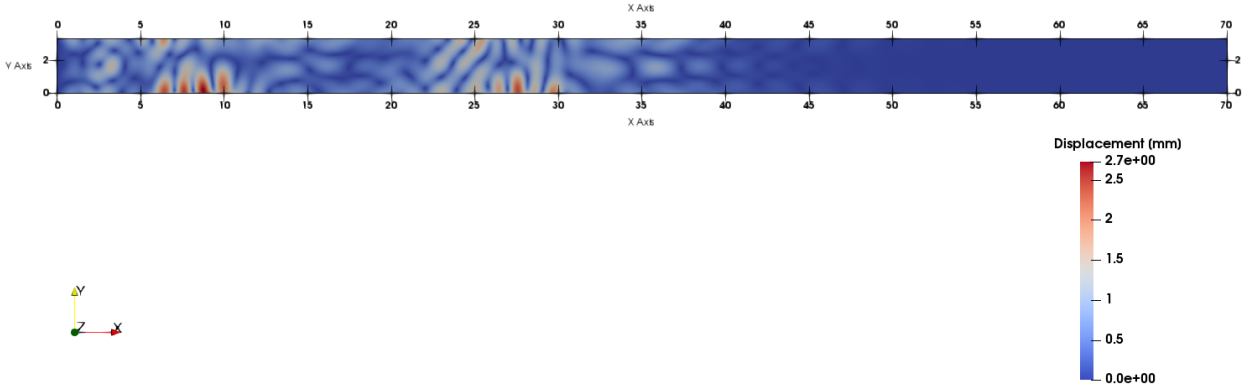

Figure 4.9: Simulated wave-guide stopped at time $31[\mu s]$. It shows in colors the intensity of the propagation wave along the rectangular domain and the interaction with the mixed boundary conditions imposed. This case is parametrized by $(6\%, 3.3[mm])$ porosity-thickness pair.

a quadratic time increment depending on the mesh size, for which a testing case at $20[\mu m]$ takes $\sim 5-7$ days under 1 core of a Xeon E5-2660 v2 processor with 4 Gb. DRR3 RAM. Therefore it was necessary to consider particular properties of the wave propagation to reduce the computational times for each simulation.

The figure (4.10) describes the *Lamb*-curves obtained from the numerically simulated (f,k)-diagram describing the $L_M(f,k)$ functional at different M values, being typically the case $M=4$ used in experimental settings. It shows the validation of the implemented model with respect to the theoretical prediction curves, observing clear correspondence between symmetrical and anti-symmetrical modes.

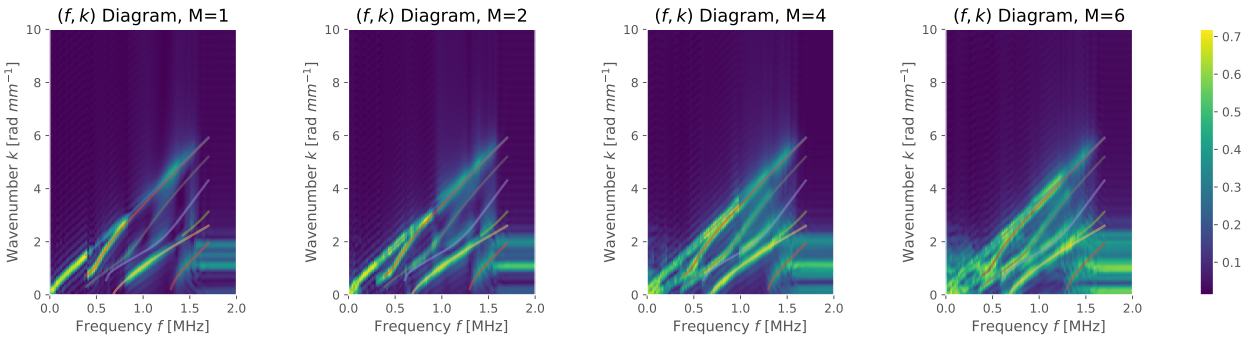

Figure 4.10: Numerically simulated (f,k)-diagram defined by the function $L_M(f,k)$ of a 2D transverse elastodynamic model. Setting of 8 sources with 3% porosity and thickness of $2.8[mm]$ with different number of modes $M>0$.

Similarly (4.11) describes the modes in [dB] from the singular value decomposition of the recorded array. It shows the preponderance of the first three modes describing the wave-front that compared naturally to the experimental reference literature. The peak is shown to be at 0.5[Mhz] in clear correlation with the input force peak shown on figure (4.7). Moreover, the width of the recorded signal varies describing interactions of the wave-front within the mesh.

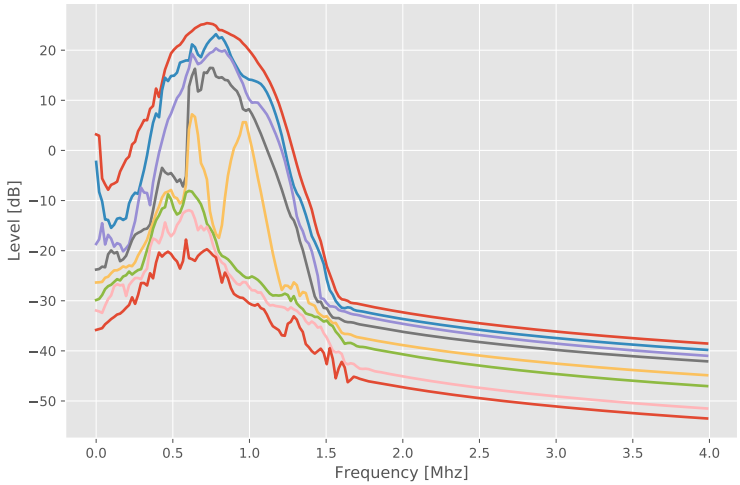

Figure 4.11: Singular values obtained by the SVD decomposition of the recorded signal from the simulated diagram (4.10). It can be seen 8 different curves associated to each force source.

Remark The presence of several symmetric and anti-symmetric modes expressed by the *Lamb* waves is related experimentally with higher thickness values, since in this case the range of horizontal propagation is bigger.

4.2.2 Case of a Single Source

The above study of simulations with 8-source force to generate one sample of data introduce problems of computation under limited resources and time. To tackle such problems, it is used the space invariance of the elastic wave, since essentially, the excitation produced by a particular force-source defines a wave-front that propagates throughout the receivers varying only the position of each one of the 8 input forces, thus the recording generated from each one are defined by spatial translation of the wave-front. Therefore by the homogeneity and symmetry of the domain being used nad the parameter independence of the domain, the 8-source setting can be exchanged to a one-source force with a higher number of receivers. This setting produces a decrease of time require to generate a full simulation, explicitly decreasing to 1/8 of the initial time but introducing reflection effects from the boundary conditions that affect the wave-front.

Remark In this setting of one-source force, it is simulated for the mesh with cell diameters of $\sim 20\,[\mu m]$ describing high-fidelity results with respect to the inverse problem prediction. The simulation times range with respect to the mesh thickness, in which under 1 core of a

Xeon E5-2660 v2 processor with 4 Gb. DRR3 RAM, it requires $\sim 18-26$ hrs. to describe a full simulation using 1024 time step associated to $51.2[\mu s]$ of real-time experimentation.

It is shown on figure (4.12) the (f,k)-diagram associated to the 1-source simulations from such setting described above. It presents natural reflections related to the rectangular 2-dimensional domain with mixed boundary conditions used.

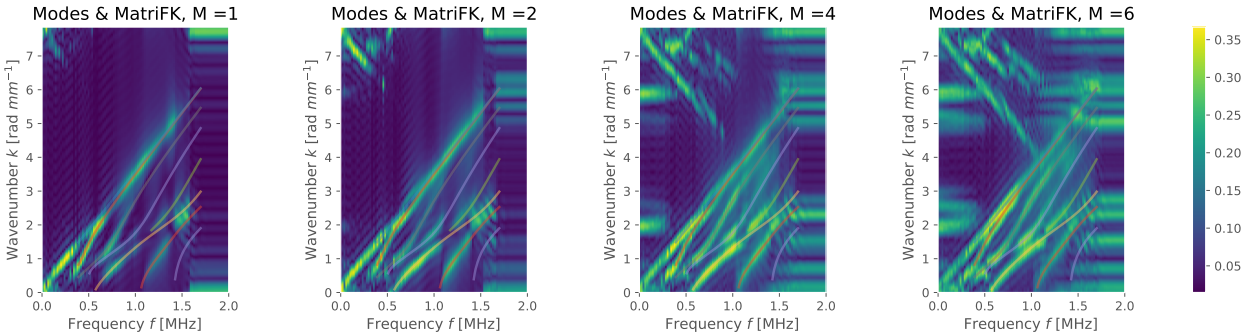

Figure 4.12: Numerically simulated (f,k)-diagram defined by the $L_M(f,k)$ functional of a 2D transverse elastodynamic model. Setting of 1 source with 6% porosity and thickness of $3.3[mm]$ with different M values.

Moreover, figure (4.13) describes the main modes associated to the recorded signal, following a realistic order of magnitude and oscillatory sine-like form characteristic from the input signal being used.

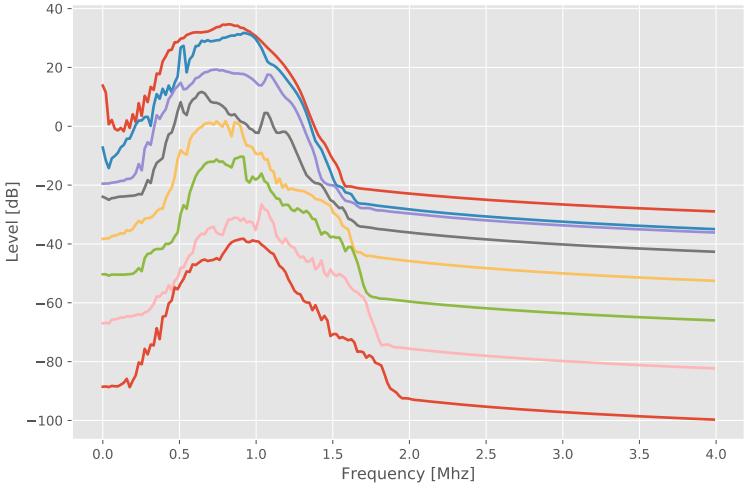

Figure 4.13: Singular values obtained by the SVD decomposition of the recorded signal from the simulated diagram (4.12), describing the 8 simulated recording at the receptors.

The reflections shown in the image (4.13) produced from the simulations corresponds to an aliasing effect in the input signal $S_m(f,\mathbf{x})_{m\in[N^E]}$ in frequency domain at fixed frequency $f\in\mathbb{R}_+$ and receiver location $\mathbf{x}$. Such aliasing express the folding of the k-variable [3] by the

[3] Associated to the wavenumber description in ultrasound jargon.

conjugation property on FFT, i.e.,

$$\overline{\texttt{FFT}(S_m(f,\mathbf{x}))(k)} := \sum_{m=0}^{M} S_m(f,\mathbf{x})\overline{e^{-2\pi i\frac{pk}{M}}} = \texttt{FFT}(S_m(f,\mathbf{x}))(-k)$$

in such a way that the norm associated is the same. Moreover since we consider a finite interval $[0, k_{max}]$, such a reflected wavenumber k is given by $k_{max} - k$ as observed in the figure (4.12)

Given such a symmetry, its considered the application of the analytic projector defined for a given signal S regular enough by:

$$\mathcal{P}(S) := (I + \mathbf{i}\mathcal{H})(S)$$

being $\mathcal{H}$ the Hilbert transform. Such a projector defines the analytic signal of S by constructing its real and imaginary parts.

Since the behavior observed in the (f, k)-diagram (4.12) shows symmetry with bigger values of M, a natural idea is to use the *Hilbert* transform on the input signal, obtaining a analytic signal which maintains the structure of the *Lamb* modes and moreover recreates experimentally obtained results *in-vivo* and *ex-vivo*. Applying then such a projection filter we obtain the results qualitatively and quantitatively similar with respect to the real experimental data.

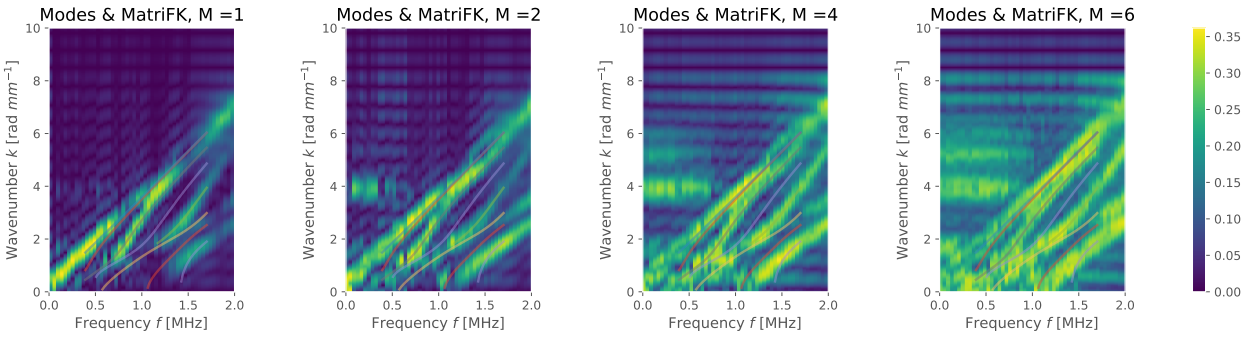

Figure 4.14: Numerically simulated (f, k)-diagram of 2D elastodynamic Model. Setting of 1 source with 6% porosity and thickness of 3.3$[mm]$ applying Hilbert transform to delete reflections.

To give statistical results, using uniformly distributed pairs in the parameters space of biomedical interest it is simulated under the above setting, obtaining the following results in terms of Root Mean Square Error (RMSE), validating the model used and the simulations being done.

A critical aspect regarding the experimental procedure is defined by the device sensitivity towards axial measurements. It has been observed that small variations of the device alignment implies corrupted recording that produce therefore wrong (porosity, thickness) prediction pairs. In this sense, table (4.4) shows explicitly the direction-sensibility dependence towards the recordings. As Axial and Anti-axial measurement itself retrieve RMSE lower enough in biomechanical settings, the compose recordings of data, retrieve porosity

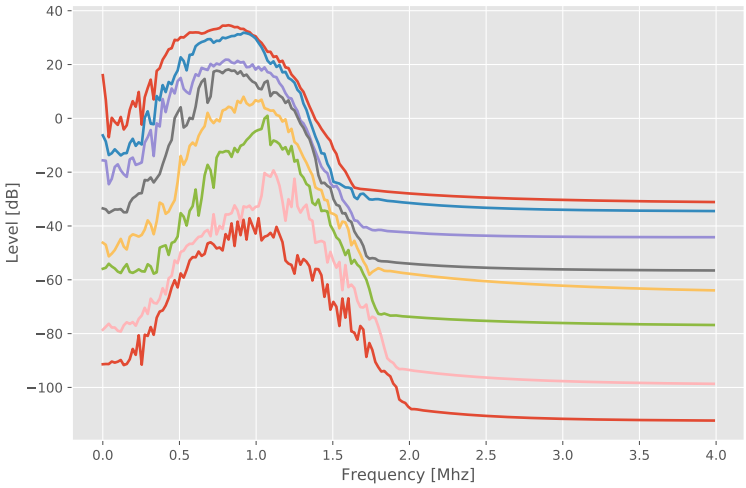

Figure 4.15: Singular values obtained by the SVD decomposition of the recorded signal from the simulation (4.14), describing the 8 different recordings at the receptors.

RMSE	**Porosity** (0-30 %)	**Thickness** (1-4) [mm]
Axial Meas.	0.87 %	0,02 [mm]
Anti-Axial Meas.	0.47 %	$<$0.01 [mm]
Composed	1.2 %	0.03 [mm]

Table 4.4: RMSE results from time-domain simulations using a set of 8 (porosity, thickness) pairs homogeneously distributed on the space of biomedical interest. Explicitly, the **Axial Meas.** defines vertical measurements of displacement, **Anti-Axial Meas.** defines horizontal measurement of displacement, whereas **Composed** defines measurement of maximum values between each of the two above, thus being of mixed type.

errors order of magnitude higher. Thus, directional data contamination compromise robustness of the inverse problem formulation. Therefore, an aspect that must be considered from the modelling setting as in the experimental device.

4.3 Case on Frequency Domain

The time-domain simulation give results which represent qualitatively the model with enough fidelity, nevertheless such simulation requires relatively small time step in such a way that for full simulations it takes considerable time. Thus, it is necessary to define a model which reduces such computational cost. To this end, let us note that the signal processing involves application of `FFT` over the sensors data, a straightforward method is to consider simulations directly on the frequency array of interest $(\omega_{\mathrm{i}})_{\mathrm{i}\in[N^F]}$.

Explicitly, one seek solutions at fixed frequency $\omega \in \mathbb{R}_+$ in the form:

$$u^{\varepsilon}(\mathbf{x}, t) = \hat{u}^{\varepsilon}(\mathbf{x}, \omega)\mathrm{e}^{\mathrm{i}\omega t} \tag{4.4}$$

solving the effective elastic formulation

$$\begin{cases} -\rho^0\omega^2\hat{u}^{(0)} - \nabla\cdot\sigma^0(\hat{u}^{(0)}) = \mathbf{0} & \text{in } \Omega \\ \sigma^0_{ij}(\hat{u}^{(0)}) = \mathbf{C}^{hom}_{ijkl}\mathbf{e}_{kl}(\hat{u}^{(0)}) & \text{in } \Omega \\ \hat{u}^{(0)} = \mathbf{0} & \text{on } \Gamma_D \\ \sigma^0(\hat{u}^{(0)}(\mathbf{x}))\cdot n = \hat{\mathbf{F}} & \text{on } \Gamma_N \end{cases} \tag{4.5}$$

where it was omitted the frequency dependency on the solution $\hat{u}^{(0)}$ for easiness of exposure and denoted $\hat{\mathbf{F}}(\omega,\mathbf{x})$ the Fourier transform at frequency ω of $\mathbf{F}(\cdot,\mathbf{x})$. Moreover, the numerical implementation is done using FEM on the variational formulation associated to (4.5).

4.3.1 Solutions without Attenuation

Using the frequency domain scheme proposed in the section before, the *Lamb*-waves contained unnatural discontinuities passing from a symmetric mode to an anti-symmetric one, also dB values ranging with over 10 orders of magnitude. Such distortion are shown in (4.16) and (4.17) respectively. This kind of behavior repeated over different pairs of porosity level under study ranging the full domain of biomedical interest associated to the simulations thus becoming an intrinsic aspect of the elastic operator under study.

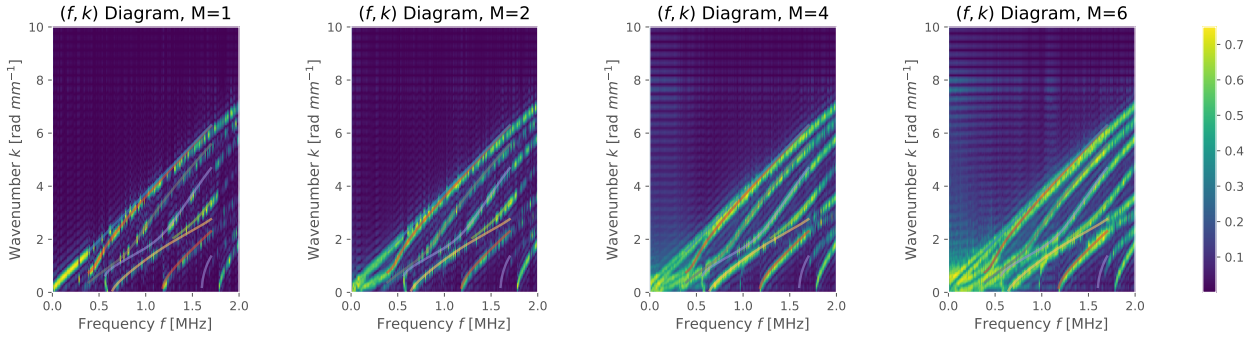

Figure 4.16: Numerically simulated (f,k)-diagram of the $L_M(f,k)$ functional using a 2D frequency domain elastic model. Setting of 8 sources with 12% porosity and thickness of 2.8 $[mm]$

Nevertheless, several sets of simulations are done to study and validate the wave-front generated. The table (4.5) shows the RMSE results where the predictions are done using an optimization algorithm to fit the recorded data to a set of references, i.e., solving the inverse problem [15]. Results shows validation of the frequency domain simulations even with the discontinuities observed both in the (f,k)-diagram as in the multiple peaks observed on (4.17). It can be explained from the clear behavior shown even at high-frequencies, thus enabling a clear fitting of the *Lamb*-curves even with discontinuities of the processed signal.

The presence of discontinuities observed on the curves from the (f,k)-diagram (4.16) as in the peaks shown on (4.17) describes a unnatural behavior of the wave-front. Multiple possible causes can be attributed to such effect, ranging from resonance behavior of the mesh itself, discontinuity effects of the discretization procedure or the bad-possedness of the elastic operator itself.

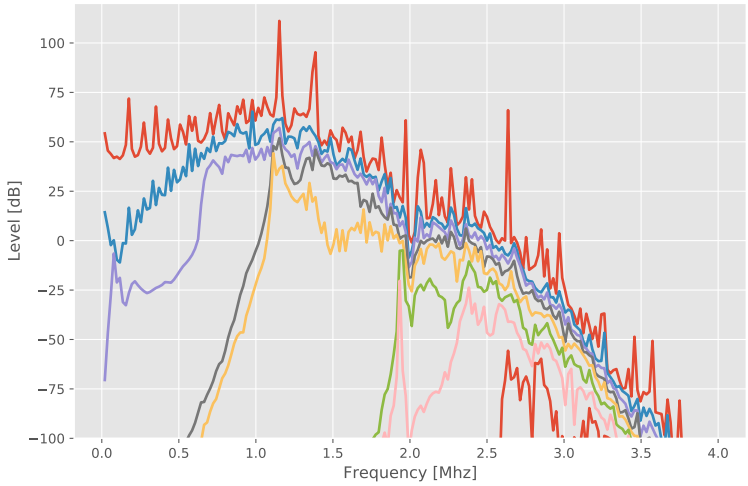

Figure 4.17: Singular values obtained by the SVD decomposition of the recorded signal from the simulation (4.16), describing the 8 different recordings at the receptors containing resonances.

RMSE	**Porosity** (0-30 %)	**Thickness** (1-4) [mm]
Axial Meas.	1.15 %	0,03 [mm]
Anti-Axial Meas.	1,11 %	$<$ 0,01 [mm]
Composed	0.8 %	0.02 [mm]

Table 4.5: RMSE results from frequency-domain simulations using a set of 8 (porosity, thickness) pairs homogeneously distributed on the space of biomedical interest. Explicitly, the **Axial Meas.** defines vertical measurements of displacement, **Anti-Axial Meas.** defines horizontal measurement of displacement, whereas **Composed** defines measurement of maximum values between each of the two above, thus being of mixed type.

In this particular case, let us recall from the justification section, that the existence results of the elastodynamic solution is derived from the existence of an increasing sequence of eigenvalues associated to the elastic operator (2.4). In this context, such eigenvalues will be called eigen-frequencies and they correspond to the main cause of such discontinuities observed before on the simulations as will be studied in what follows.

Such a study corresponds to the formulation of an eigenvalue problem associated to the elastic operator, defined as finding the pairs $\{(\lambda_k, u_k) \,:\, k \in \mathbb{N}\} \subset \mathbb{R}_+ \times \mathbf{H}^1(\Omega, \Gamma_D)$ solution to the following variational form:

$$\mathcal{I}_{\mathbf{C}^{hom}}(u_k, v) = \lambda_k (u_k, v)_\Omega \quad \forall v \in \mathbf{H}^1(\Omega, \Gamma_D)$$

where we identify each eigenvalue to the eigenfrequency $\omega_k = 2\pi f_k$ associated to our problem in the form:

$$\lambda_k = \rho^0 (2\pi f_k)^2, \text{ i.e. } f_k = \frac{1}{2\pi}\sqrt{\frac{\lambda_k}{\rho^0}} \quad k \in \mathbb{N}_*$$

Remark Let us note in particular that the existence of such pairs is obtained from a classical result of elliptic theory [19], [11]. Explicitly, it follows since the homogenized coefficients are elliptic and moreover they are bounded which gives us a well-defined bilinear, bicontinuous and coercive operator $\mathcal{I}_{\mathbf{C}^{hom}}(\cdot,\cdot)$ and a linear continuous operator $b(\cdot) := (u_k, \cdot)$ defined respectively on $\mathbf{H}^1(\Omega, \Gamma_D) \times \mathbf{H}^1(\Omega, \Gamma_D)$ and $\mathbf{H}^1(\Omega, \Gamma_D)$.

By solving the problem (4.3.1), it was found a discrete spectrum with abundant eigen-frequencies in bounded intervals of frequency as predicted from (2.4), nevertheless the experimental frequency array which was necessary to use for further studies in connection with the real data showed a neighborhood of at least eigen eigen-frequencies over each experimentally selected frequency.

In (4.18) is shown the frequencies used in the experimental setting used for the simulations in the frequency domain and the eigen-frequencies associated to the operator under study. It explicitly describes the correspondence of the found eigen-values within a close neighborhood of the simulated frequency array and moreover, intersecting the peaks with resonance modes, thus explaining the resonance and un-natural discontinuity effect observed before.

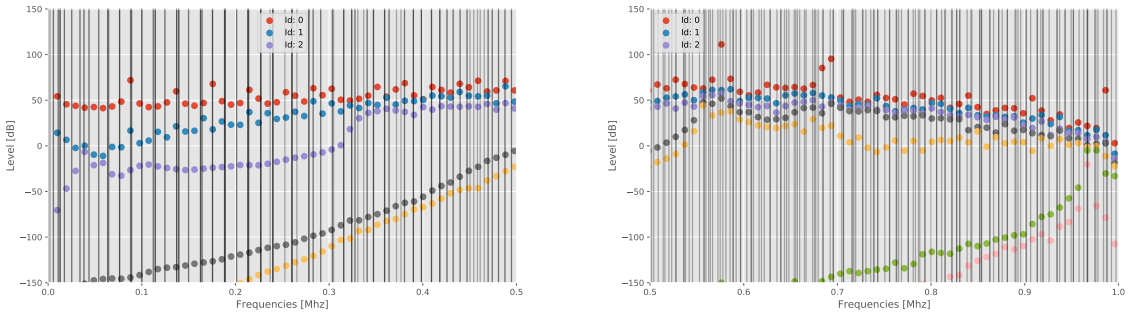

(a) Start Bandwidth

(b) End Bandwith

Figure 4.18: Comparison between Singular Values and Eigen-frequencies: Experimentally its found a increasing sequence of eigenvalues that intersects the experimentally chosen array frequencies.

4.3.2 Solution using Attenuation.

To bypass the oscillation observed at the frequency-domain problem, its considered adding a ε viscous-like term, such model in particular defines a translation of the eigen-frequencies from the elastic operator to the complex plane, thus avoiding the real plane resonances. In this sense, is expected an smoothing effect on the real part recordings, and moreover this implies avoiding the ill-conditioned matrix system from the FEM space discretization procedure.

For a fix frequency $\omega \in \mathbb{R}$, let us consider solutions in the form: $u(\mathbf{x}, t) = \mathrm{e}^{\mathrm{i}\omega t}\hat{u}(\mathbf{x})$, so that

$\hat{u} \in \mathbf{H}^1(\Omega)$ solves the equivalent problem in the frequency domain

$$\begin{cases} -\omega^2 \rho^0 \hat{u} - \mathrm{i}\varepsilon \hat{u} - \nabla \cdot \sigma^0(\hat{u}) = \mathbf{0} & \text{in } \Omega \\ \sigma^0(\hat{u}) = C^{hom}_{\mathrm{ijkl}} \mathbf{e}_{kl}(\hat{u}) & \text{in } \Omega \\ \hat{u} = \mathbf{0} & \text{on } \Gamma_D \\ \sigma^0(\hat{u}) \cdot n = \mathbf{F}(\cdot, \omega) & \text{on } \Gamma_N \end{cases}$$

Taking into account that `FEniCS` version 2017.2.0 doesn't support the usage of a complex coefficient formulation in the variational form, its decomposed the solution in their real and complex part as $\hat{u} = \hat{u}_R + \mathrm{i}\hat{u}_I$. It follow then a coupled system satisfied for the pair $(\hat{u}_R, \hat{u}_I)$ given in the form:

$$\begin{cases} -\omega^2 \rho^0 \hat{u}_R + \omega\varepsilon \hat{u}_I - \nabla \cdot \sigma(\hat{u}_R) = \mathbf{0} & \text{in } \Omega \\ -\omega^2 \rho^0 \hat{u}_I - \omega\varepsilon \hat{u}_R - \nabla \cdot \sigma(\hat{u}_I) = \mathbf{0} & \text{in } \Omega \\ \hat{u}_R, \hat{u}_I = \mathbf{0} & \text{on } \Gamma_D \\ \sigma(\hat{u}_R) \cdot n, \sigma(\hat{u}_I) \cdot n = \hat{\mathbf{F}}_R, \hat{\mathbf{F}}_I & \text{on } \Gamma_N \end{cases}$$

which can be solved with the standard tools of `FEniCS` by the usage of a mixed element for the couple system.

Simulating such system shows on figure (4.19) the (f, k)-diagram associated to the 8-sources setting. It presents natural reflections related to the rectangular 2-dimensional domain used with mixed boundary conditions.

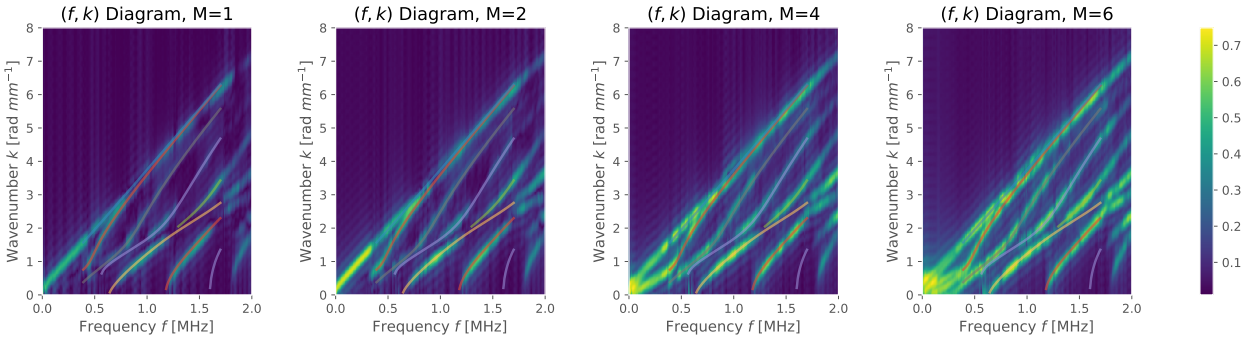

Figure 4.19: Numerically simulated (f, k)-diagram of the $L_M(f, k)$ functional using a 2D transverse elastodynamic model. Setting of 8 sources with 12% porosity and thickness of $2.8[mm]$ with different M values for signal intensity comparison.

Nevertheless, using figure (4.20) of main modes associated to the recorded signal, its observed vanishing oscillation of the modes, thus numerically avoiding the eigen-frequencies, the main provider of resonances.

4.4 3-Dimensional Simulation of Wave Propagation

Following the 2-dimensional case, it is now studied the effect of radial wave behavior on the recorded signal, assessing in particular the experimentally obtained results that neglect the non-axial wave-guide propagation. In this sense, is assessed the wave-propagation by using

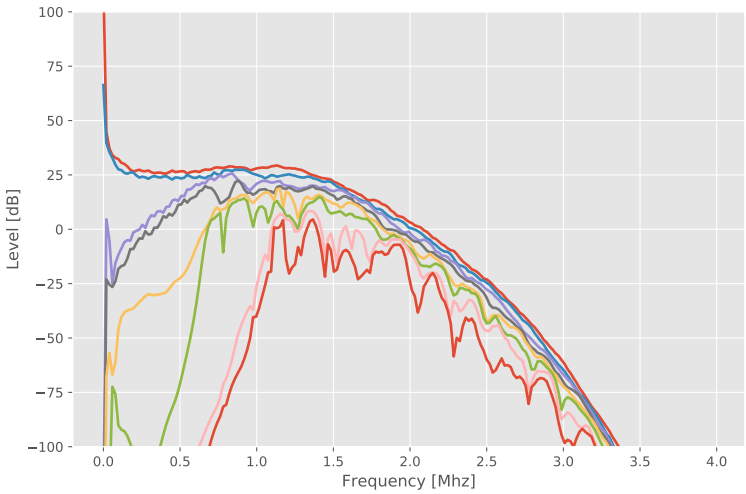

Figure 4.20: Singular values obtained by the SVD decomposition of the recorded signal from the simulation (4.19), describing the 8 recorded attenuated signals.

a cylindrical type domain characterizing the cortex curvature and on a non-uniform domain derived from μ-CT images that relates the irregularities of inner surfaces from realistic cortical bone samples. Such procedures imply the creation of adaptive meshes of the complex cortical bone geometry, where open-source software such as `iso2mesh`, `CGAL` is used for its generation and in particular is created a pipeline of mesh generation from μ-CT images.

4.4.1 Half-Cylinder Case

A half-cylinder mesh is proposed as first approximation to the 3-dimensional real cortical bone sample from the μ-CT images. In this case, avoiding the non-uniformity characteristic of the bone surface it's tested the wave-guide propagation and distortion generated by the natural curvature of the mesh.

The numerical model setting is schematically proposed on (4.21), resembling the 2-dimensional case (4.8) with variations associated to the input force width and rectangular-type force sensors. Such sensors are modelled to capture now surface forces of type $\sigma^{hom}(u) \cdot n$ restricted to each sensor subdomain. As before, the problem is modelled with *Dirichlet* boundary conditions on $\Gamma_l \cup \Gamma_r$ and *Neumann* condition on $\Gamma_u \cup \Gamma_{\mathrm{d}}$.

As before, the implementation is done with `FEniCS` library on time-domain. Applying a post-processing analysis at particular time step with visual behavior effect is shown on figure (4.22) using the `ParaView` library. The figure describes a wave-front propagating along the axial-plane as expected but with characteristic non-axial behavior not present in 2-dimensional simulations.

Remark The total simulation time associated to the half-cylindrical mesh is $\sim$ 25 hrs. using 2 cores on a Xeon E5-2660 v2 processor with 5 Gb. RAM DDR3. This mesh with cells at $\sim 40[\mu m]$ defines *Lamb*-waves requiring 1024 time steps partitioning $51.2[\mu s]$ of real-time

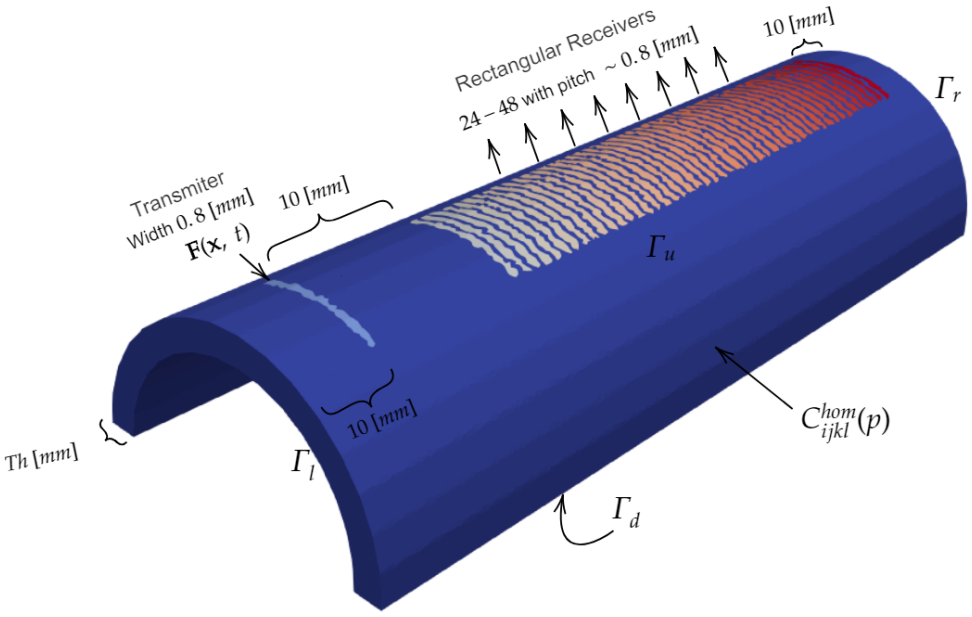

Figure 4.21: Half-Cylinder Mesh defining the geometry for the elastodynamic 1-source simulation with mean diameter of tetrahedral $\sim 40[\mu m]$. Number of vertices: $176,144$ and number of cells: $956,704$. The colors variations shows the different tagged subdomains describing the numerical implementation and recording on the receptors. In this case, from left to right it's shown source subdomain and force-sensors subdomains in array-like form.

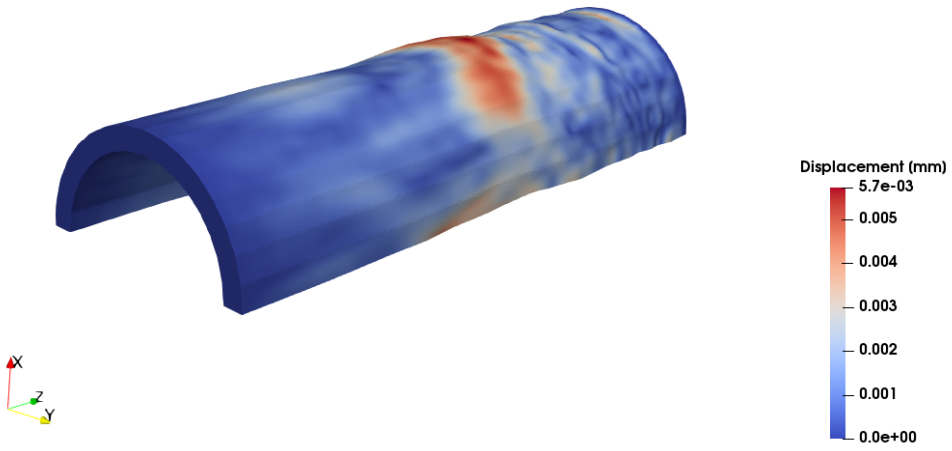

Figure 4.22: Wrapping by vector effect on the simulated domain with input force $\mathbf{F}(\mathbf{x}, t)$ at $8[\mu s]$. The color intensity described by the right-hand side bar shows the magnitude of displacement scaled at $[mm]$.

simulation.

The signal recording from the wave-front propagation partially observed from (4.22) enables us to observe the first example of numerically generated *Lamb*-modes characteristic of the *Lamb*-wave theory as shown in (4.23). In particular, the 3-dimensional curvature effect from the cortical bone doesn't affect the main three modes, nevertheless anti-symmetrical

modes are less clear showing variations respect to the theoretical 2-dimensional theoretical model and vanishing at higher frequencies. On the other hand, symmetrical modes preserve their structure on the central range of frequencies $(0.5, 1.5)[Mhz]$. Moreover, its shown already at level $M = 4$ strong reflection effects affecting the signal. With respect to the sin-

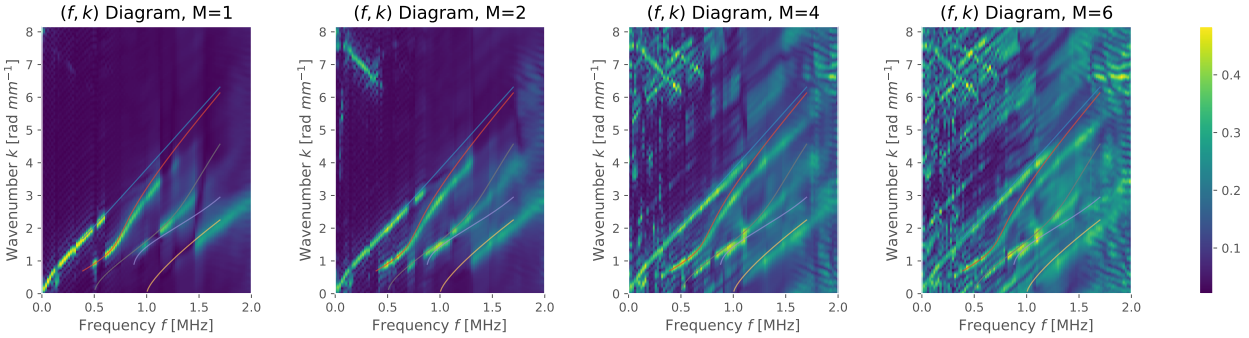

Figure 4.23: Numerically simulated (f, k)-diagram of the $L_M(f, k)$ functional using as 3-dimensional Half-cylinder elastodynamic model. Setting of 1 source with 11% porosity and $1.8\,[mm]$ thickness applying Hilbert transform to delete reflections. The inverse formulation retrieves $\sim 1.01\%$ of porosity and $\sim 1.801\,[mm]$ thickness.

gular value decomposition of the recorded signal, in figure (4.24) the first 3 modes describes a natural behavior in the $(0, 20)\,[\mathrm{d}B]$ range associated to the input force currently used. The oscillatory effect is attributed to the cosine component on the force-source, decaying at outside the maximum signal intensity at $\sim 1\,[MHz]$.

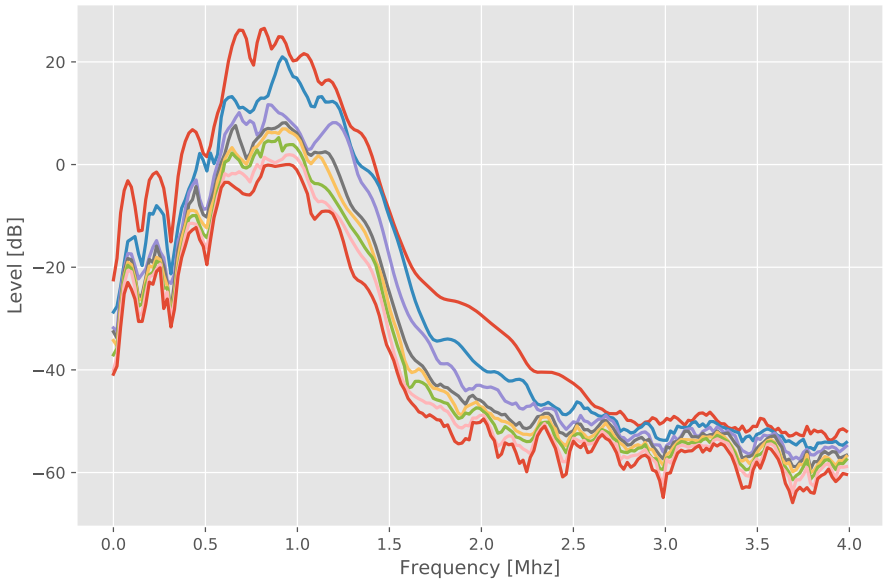

Figure 4.24: Singular values obtained by the SVD decomposition of the recorded signal from the simulation (4.23). The different modes obtained from the decomposition are shown in different colors, being the first 3 related to the naturally obtain from real *ex-vivo* results.

4.4.2 Irregular Domain Case

The half-cylinder shows clear correspondence to the 2-dimensional case, describing prevalence of the axial-propagation over the non-axial effect that occur during the wave-front. Nevertheless, it does not incorporates possible irregularities arising from constant development of bone, being not only the curvature effect relevant to a realistic simulation but also the presence of non-uniform irregularities mainly from the interior surfaces on cortical bone samples. In this case, it is assessed the mesh creation based on real μ-CT cortical bone images and the data-flow necessary to create a well-defined mesh, simulation and processing of results.

Mesh Generation

The mesh generation is done using the data-flow diagram presented in (4.25). Such procedure works by applying several layer of software. It creates a complex tetrahedral mesh from processed volumetric images using as back-end `CGAL` library that compute the geometry. The processing of the μ-CT gray-scale images stack is defined in three main steps:

1. A scaling procedure from input $9\,[\mu m]$ voxel images is done to restrict the memory consumption from the full stack of μ-CT images. The output images are obtained with $56\,[\mu m]$ voxel, i.e., considering a 40% scaling factor with cubic interpolator.
2. The stack is separated between gray-scale value ranges, to isolate the different sets of constituent materials. In this case, the separation of the mesoscale is done, being porosity and bone matrix voxels labeled.
3. Finally, each labeled set of voxels is stacked, defining a volumetric image on `Octave`, meshed with `Iso2mesh` library which wraps functions containing the `CGAL` algorithms of mesh generation.

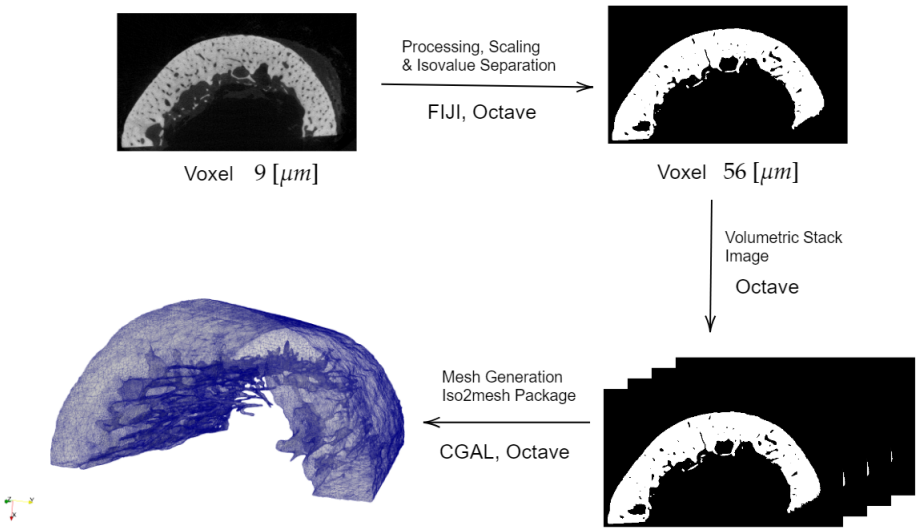

Figure 4.25: Data-Flow. The mesh generation involves a sequence of different software `Fiji, Octave, iso2mesh, CGAL` that used in sequence generates complex adaptive meshes that describe realistic geometries.

The 3-dimensional elastodynamic study of the homogenized bone is done by considering the above mesh generation (4.25) ignoring the labeled sets, thus defining an uniform interior mesh being adaptive to the surface irregularities. To keep the scaled distance relating to the experimental setting, it is used 1000 slices from the stack, thus defining real $56\,[mm]$ of cortical bone geometry.

The objective then is to recover the dispersion curves associated to the 2-dimensional model but now incorporating the surface effect from the curvature and irregularities, that are expected to affect the behavior of the *Lamb*-curves and thus the recorded signal itself.

By applying the generation procedure described before, it follows the realistic irregular mesh pictured in (4.26). It characterizes a cortical bone sample of $56\,[mm]$ length in the long direction describing a thickness of $\sim 1.8[mm]$.

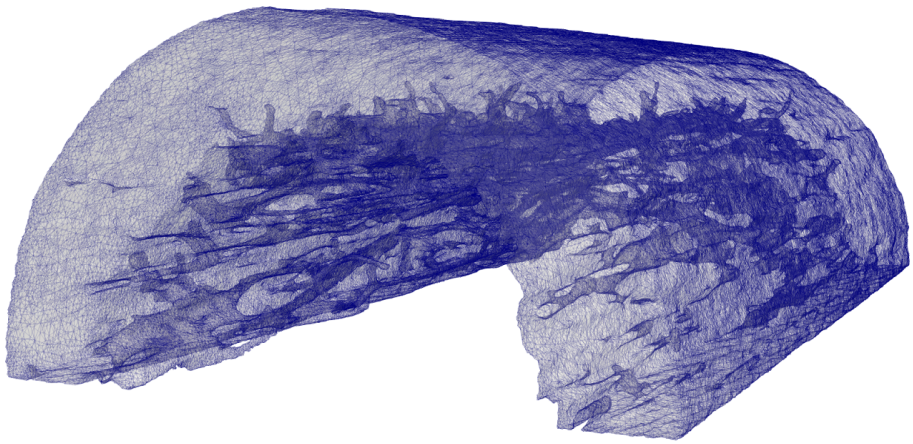

Figure 4.26: Mesh Generated from 1000 Slices from $\mu-CT$ images using the mesh-generation diagram (4.25). It characterizes a cortical bone sample of $56\,[mm]$ length in the long direction associated to a thickness $\sim 1.8[mm]$ and experimentally tested porosity of $\sim 11\%$. Explicitly, the mesh is described by $432,280$ vertices with $1,393,709$ tetrahedrons.

Simulation and Results

The configuration is defined similar to the cylindrical case. The figure (4.27) describes explicitly the settings of rectangular sources and receivers implemented, each one defined by a width of $\sim 0.8[mm]$ with height $\sim 8[mm]$ located at the top surface of the mesh. As in the cylinder case, the receivers record force-signal of type $\sigma^0(u)\cdot n$ over each of the subdomain locations. The adaptive mesh (4.26) resembles a real geometry by meshing the irregularities on the inner surface characteristics of a natural cortical bone sample.

Over such geometry is simulated an elastodynamic model propagating a guided wave and thus generating the dispersion curves of figure (4.29) related to the wavefront in figure (4.28). Varying in color intensity, it is shown the wave-front interacting with the non-uniform mesh. Moreover, different view-planes show direct impact in the wave behavior as it interacts with the inner irregular surface, creating points of high displacement. This kind of behavior not

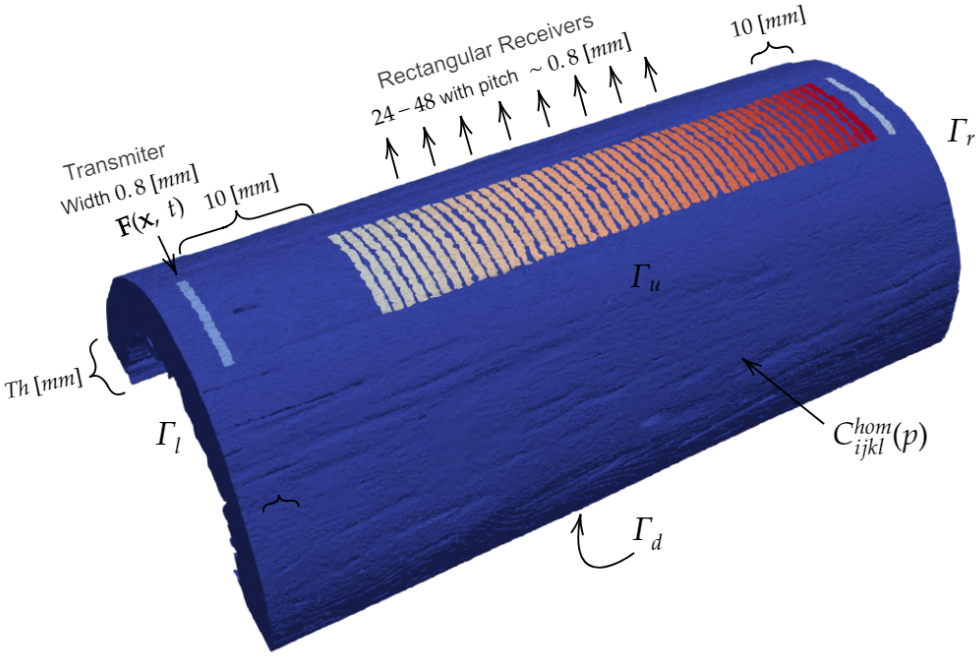

Figure 4.27: The colors markers define the different subdomains associated to the mesh (4.26). It is described 48 receivers and a transmitter locations in a array-like form resembling the experimental transducer. Moreover, each subdomain is defined approximately by ~ 200 marked tetrahedral cells.

observed on the cylindrical case studied before, thus becoming an inherent effect from the irregularities.

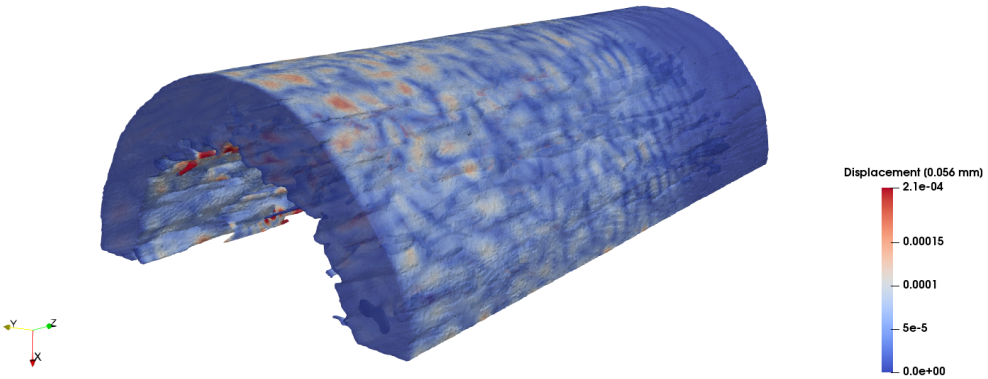

Figure 4.28: The elastodynamic simulation over the irregular mesh is shown at instant $32\,[\mu s]$, characterizing the wave-front propagation using a intensity color-scheme. The right-hand side bar contains the scale over the simulation, at $0.056\,[mm]$ associated to the voxel size.

Remark The elastodynamic model simulated over this complex domain at $\sim 80\,[\mu m]$ required 2 cores of a Xeon E5-2660 v2 processor with ~ 8 Gb of DDR3 RAM and ~ 7 days of computation time. It enables us to obtain complex wave-front propagation affected by the irregularities of the domain.

The effect produced on the guided-wave from the interaction with the irregularities on the domain are shown in the (f, k)-diagram of figure (4.29). It shows a clear discrepancy between the reconstructed modes recorded at the receptors and the reference *Lamb*-curves. The main variation is shown on the first anti-symmetric and symmetric modes, which does not fit within the expected behavior. Nevertheless, it can be seen that second modes have behavior fitting the references. Similarly, singular values associated to data recording described by (4.29) are

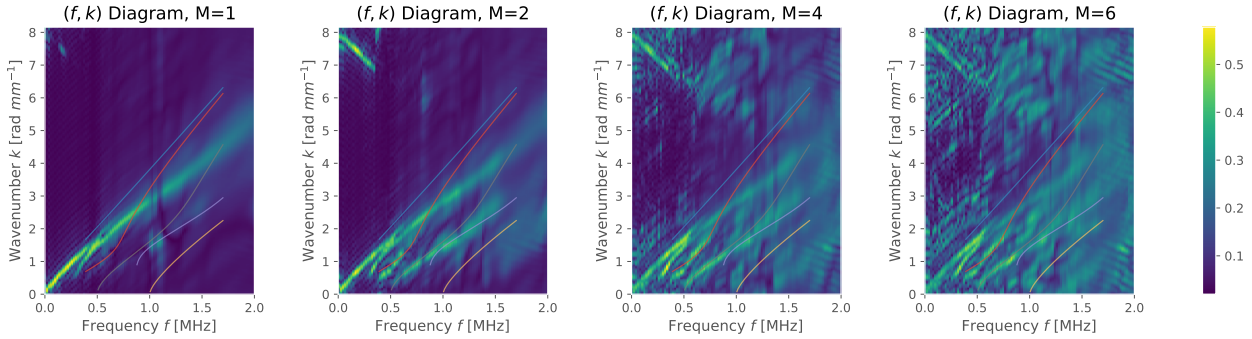

Figure 4.29: Numerically simulated (f, k)-diagram of the $L_M(f, k)$ functional using a 3-dimensional realistic-geometry. Setting of one-source with 11% porosity and $\sim 1.8[mm]$ thickness. The green lines defines *Lamb* curves created from recording of the wave-guide being the others associated to a reference model.

given on (4.30) which resembles realistic values given the input force used. The figure shows the first three modes in realistic magnitude scale $(0, 20)$ [dB], being the rest of modes of lesser importance given the presence of noise in realistic measurements that should vanish the rest of modes. In comparison with the half-cylinder case it's shown a clear variation on the general

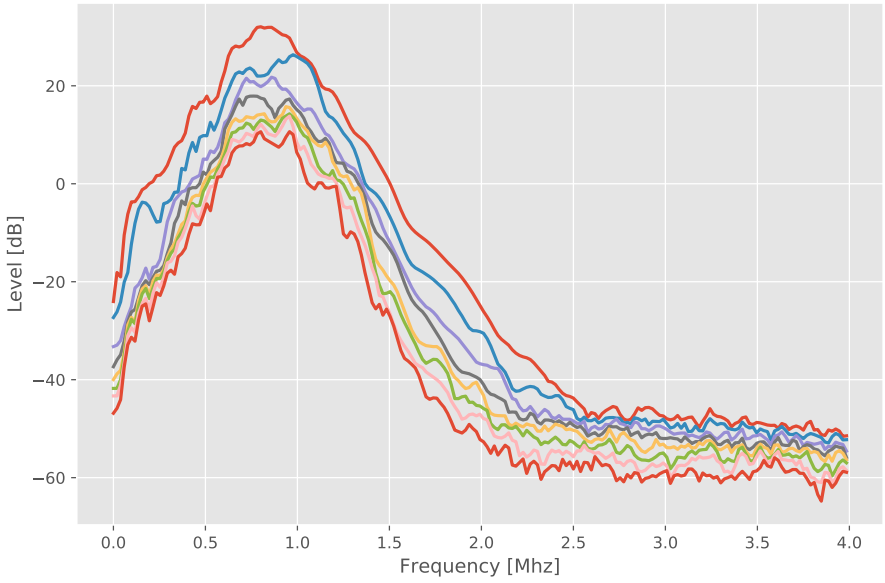

Figure 4.30: Singular values obtained by the SVD decomposition of the recorded signal from the simulated diagram (4.23), describing the 8 recordings at the receptors.

wavefront behavior, expressed in modes not align with respect to the reference cases for the

parameters used in the simulation. Moreover, figure (4.29) shows clear signal distortion at the high frequency range of $(1, 2)\,[Mhz]$ for all the different *Lamb*-curves involved, expressed in color diffusion within the curves. Explicitly, at higher M values, which characterize the amount of receptors information to analyze, shows clear interaction within the domain mesh, thus more error fitting associated to the inverse problem solution.

On the other hand, figure (4.23) associated to the half-cylinder setting describes a more regular behavior of the curves in all the frequency range, corresponding to a wave-front in which the curvature effect does not affect the main axial propagation, thus describing at each M values clear *Lamb*-curves, thus fully comparative signal with the 2-dimensional case.

The explanation to such behavior relates to missing interaction within the inner irregularities that fully deform the characteristic wave propagation. Moreover, the simulations shows concentration of displacement in the interior irregularities being an aspect to further investigate. In this sense, the plausible explanation on the first symmetric and anti-symmetric modes is related to missed damping effects on the bone marrow that are not captured in the simulations, which requires a generalization to a viscoelastic model to capture such effects.

Chapter 5

Viscoelastic Predictions

As explained before, factors of risk fracture such as thickness, porosity and particular quality elements of the extracellular matrix, define the bone quality assessed by DXA techniques and BMD values. The QUS method proposed by *Minonzio and Foiret et al.* [12], [15] of axial transmission technique simulated in the chapter before, is based on recording from the guided-wave propagation over the media, where damping factors naturally affect the signal. This relates to a viscoelastic behavior of the cortical bone arising mainly from the presence of collagen fibers, specifically treated with Resonant Ultrasound Spectroscopy (RUS) techniques. Thus, it becomes natural to study the correspondence between such damping elements and their preponderance on the resulting homogenized coefficients by the two-scale homogenization theory.

Describing the damping effects on cortical bone is not new, *Bernard et al.* [6] studied a viscoelastic-type behavior on a frequency domain, in which he modelled the elastic tensor C^*_{ij} with damping effect described by the formulas:

$$C^*_{ij} = C_{ij} + iC'_{ij} = C_{ij}(1 + iQ^{-1}_{ij}) \quad i, j = 1, \ldots, 6$$

where the Q^{-1}_{ij} are defined as ratios of the imaginary part (C'_{ij}) to the real part (C_{ij}), denoting the so-called quality factors.

In this section, I shall reformulate such quality factors following the two-scale homogenization formalism, recovering the homogenized coefficients in the elastic case at different porosity levels and particularly obtaining prediction for the quality factors at some interval. Using up-to-date references, such coefficients are yet to be validated since there isn't enough experimental literature to confirm nor further validate the predictions.

5.1 Formalization of Q-factors

The quality factors Q_{ij} proposed by *Bernard* in experimental fashion, provide an interesting formalization of the ratio between the real and imaginary constitutive coefficients of a full

viscoelastic mechanical description of the bone, moreover it gives us a comparison using the existent literature and experimental results.

In the following, it is described the so-called Q-factors by means of the two-scale homogenization theory, derived from a *Kelvin-Voigt* viscoelastic formulation of bone in frequency domain. More specifically, the mechanical behavior of bone is assumed as a multiphase viscoelastic material composed of two-phases, defined by a square cell unit on $\mathbf{R}^2$ with circular inclusion in the form $\mathbf{Y} = \mathbf{Y}_m \cup \mathbf{Y}_f$ being each the matrix and fluid parts respectively. For the bone matrix, we associate an elastic behavior defined by the elastic coefficients:

$$C_{ijkl}(\mathbf{y}) = C^m_{ijkl}\mathbb{I}_{\mathbf{Y}_m}(\mathbf{y}) + C^f_{ijkl}\mathbb{I}_{\mathbf{Y}_f}(\mathbf{y})$$

while the porosity is modeled with a viscous contribution, associated to coefficients in the form:

$$D_{ijkl}(\mathbf{y}) = D^m_{ijkl}\mathbb{I}_{\mathbf{Y}_m}(\mathbf{y}) + D^f_{ijkl}\mathbb{I}_{\mathbf{Y}_f}(\mathbf{y}).$$

Moreover, the relations between both behaviors are expressed with attenuation specified by parameters $\alpha^{(m)}, \alpha^{(f)} > 0$ associated to the bone matrix and mesostructure respectively. Explicitly, it is assumed:

$$D^m_{ijkl}(\mathbf{y}) = \alpha^m C^m_{ijkl}(\mathbf{y}), \quad D^f_{ijkl}(\mathbf{y}) = \alpha^f C^f_{ijkl}(\mathbf{y})$$

Remark By assuming this kind of relation, the objective is to obtain a viscoelastic model in which the viscous part is modelled by a linear attenuation of the elastic one, so that the overall behavior is of transverse isotropic type defined by pair of parameters (α^m, α^f) that mimic closely the experimental behavior of cortical bone.

5.1.1 Workflow Description

Given the requirements of a viscous-like behavior, in time domain is considered a model of *Kelvin-Voigt* type with mixed boundary conditions, described in the form:

$$\begin{cases} \rho^\varepsilon \partial_{tt} u^\varepsilon - \nabla \cdot \sigma(u^\varepsilon, \partial_t u^\varepsilon) = \mathbf{0} & \text{in } (0,T)\times\Omega \\ \sigma^\varepsilon(u^\varepsilon, \partial_t u^\varepsilon) = \mathbf{C} : \mathbf{e}(u^\varepsilon) + \mathbf{D} : \mathbf{e}(\partial_t u^\varepsilon) & \text{in } (0,T)\times\Omega \\ \sigma^\varepsilon(u^\varepsilon, \partial_t u^\varepsilon)\cdot n = \mathbf{F} & \text{on } (0,T)\times\Gamma_N \\ u^\varepsilon = \mathbf{0} & \text{on } (0,T)\times\Gamma_D \end{cases}$$

Remark In the above and the next developments, we assume resting initial conditions, i.e., $\partial_t u^\varepsilon = u^\varepsilon = \mathbf{0}$ at $t = 0$, not written explicitly in the models and further deductions.

Existence results can be derived similarly to the elastic case proposed before, by applying spectral decomposition on both: the elastic and viscoelastic operators. Similar mathematical description of viscous models are given by [2], [7] on homogeneous *Dirichlet* boundary condition cases.

The interest is regarded to the frequency-domain, thus applying *Fourier* transform defined at frequency $\omega \in \mathbb{R}$ by assuming $u^\varepsilon(t,\mathbf{x}) = \hat{u}^\varepsilon(\mathbf{x})\mathrm{e}^{\mathrm{i}\omega t}$ it follows the redefined problem in Fourier

domain:

$$\begin{cases} -\omega^2\rho^\varepsilon\hat{u}^\varepsilon - \nabla\cdot\hat{\sigma}_{\varepsilon,\omega}(\hat{u}^\varepsilon) = \mathbf{0} & \text{in } \Omega \\ \hat{\sigma}^\varepsilon(\hat{u}^\varepsilon) = (\mathbf{C} + \mathrm{i}\omega\mathbf{D}) : \mathbf{e}(\hat{u}^\varepsilon) & \text{in } \Omega \\ \hat{\sigma}^\varepsilon(\hat{u}^\varepsilon)\cdot n = \hat{\mathbf{F}}(\omega) & \text{on } \Gamma_N \\ \hat{u}^\varepsilon = \mathbf{0} & \text{on } \Gamma_D \end{cases}$$

such that at $\omega = 0$ we have $\hat{u}^\varepsilon = \mathbf{0}$ at Ω. In particular, for easiness of exposure, it has been omitted dependencies on the frequency for the multiscale solution u^ε.
Now, by the homogenization heuristic using the two-scale asymptotic method, it follows the effective (macroscopic) model defined at frequency ω in the form:

$$\begin{cases} -\omega^2\rho^0\hat{u}^0 - \nabla\cdot\hat{\sigma}^0(\hat{u}^0) = \mathbf{0} & \text{in } \Omega \\ \hat{\sigma}^0(\hat{u}^0) = (\mathbf{C} + \mathrm{i}\omega\mathbf{D})^{hom} : \mathbf{e}(\hat{u}^0) & \text{in } \Omega \\ \hat{\sigma}^0(\hat{u}^0)\cdot n = \hat{\mathbf{F}}(\omega) & \text{on } \Gamma_N \\ \hat{u}^0 = \mathbf{0} & \text{on } \Gamma_D \end{cases}$$

In particular, the homogenized coefficients are defined by the cell problem solutions $\mathbf{N}^{rs} \in \mathbf{H}^1_0(\mathbf{Y}, \mathbb{C})$, described for each $r, s \in \{1, 2, 3\}$ in the form

$$\begin{cases} \partial_{y_j}\big[\big(C_{\mathrm{i}jkl} + \mathrm{i}\omega D_{\mathrm{i}jkl}\big)\mathbf{e}_{kl}(\mathbf{N}^{rs})\big] & = -\partial_{y_j}\big[C_{\mathrm{i}jkl} + \mathrm{i}\omega D_{\mathrm{i}jkl}\big] \quad \forall y \in \mathbf{Y} \\ \big\langle \mathbf{N}^{rs}\big\rangle_{\mathbf{Y}} = \mathbf{0} \end{cases}$$

Since the cell problems must be valid for each $\omega \in \mathbb{R}$ and for each $\mathbf{y} \in \mathbf{Y}$, a natural procedure would be to decouple the cell PDE problems thus being able the define viscosity-elasticity ratios, i.e. an expression to the so-called Q-factors.

The decoupling is then defined by considering the separation between real and imaginary parts associated to the cell solutions, i.e., by considering the following decomposition

$$\mathbf{N}^{rs}(\mathbf{y}) = \mathbf{N}^{rs}_R(\mathbf{y}) + \mathrm{i}\mathbf{N}^{rs}_I(\mathbf{y})$$

being now the vectors functions $\mathbf{N}^{rs}_R, \mathbf{N}^{rs}_I$ in $\mathbf{H}^1_0(\mathbf{Y}, \mathbb{R})$ solving the following PDE coupled system for each real and imaginary solution parts in the form:

$$\begin{cases} \partial_{y_j}\big[C_{\mathrm{i}jkl}\mathbf{e}_{kl}(\mathbf{N}^{rs}_R) - \omega D_{\mathrm{i}jkl}\mathbf{e}_{kl}(\mathbf{N}^{rs}_I)\big] = -\partial_{y_j}\big[C_{\mathrm{i}jrs}\big] & \forall \mathbf{y} \in \mathbf{Y} \\ \partial_{y_j}\big[C_{\mathrm{i}jkl}\mathbf{e}_{kl}(\mathbf{N}^{rs}_I) + \omega D_{\mathrm{i}jkl}\mathbf{e}_{kl}(\mathbf{N}^{rs}_R)\big] = -\partial_{y_j}\big[\omega D_{\mathrm{i}jrs}\big] & \forall \mathbf{y} \in \mathbf{Y} \\ \big\langle \mathbf{N}^{rs}_R\big\rangle_{\mathbf{Y}} = \mathbf{0} \quad \big\langle \mathbf{N}^{rs}_I\big\rangle_{\mathbf{Y}} = \mathbf{0}. \end{cases}$$

Remark Note that for the above cell problems, the existence and uniqueness of a weak solution is guaranteed since the problem can be rewritten as a fully elliptic operator, being the solution unique by applying a normalization condition of mean equal $\mathbf{0}$ type.

With the solution to the cell problem, we can then define the homogenized coefficients associated to the elastic and viscous part by recalling first:

$$\hat{\sigma}^0_{\mathrm{i}j}(\hat{u}^0, \omega) = R^{hom}_{\mathrm{i}jkl}(\omega)\mathbf{e}_{kl}(\hat{u}^0)$$

being the homogenized tensor

$$R^{hom}_{\mathrm{i}jrs} = \big\langle C_{\mathrm{i}jrs} + \mathrm{i}\omega D_{\mathrm{i}jrs} + \big(C_{\mathrm{i}jkl} + \mathrm{i}\omega D_{\mathrm{i}jkl}\mathbf{e}_{kl}(\mathbf{N}^{rs})\big)\big\rangle$$

so that, using the decomposition of N^{rs} it follows the full homogenized expression, described in (5.1) decomposed in real and imaginary parts characterizing the elastic and viscous contribution respectively.

$$\begin{aligned} R^{hom}_{\mathrm{i}jrs} &= \big\langle C_{ijrs} + \big(C_{\mathrm{i}jkl}\mathbf{e}_{kl}(\mathbf{N}^{rs}_R) - \omega D_{ijkl}\mathbf{e}_{kl}(\mathbf{N}^{rs}_I)\big)\big\rangle \\ &\quad + \mathrm{i}\big\langle \omega D_{\mathrm{i}jrs} + \big(C_{\mathrm{i}jkl}\mathbf{e}_{kl}(\mathbf{N}^{rs}_I) + \omega D_{\mathrm{i}jkl}\mathbf{e}_{kl}(\mathbf{N}^{rs}_R)\big)\big\rangle \\ &:= C^{hom}_{\mathrm{i}jrs} + \mathbf{i}\omega D^{hom}_{\mathrm{i}jrs} \end{aligned} \tag{5.1}$$

In particular, the definition of $Q_{\mathrm{i}j}$ factors can be directly rewritten terms of a homogenized formulation, defined directly on the tensor coefficients described by (5.2). In particular, given the deduction done, the definition of such quality-factors becomes dependent on the frequency which derives from the multiscale *Kelvin-Voigt* mechanical model assumed.

$$Q^{-1}_{\mathrm{i}jrs}(\omega) := \frac{D^{hom}_{\mathrm{i}jrs}(\omega)}{C^{hom}_{\mathrm{i}jrs}(\omega)} \tag{5.2}$$

5.1.2 Nonlinear Decomposition

An aspect that must be taken into account is the nonlinear effect added from the asymptotic assumption on the solution, expressed in the term $\mathbf{N}^{rs}$ at the homogenized coefficients definition that can be explicitly stated from (5.2). It is possible to account for that effect by taking a decomposition on the linear part associated to the mean over the coefficient itself and the nonlinear effect produced from the solutions to the cell problems, i.e., from (5.2) the decomposition in their linear and nonlinear effects is obtained as:

$$Q^{-1}_{\mathrm{i}jrs} = \frac{D^{(0)}_{hom}}{C^{(0)}_{hom}} + \frac{1}{C^{(0)}_{hom}\Big(C^{(0)}_{hom} + C^{(1)}_{hom}\Big)}\big[C^{(0)}_{hom}\big(D^{(0)}_{hom} + D^{(1)}_{hom}\big) - D^{(0)}_{hom}\big(C^{(0)}_{hom} + C^{(1)}_{hom}\big)\big] \tag{5.3}$$

where the notation for the linear terms in $p \in [0,1]$ (porosity) in given by:

$$C^{(0)}_{hom} = \langle C_{\mathrm{i}jrs}\rangle_{\mathbf{Y}} \quad D^{(0)}_{hom} = \langle D_{\mathrm{i}jrs}\rangle_{\mathbf{Y}}$$

and the nonlinear terms with respect to $p \in [0,1]$ associated to the solutions N^{rs} is given by:

$$\begin{aligned} C^{(1)}_{hom} &= \quad \langle C_{\mathrm{i}jkl}\mathbf{e}_{kl}(N^{rs}_R) - \omega D_{\mathrm{i}jkl}\mathbf{e}_{kl}(N^{rs}_I)\rangle_{\mathbf{Y}} \\ D^{(1)}_{hom} &= \langle \omega^{-1} C_{\mathrm{i}jkl}\mathbf{e}_{kl}(N^{rs}_I) + D_{\mathrm{i}jkl}\mathbf{e}_{kl}(N^{rs}_R)\rangle_{\mathbf{Y}} \end{aligned}$$

5.2 Predictions

The explicit dependency on the frequency ω, requires us to consider the frequency range in which the experimental setting take place. In this sense, after adjusting regards experimental data range, viscous factors with transverse isotropic behavior of the type are assumed in the form:

$$D^m_{\mathrm{i}jkl}(\mathbf{y}) = 5 \times 10^{-2} C^m_{\mathrm{i}jkl}(\mathbf{y}), \quad D^f_{\mathrm{i}jkl}(\mathbf{y}) = 1 \times 10^{-3} C^f_{\mathrm{i}jkl}(\mathbf{y})$$

Under such considerations, the figure (5.1) contains the prediction for the homogenized elastic coefficients and Q-factors associated to a fixed frequency $\omega = 0,5\,[Mhz]$. It describes the behavior as function of density in the clinical range of interest. The main quality factors describing the axial-related behavior shows predictions comparable to up-to-date literature [6]. Moreover, homogenized elasticity coefficients are recovered with predictions regarding results obtained in fully elastic models [18], therefore describing a generalization. In particular, shear-like $C_{55}^{hom}, C_{66}^{hom}$ coefficients describe experimentally measured values validating the simulated model.

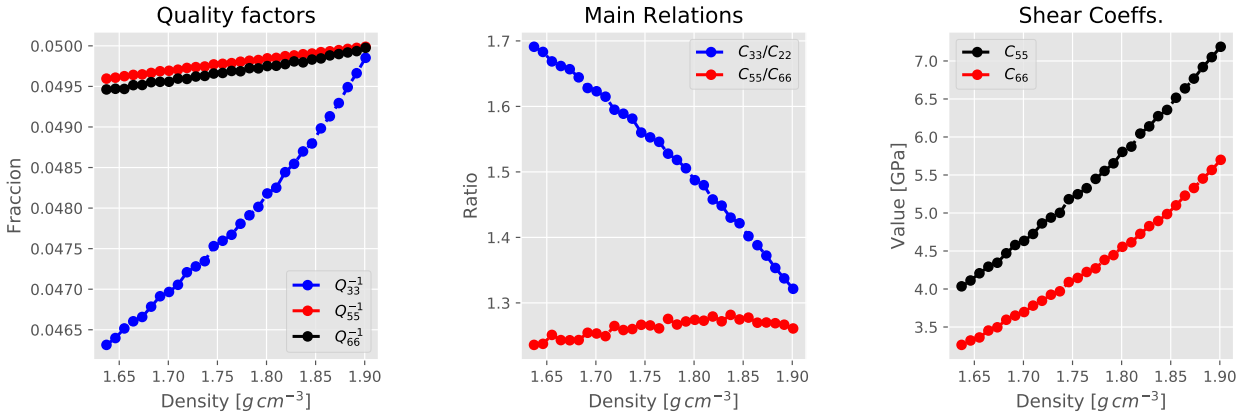

Figure 5.1: Predicted behavior for the viscoelastic model. It is shown on the left figure the predicted quality factors for a *Kelvin-Voigt* model; the center figure a prediction of homogenized coefficient ratios, and on the right figure some homogenized shear ratios with behavior as in [6].

Nevertheless, figure (5.1) cannot be used to account for the nonlinearity effects which might not be preponderant on the definition of the quality factors. In this setting, the decomposition (5.3) can be used to describe characteristic behavior regarding the linear and nonlinear contribution and therefore, answering the question of dependency on preponderant linear behavior. In this sense, figure (5.2) shows a clear direction-dependent strong nonlinear preponderance on the overall behavior for the three cases, implying full cell-problem interactions to describe each factors. In particular, becoming the cell-problems the most relevant effect that describes the mechanical behavior.

Finally, a relevant dependency that must be taken into account from the Q-factors definition (5.2) is related to the frequency dependency. From the experimental setting proposed by [6], such dependency is not taken into account on the viscoelastic operator nor in the quality-factor. In this direction, figure (5.3) describes the obtained factors for different frequency values. It shows a clear independent behavior at each frequency being used, therefore expressing the assumption proposed by *Bernard et. al. (2015)* [6] in which given the frequency range under consideration, the overall behavior of the Q-factors remains the same, i.e., equal ratio of elastic and viscous part at each frequency .

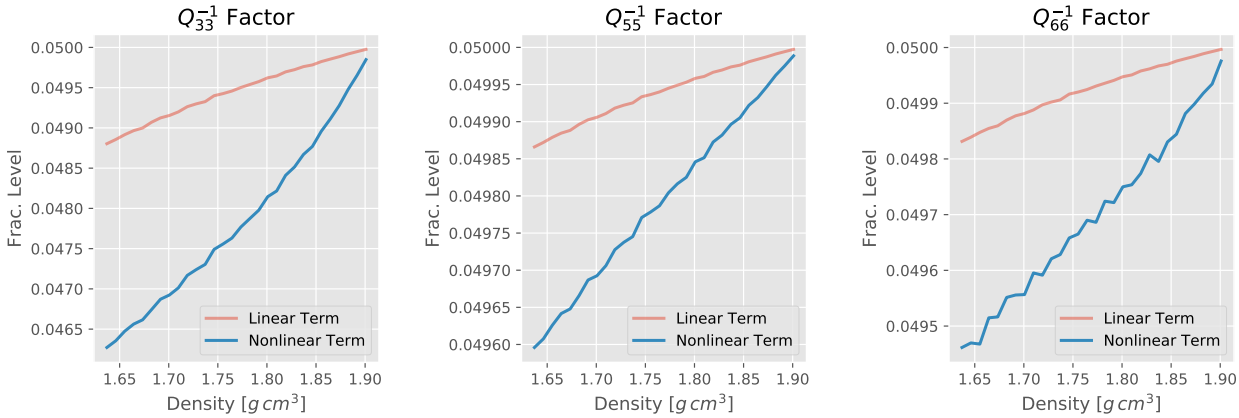

Figure 5.2: The effects from cell-problem solutions is shown for some representative quality factors accounting the linear and non-linear contributions over the range of biomedical interest.

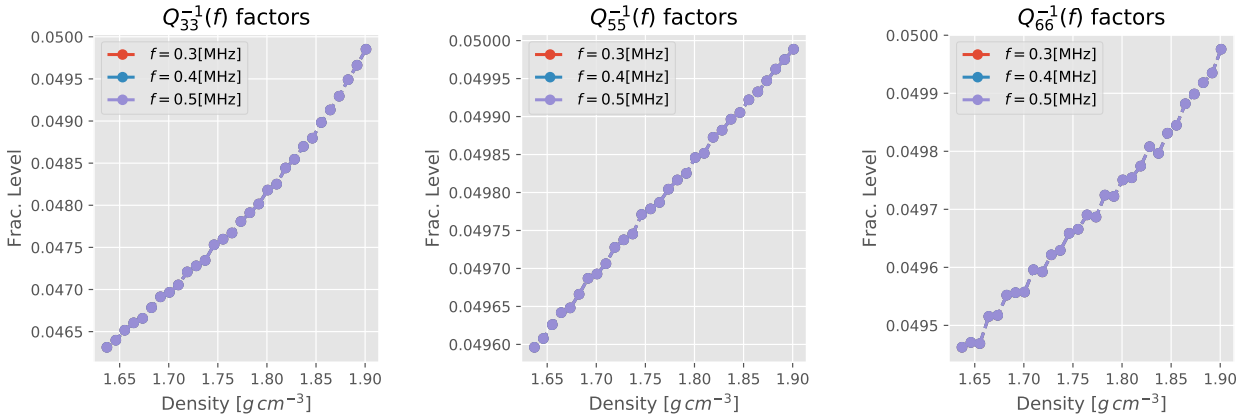

Figure 5.3: Predicted behavior for the viscoelastic model. It is shown in the left figure the predicted quality factors for a *Kelvin-Voigt* model; the center figure a prediction of homogenized coefficient ratios, and in the right figure some homogenized shear ratios behaves as in [6]

Conclusion

The current advance of QUS devices, capable to record multi-array signal opens-up the study of new techniques to recover clinical-relevant data from which various material properties can be extracted. Nonetheless, it requires the validation and case-study of possible limitations of such devices in wide variety of setting to evaluate fidelity and therefore, assure clinical usage.

This works fills that gap, recreating under simplified configurations the modelling and generation of realistic wave-front recording that reproduce *Lamb*-curves describing the material behavior. By applying two microstructure types regarding the homogenization assumptions, it is obtained by FEM homogenized tensors that resemble PG predictions with $< 1\%$ of RMSE for axial-related coefficients, while > 10 errors on fully anti-axial coefficients at high porosity values. Such error remains similar at changes from square to hexagonal and cubic type geometries, attributed then to the axial 2-dimensional assumptions of the characteristic microstructure, not adding possible anti-axial effects.

Modeling, discretization and simulations regarding the novel QUS method are done under 2-dimensional settings, both in time and frequency domains. Validation of the inverse problem predictions are done using test sets, thus ensuring correct *Lamb*-modes identification from the homogenized materials simulated under specific model cases. Similarly, the numerical procedure is generalized to 3-dimensions under regular and irregular domain characterizing cortical bone on increasing complexity and simulations are done taking into account the computational and time resources necessary to generate sample data. In this sense, the high cost of the computational simulations to retrieve irregular models with enough fidelity become a bottleneck, therefore non-physically inspired model could be taken into account such as learning methods in a cost-functional perspective. On the other hand, from a device-linked perspective, the time-domain model shows dependence from the directional measurement and therefore the sensibility and lack of robustness toward small changes in directional recordings. Such aspect must be considered in future device development and modeling, since it describes a fundamental defect that can negatively contribute towards an extensive device usage in standard clinical procedures.

The presence of viscous-like behavior on experimentally recorded signals becomes an relevant investigation factor, that could echo the processed signal. Several literature have tried to retrieve such contribution to the overall mechanical behavior, nevertheless the difficulty to separate such contribution from the other factors such as domain irregularities have become a challenge from the experimental setting as from the modelling perspective. Under such context, quality-factor are defined from a homogenized *Kelvin-Voigt* viscoelastic model. It represent a first approach, formally validated, that recreates experimentally observed values under specific parameters and moreover, recovers the elastic coefficient values. Nevertheless, the lack of experimental data lets us conclude partial prediction of quality-factors only at high density values of cortical bone.

Directions to follow the current work are many, but investigations to tackle the numerical model under efficient methods, and study closely the effects of particular mesh irregularities are relevant to assess validation of the experimental procedure in more complex domains. Similarly, studies regarding the device sensibility can be taken into account, such as variation of directional measurements and moreover effects of device noise over the general setting. In a similar fashion, more complex viscoelastic models fitting experimental data should be considered since bone-skin and bone-marrow interactions contribute as damping effects on the recorded signal.

Bibliography

[1] Bilen Abali. *Computational reality : solving nonlinear and coupled problems in continuum mechanics*. Springer, Singapore, 2016.

[2] Zouhair Abdessamad and Grigory Panasenko. Memory effect in homgenization of a viscoelastic kelvin-voigt model with time-dependent coefficients. *Mathematical Models and Methods in Applied Sciences*, 19(09):1603–1630, sep 2009.

[3] Assyr Abdulle and Andrea Di Blasio. Numerical homogenization and model order reduction for multiscale inverse problems. *publication*, 2016.

[4] Holm Altenbach. *Generalized models and non-classical approaches in complex materials*. Springer, Cham, Switzerland, 2018.

[5] N Bakhvalov. *Homogenisation: Averaging Processes in Periodic Media : Mathematical Problems in the Mechanics of Composite Materials*. Springer Netherlands, Dordrecht, 1989.

[6] Simon Bernard, Joannes Schneider, Peter Varga, Pascal Laugier, Kay Raum, and Quentin Grimal. Elasticity–density and viscoelasticity–density relationships at the tibia mid-diaphysis assessed from resonant ultrasound spectroscopy measurements. *Biomechanics and Modeling in Mechanobiology*, 15(1):97–109, jun 2015.

[7] Ahmed Boughammoura. Homogenization of a highly heterogeneous elastic-viscoelastic composite materials. *Mediterranean Journal of Mathematics*, 10(4):1793–1812, feb 2013.

[8] Xiran Cai, Renald Brenner, Laura Peralta, Cécile Olivier, Pierre-Jean Gouttenoire, Christine Chappard, Françoise Peyrin, Didier Cassereau, Pascal Laugier, and Quentin Grimal. Homogenization of cortical bone reveals that the organization and shape of pores marginally affect elasticity. *Journal of The Royal Society Interface*, 16(151):20180911, feb 2019.

[9] R. M. Christensen. *Theory of viscoelasticity : an introduction*. Academic Press, New York, 1982.

[10] Alexandre Ern. *Theory and practice of finite elements*. Springer, New York, 2004.

[11] Lawrence Evans. *Partial differential equations*. American Mathematical Society, Providence, R.I, 2010.

[12] Josquin Foiret, Jean-Gabriel Minonzio, Christine Chappard, Maryline Talmant, and Pascal Laugier. Combined estimation of thickness and velocities using ultrasound guided waves: a pioneering study on in vitro cortical bone samples. *IEEE Transactions on Ultrasonics, Ferroelectrics, and Frequency Control*, 61(9):1478–1488, sep 2014.

[13] Anders Logg. *Automated solution of differential equations by the finite element method : the FEniCS book*. Springer, Berlin New York, 2012.

[14] Anders Logg and Garth N. Wells. Dolfin: Automated finite element computing. *ACM Transactions on Mathematical Software*, 37(2), 2010.

[15] J.-G. Minonzio, N. Bochud, Q. Vallet, Y. Bala, D. Ramiandrisoa, H. Follet, D. Mitton, and P. Laugier. Bone cortical thickness and porosity assessment using ultrasound guided waves: An ex vivo validation study. *Bone*, 116:111–119, nov 2018.

[16] O. A. Oleinik. *Mathematical problems in elasticity and homogenization*. North-Holland, Amsterdam New York, 1992.

[17] G. P. Panasenko. *Multi-scale modelling for structures and composites*. Springer Sold and distributed in North, Central, and South America by Springer, Dordrecht, Netherlands Norwell, MA, 2005.

[18] W.J. Parnell and I.D. Abrahams. Homogenization for wave propagation in periodic fibre-reinforced media with complex microstructure. i—theory. *Journal of the Mechanics and Physics of Solids*, 56(7):2521–2540, jul 2008.

[19] Pierre Raviart. *Introduction à l'analyse numérique des équations aux dérivées partielles*. Masson, Paris New York Barcelone, 1983.

[20] Sang-Ho Rhee, Jeong-Ki Lee, and Jung-Ju Lee. The group velocity variation of lamb wave in fiber reinforced composite plate. *Ultrasonics*, 47(1-4):55–63, dec 2007.